High Precision and Safe Hybrid Pneumatic-Electric Actuated Manipulators

High Precision and Safe Hybrid Pneumatic-Electric Actuated Manipulators

By

Behrad Rouzbeh

B.Sc., M.Sc.

A Thesis Submitted to the School of Graduate
Studies in Partial Fulfilment of the Requirements for
the Degree

Doctor of Philosophy

McMaster University
Hamilton, Ontario, Canada

December 2020

© Copyright by Behrad Rouzbeh, 2020

Doctor of Philosophy (2020) (Mechanical Engineering)

McMaster University Hamilton, Ontario

TITLE:	**High Precision and Safe Hybrid Pneumatic-Electric Actuated Manipulators**
AUTHOR:	**Behrad Rouzbeh, B.Sc., M.Sc.**
SUPERVISOR:	**Dr. Gary M. Bone, Ph.D., P.Eng.**
NUMBER OF PAGES:	**xviii, 147**

This thesis is dedicated to my wife for her love, endless support and sacrifices. My heart pounds for you every second!

Lay Abstract

Robots that work with, or near, humans require greater safety considerations than other robots. A significant concern is collisions between the robot and humans that may happen when sensors or software fails. An actuator for robots that combines the inherent safety of pneumatic actuators with the accuracy of electric actuators, termed a “hybrid pneumatic electric actuator” (HPEA), is investigated. The design, instrumentation, modelling, and control of HPEAs are studied theoretically and experimentally. The proposed actuator could achieve high position control accuracy in a variety of experiments, with steady state error of less than 0.0045 degrees. Simulated impacts with a human head also showed that a HPEA-driven robot arm can achieve a 52% lower impact force, compared to an arm driven by conventional electric actuators. The HPEA design and control experiments are performed on a single HPEA-driven joint and extended to an arm consisting of two HPEA-driven revolute joints.

Abstract

Robot arms require actuators that are powerful, precise and safe. The safety concern is amplified when these robots work closely with people in collaborative applications. This thesis investigates the design and implementation of hybrid pneumatic-electric actuators (HPEA) for use in robot arms, particularly those intended for collaborative applications. The initial focus was on improving the control of an existing single HPEA-driven rotary joint. The torque is produced by four pneumatic cylinders connected in parallel with a small DC motor. The DC motor is directly connected to the output shaft. A cascaded control system is designed that consists of an outer position control loop and an inner pressure control loop. The pressure controller is based on a novel inverse valve model. High precision position tracking control is achieved due to the combination of the model-based pressure controller, model-based position controller, adaptive friction compensator and offline payload estimator. Experiments are performed with the actuator prototype rotating a link and payload with a rotational inertia equivalent to a linear actuator moving a 573 kg mass. Averaged over five tests, a root-mean-square error of 0.024° and a steady-state error (SSE) of 0.0045° are achieved for a fast multi-cycloidal trajectory. This SSE is almost ten times smaller than the best value reported for previous HPEAs. An offline payload estimation algorithm is used to improve the control system's robustness. The superior safety of the HPEA is shown by modeling and simulating a constrained robot-head impact, and comparing the result with equivalent electric and pneumatic actuators. This research produced two journal papers.

Since HPEAs are redundant actuators that combine the large force, low bandwidth characteristics of pneumatic actuators with the large bandwidth, small force characteristics of electric actuators, the effect of using optimization-based input allocation for HPEAs was studied. The goal was to improve the HPEA's performance by distributing the required input (force or torque) between the redundant actuators in accordance with each actuator's advantages and limitations. Three novel model-predictive control (MPC) approaches are designed to solve the position tracking and input allocation problems using convex optimization. The approaches are simulated on a HPEA-driven system and compared to a

conventional linear controller without active input allocation. The first MPC approach uses a model that includes the dynamics of the payload and pneumatics; and performs the motion control using a single loop. The latter methods simplify the MPC law by separating the position and pressure controllers. Although the linear controller is the most computationally efficient, it is inferior to the MPC-based controllers in position tracking and force allocation performance. The third MPC-based controller design demonstrated the best position tracking with root mean square errors of 46%, 20%, and 55% smaller than the other three approaches. It also demonstrated sufficient speed for real-time operation. This research produced one journal paper.

The research continued with the design and implementation of a two degree-of-freedom HPEA-driven arm. A HPEA-driven “elbow” joint is designed and added to the existing “shoulder” joint. The force from a single pneumatic cylinder is converted into torque using a 4-bar linkage. To eliminate backlash and keep the weight of the arm low, a 2nd smaller DC motor is directly connected to the joint. The kinematic and kinetic models of the new arm, as well as the geometry of the new elbow joint are studied. The resulting joint design is implemented, tested and controlled. This joint could achieve a SSE of 0.0045° in spite of its nonlinear joint geometry. The arm is experimentally tested for simultaneous tracking control of the two joints, and for end-effector position tracking in Cartesian space. The end-effector is able to follow a circular trajectory in pneumatic mode with position errors below 0.005 m.

Acknowledgements

My sincere gratitude goes to my supervisor Dr. Gary M. Bone for his continuous support, his patience, encouragement, and guidance throughout the course of my PhD. Dr. Bone selflessly and patiently helped me in many different ways.

Special thanks are due to my supervisory committee members, Dr. Saeid Habibi and Dr. Shahin Sirouspour, for their valuable comments and suggestions. I would like to thank Dr. Brian W. Surgenor for reviewing my work and providing insightful comments as the external examiner.

I am thankful for the help and support provided by the wonderful technical staff in the Mechanical Engineering Machine Shop, specifically Michael Lee and Mark Mackenzie.

My gratitude extends to all my friends and colleagues whom I met during my journey at McMaster University for their moral supports and helpful discussions. Many thanks to Dr. Mohammad Taghi Ahmadian at Sharif University who helped me to become a research scientist and a free thinker I am today; and to my former Master's supervisor at Amirkabir University, Dr. Firooz Bakhtiarinejad who taught me a lot about the realm of Controls Engineering and Mechatronics.

I would also like to appreciate the National Sciences and Engineering Research Council (NSERC) for the financial support throughout this research.

At last, but by no means the least, I want to give a big thank you from the bottom of my heart to my parents, my wife, and my sister and my brother, and my lovely son for their love, spiritual support, and prayers as I completed this research.

Co-Authorship

This thesis has been prepared in accordance with the regulations for a 'Sandwich' thesis format or as a compilation of papers stipulated by the Faculty of Graduate Studies at McMaster University. Chapters 2 through 4 have been published in peer-reviewed journals. The author of this thesis confirm that he is the primary performer of all research and primary author of all the proceeding chapters. Chapters 2 and 3 use a test setup for which the design and implementation of the mechanical part had been carried out by Graham Ashby (listed among the authors). Graham Ashby also developed some of the control system equations and software used in chapters 2, 3 and 5. The work was all completed under the supervision, guidance, and review of Dr. Gary Bone.

Chapter 2: High Accuracy Position Control of a Rotary Pneumatic Actuator.
Authors: Behrad Rouzbeh, Gary M. Bone, and Graham Ashby
Published in *IEEE/ASME Transactions on Mechatronics*, 23 (2018), 2774-2780.

Chapter 3: Design, Implementation and Control of an Improved Hybrid Pneumatic-Electric Actuator for Robot Arms

Authors: Behrad Rouzbeh, Gary M. Bone, Graham Ashby, and Eugene Li
Published in *IEEE Access*, 7 (2019), 14699 - 14713.

Chapter 4: Optimal Force Allocation and Position Control of Hybrid Pneumatic–Electric Linear Actuators.

Authors: Behrad Rouzbeh and Gary M. Bone
Published in *Actuators*, 9 (2020), 86 - 100.

Contents

List of Tables

List of Figures

Chapter 1. Introduction

1.1 Introduction

Robots that work directly with, or in close proximity to, humans are considered within a category defined as “collaborative robotics” [1]. Collaborative robots have numerous applications and are a very active research area. There are some technical and safety concerns that are more critical in this field compared to general robotics. Related standards are still under development such as the recently introduced ISO/TS 15066 that proposes strict safety requirements for collaborative robots [2]. A significant concern is collision between human and collaborative robots when active precautions fail, or an unpredicted software error happens. Developing compliant manipulators with low mechanical impedance is an answer to this concern. This can be achieved by including innovative actuation methods benefiting from some of the positive characteristics of pneumatic actuators.

Driving the joints of robot arms requires actuators that provide both high torque and precise motion. Conventional pneumatic actuators are known to have high torque-to-mass ratio, low mechanical impedance, low cost, low friction, rare overheating concerns, and effectiveness for force-control and impedance-control applications. On the other hand, their accuracy, bandwidth, and robustness are known to be insufficient for some applications. Their performance can be considerably undermined when subjected to common situations such as: unknown payloads, external disturbances, and unknown friction in the system.

Electric motors are easier to model and control, and benefit from higher bandwidth and accuracy. They are the most commonly used actuator since they are also easy to control precisely and easy to interface. However, they are prone to overheating when they must provide a large continuous torque. When electric motors are used as robotic actuators, because the torque produced by a reasonably sized motor is insufficient, high ratio gearboxes are usually inevitable (typically with a ratio of 100:1 or more). This high ratio

gearbox makes the mechanical impedance of the actuator high. The high impedance has two main causes. First, the moment of inertia at the output of the gearbox is equal to the motor's inertia times the transmission ratio squared. Second, the actuator's friction torque equals the motor's friction torque amplified by the transmission ratio, plus the friction torque introduced by the transmission. Such high impedance can produce unsafe collision forces during collaborative function. Backlash is another disadvantage of adding a gearbox.

A hybrid pneumatic-electric actuator (HPEA) is an innovative device that can benefit from the advantages of both actuators if properly designed and controlled. Thus design, instrumentation, modelling, and control of hybrid actuators that can function in realistic conditions will be an important contribution to collaborative robotics.

1.2 Motivation and Goals

As robotics technology is spreading to new applications in everyday life, collaborative robots play a key role in this field. With the latest advances in artificial intelligence and mechatronic systems, robots are continuously gaining abilities to perform new tasks. Reliability and safety are the main concerns about recruiting robots to new tasks that used to be done by humans. Safety issues are the most important with collaborative robots as they share their workspace with humans. With state-of-the-art sensors and elaborate algorithms, active safety precautions have been developed such as: collision avoidance techniques, impedance control methods, force control of end-effectors, and active collision reaction.

Although active solutions are beneficial, they may fail due to hardware/software failures or when encountering unexpected conditions. Therefore, it is necessary to improve the inherent safety of mechanical systems in parallel with the active solutions. Some solutions to increase inherent safety of collaborative robots include: use of soft-bodied robots, use of compliant surfaces, and employing actuators with higher inherent safety. HPEAs can serve toward the latter. Progress on the design and control of this type of actuator has been made since it was introduced in 1980s [3]. However, in robotics, and specifically collaborative manipulators, electric actuators still play the main role due to their reliability, accuracy,

and bandwidth. A HPEA-driven manipulator that can inherit the advantages of electric motors and add the high power-to-weight-ratio, compliance, and inherent safety of pneumatic actuators (due to low mechanical impedance, low inertia, and low friction, etc.) can change the actuation trend in this field, if it remains feasible and cost-efficient.

Given these motivations, the intent of this research is to design and develop a prototype of HPEA-driven robotic manipulator with the following goals:

- **Actuator with high inherent safety, high accuracy, and fast response time:** The main design goal is to benefit from the compliance, low friction, and low inertia of pneumatic actuator in the whole HPEA design. With help of the pneumatic part, the need for high ratio gearbox for the electric actuator will be eliminated. This will contribute to lowering the overall actuator inertia and mechanical impedance. This actuator should be easily back-drivable, which is favorable for teaching the robot by manually dragging its end-effector to the desired trajectory points. Simulations should be done to investigate the collision safety. The electric actuator used within the HPEA should compensate for the weaknesses of the pneumatic actuator and lead to a positioning accuracy comparable to the electric actuators used with robots. In addition to better hardware, developing the high performance HPEA will require the development of an advanced control system. The main challenge is the controller must manage the coupled dynamics of the pneumatic and electric actuators. This controller must calculate the required torque and provide it as accurately and fast as possible by appropriately defining the contribution from each actuator (also known as the torque distribution, torque allocation or input allocation problem). If the new HPEA is able to provide sufficient accuracy and speed of response, then its inherent safety will make it a desirable choice for collaborative robots.

- **Design and implementation of multiple degree-of-freedom HPEA-driven manipulator:** Although there is some literature on rotary single degree-of-freedom (DOF) arms powered by an HPEA, their application to more complicated manipulators has not been explored. This research will start by studying modeling and control improvements on a 1-DOF HPEA-driven arm. To further advance the field this should be developed into a

more realistic and novel multi-DOF HPEA-driven manipulator. The goal is to modify the existing 1-DOF system into 2-DOF manipulator by designing and fabricating a new hybrid actuator for the 2nd joint. The goal is to achieve a completely HPEA-driven two-DOF manipulator that can provide effective position control of the joints and end-effector.

- **Experimental evaluation:** A test setup for HPEA-driven manipulator needs to be prepared to implement the actuator and controller design ideas. The advantages of HPEA design should be experimentally tested and evaluated.

- **Cost efficiency of the whole design:** The goal of this research is to present a solution that can be used by industry in future as a better alternative to current actuation methods. There are many examples of successful research that used the highest technologies and most elaborate equipment to produce favourable results; but never made their way into people's lives because of expensive and complex equipment that made them too impractical. The cost efficiency and availability issues are important factors in this research. Achieving the expected results with cost-efficient equipment is one of the challenges.

1.3 Literature Review

The most relevant and advanced papers are reviewed in this section. They are organized into the following five subsections.

1.3.1 Modelling and Position Control of Pneumatic Actuators

Pneumatic actuators are known to have highly nonlinear and compliant characteristics which makes controlling them a challenge. This challenging control problem has attracted extensive research interest both in past decades (e.g., [1][2][3][4][5][6][7]) and in recent years ([8][9][10][11][12][13][14]). The majority of the previous research has been on the position control of actuators providing linear motion. We will use the term "rotary actuator" to refer to any actuator that rotates an output shaft or arm, including those employing cylinders and linear-to-rotary mechanisms; and vane-type actuators that rotate

directly. Even though they are much more commonly used with robotic arms, relatively few researchers have investigated the position control of rotary pneumatic actuators.

For decades, pneumatic actuators were conventionally considered for limited set-point positioning applications. They were known to provide relatively lower bandwidth due to the compliance of the air, and the delays in air flow which increase with the length of the connecting tubes. The air flow through the pneumatic actuators is highly nonlinear and difficult to model. Shearer [15] developed detailed mathematical equations for the thermodynamics and the air flow of the charging-discharging process in pneumatic circuits. These equations paved the way to develop efficient models for the pneumatic actuators and use them with various modern position controllers. In [16], Richer and Hurmuzlu extended this research to develop a detailed mathematical model for double-acting pneumatic cylinders controlled by proportional spool valves. Leakage, delay, and attenuation in pneumatic lines were included in their model.

The majority of the papers on position control of pneumatic actuators have used proportional or servo valves [3][7][9][13][14][16][17][18]. These valves allow the air flow to be continuously varied making the position problem easier. However, they are much more expensive than on/off solenoid valves (e.g., U.S.$800 vs. U.S.$40). Since one of the benefits of pneumatic actuators is their low cost we are more interested in using on/off solenoid valves like those used in [1][2][5][10][11][12] even though they make precise position control more challenging.

Bobrow and McDonell [3] developed nonlinear model-based hierarchical control laws for the position control of a robotic arm with three rotary joints. For modeling, they used a nonlinear dynamic model of valves and the thermodynamic properties of compressed air. Each joint was actuated by a pneumatic cylinder connected by cables to a pulley. A 5/3 servo valve was connected to each cylinder. Tracking errors as large as 4° were observed for 100° moves in their experiments. No considerations for model uncertainties were reported.

Pandian et al. [7] controlled a vane-type rotary actuator using two proportional valves and a model-based adaptive control law. Unfortunately, they did plot or not report any numerical values for the tracking errors.

Much later, Bone and Chen [10] proposed a discrete-valued model-predictive control algorithm for pneumatic actuators driven by on/off solenoid valves. The hardware included two 3/2 solenoid valves, a pneumatic cylinder and a rack and pinion mechanism to produce the rotary motion. They also connected an electric motor in parallel with the pneumatic actuator to form a HPEA that will be discussed in the next subsection. A maximum tracking error of 2.9° was achieved for a 115° vertical cycloidal trajectory experimentally using the pneumatic actuator alone. It is important to note that the robot arm was much smaller in [10] than in [3].

Rahman, He and Sepehri [9] controlled a rotary joint consisting of pneumatic cylinder connected to a link using pin joints. They utilized a 5/3 proportional valve and proposed an adaptive backstepping–sliding mode control law to control the position of the cylinder and a Lugre-based friction observer. Unfortunately, they only reported linear position control results. For a 0.1 Hz, 100 mm amplitude, sinusoidal reference trajectory the maximum tracking error was 5 mm. For a multiple-step polynomial trajectory the maximum tracking error was similar, and the average steady-state error (SSE) was 0.52 mm.

Tuvayanond and Parnichkun proposed an H∞ loop shaping controller based on particle swarm optimization for a pneumatic robot arm with three joints [13]. The first joint used a rotary actuator consisting of two pistons driving rack gears meshed with a common pinion gear. The air flow was controlled by a 5/3 proportional valve. For a 60° reference trajectory the maximum error was 0.96° and the SSE was 0.3° or less.

A much more powerful rotary actuator (with maximum pneumatic torque of 36.6 Nm) employing four pneumatic cylinders to drive a rack and pinion mechanism was presented by Ashby and Bone in [12]. As in [10] and [11], they used an HPEA consisting of an electric motor in parallel with the pneumatic actuator for some of their experiments. The

pneumatic actuator was controlled using two 3/2 on/off solenoid valves, an outer position control loop and two inner pressure control loops. The controller for the pneumatic actuator consisted of a model-based outer-loop position control law, an inner-loop linear feedforward plus feedback pressure control law (not model-based) and an adaptive friction compensator. When the pneumatic actuator was used alone, the arm followed a 90° vertical cycloidal trajectory with a root mean square error (RMSE) of 0.096° and a SSE of 0.0045°.

Chen et al. proposed a novel actuator combining a plastic vane-type pneumatic motor with a 100:1 gearbox for use in surgical robots [14]. The actuator was controlled using conventional proportional plus integral plus derivative feedback and a 5/3 proportional valve. For a 120° step reference inputs the RMSE was 0.9° and the SSE was 0.7°.

Rao and Bone [4] modelled proportional 2-way valves as part of their model-based controller development. Experimental data was first collected for each of the individual valves used. Steps throughout the control signal range were input and system pressure was measured, and mass flow rate was estimated. A second order bi-polynomial surface was fit to the data such that mass flow rate was a function of chamber pressure and control signal. The quality of fit was evaluated by comparing the result to the proportional valve model of Bobrow and McDonell [3]. Evaluated across four individual valves, the bi-polynomial had 43% less RMSE between the model and experimental data than that of Bobrow and McDonell. Rao and Bone also found the filling portion of the valve flow was more difficult to accurately model than the discharging. A nonlinear multiple- input single-output control law was developed. The state variables were position, velocity, chamber *A* pressure, chamber *B* pressure, mass flow rate through valve *A*, and mass flow rate through valve *B*. The controller was proven to be BIBO stable. Experimental tests were performed in the horizontal plane with a 1.5 kg payload. An S-curve trajectory was followed for a 20 mm move over 1 second, with an MAE of ~0.3 mm and an RMSE of 0.074 mm, for the example shown. Sine testing was also performed with a 35 mm PTP amplitude at 1 Hz, where a 0.5 mm MAE and a 0.136 mm RMSE were observed.

Hodgson *et al.* [8] presented a nonlinear discontinuous averaging model for use with a PWM based sliding mode controller. A double acting, double rod pneumatic cylinder was controlled with four 3-way solenoid valves. With the increased number of valves nine useful operating modes existed in the system. Only seven modes were retained for consideration, as two produce a similar effect, although less effectively than the other modes. The output over a period was the sum of the effects of each mode multiplied by their portion of the PWM period. By selecting the most effective modes, three mode, five mode, and seven-mode models were also developed and compared. The three mode and seven mode controllers were experimentally evaluated. A 0.9 kg payload was controlled in the horizontal plane for step tests of 40 mm. Three mode and seven mode switching controllers were also compared to a model-based sliding-mode controller. The position error values are quite similar for their experiments, but the model-based seven mode controller significantly reduces the number of required switches, which should extend valve life.

Carneiro and de Almeida [6] used an artificial neural network (ANN) approach to model the nonlinear nature of the pneumatic components. A double acting pneumatic cylinder with two proportional valves was studied. Three separate ANNs were developed and used. The first, an inverse ANN model, was used for the valves, which given mass flow rate desired and pressure differential between chambers returned an appropriate PWM frequency input for the valves. The second, a direct ANN model, returned a mass flow rate given the valve PWM frequencies, and instantaneous chamber pressure differential. The third, another direct ANN model, estimated the friction force given the current velocity and acceleration estimates of the system. The ANNs were black box models trained using experimental data to approximate a relationship (three dimensional surfaces in these cases) between the input/output variables. The difficulty in using ANNs lies in gathering appropriate data, selecting proper network configuration, and solving the optimization problem required to tune the network. The friction model developed had a fitting error of 1.9% of the maximum range of friction values. The direct model had a maximum error in

fit of 1.25% when compared to the mass flow rate used for training. When the inverse model was used to control the valve, a maximum 1.3% mass flow rate error was achieved.

1.3.2 Design, Modelling and Control of HPEAs

A design concept for a rotary HPEA consisting of an electric motor connected in parallel to pneumatic rotary actuator was proposed in a 1987 patent [19]. It was intended to solve the problems of electric motor overheating and low power to weight ratio for high payload applications, but was never produced. In contrast to pneumatic actuators, limited research has been performed on HPEAs.

In [20] they connected a DC motor in parallel with a rotary pneumatic motor using a pair of gears. The output shaft drove a single-link robot arm via a second pair of gears. The effective gear ratios of the pneumatic motor and DC motor to the output shaft were 30:1 and 15:1, respectively. The hardware included two servo valves, an optical encoder on the output shaft, and two pressure sensors. A 1.5 kg payload was position controlled in the horizontal plane. They presented two control algorithms. For tracking a sinusoidal position trajectory, they designed a SMC strategy based on a linearized model of the hybrid actuator. For point-to-point motion control they proposed a mixture of SMC and PD control. They included experimental results for horizontal motions including step inputs and a 200° peak-to-peak, 0.5 Hz, sinusoidal trajectory. Compared with the pneumatic motor operating alone (under SMC), the hybrid actuator reduced the settling time from 1.2 s to 0.5 s for the step input, and the maximum tracking error from 20° (10%) to less than 10° (5%) for the sinusoidal input.

In [21] the HPEA prototype included antagonistic PAM approach pneumatic muscle actuators (PMAs) connected by cables to an output pulley with a 0.0305 m radius. A DC motor was connected to the output pulley by a 28:1 gearbox. The force output of each PMA was controlled using a PID control loop with the gains experimentally tuned, and a proportional valve. The angular position of the joint was controlled using acceleration feedforward plus PD control. Their controller divided the torque between the pneumatic and electric actuators by first requesting the full torque from the pneumatic and assigning

the torque error between the pneumatic and desired to the electric. They included experimental results for 12° peak-to-peak, 1 Hz and 3 Hz sinusoidal position trajectories with no payload mass. Based on their plots, the hybrid actuator reduced the maximum tracking error from about 50% to about 10%, compared with the PMAs operating alone.

A unique design for a linear HPEA was presented in [22]. Their design integrates a pneumatic cylinder and a linear electric motor into a very compact device. They control the forces produced by the cylinder and motor using separate PI controllers. They reported force control RMSE values. The HPEA reduced the RMSE to 1.77 N compared to the 6.26 N obtained using only the pneumatic cylinder. They did not control the HPEA's position or use it to drive a rotary joint.

The HPEA design in [10][11] generated the majority of its torque using a single pneumatic cylinder to push/pull the rack of a rack and pinion mechanism. The pinion was directly connected to the output shaft. A DC motor also drove the pinion via a smaller gear resulting in a 5:1 transmission ratio. Rather than using pulse-width modulation (PWM) with the on/off solenoid valves, they were directly switched using a discrete-valued model predictive control algorithm. The motor was controlled using a variant of inverse dynamics control.

Bone and Chen [10] described the "GEN1" HPEA. It used two 3-way solenoid on/off valves, one per chamber. The charging and discharging mass flow rates were modelled by piecewise equations. The relationship was empirically developed to fit to observed mass flow data. The cylinder pressure model for the cylinders was based upon those presented by Shearer [15]. The model of friction incorporated either a sum of Coulomb and viscous friction, or simply static friction. The values were experimentally determined for the particular cylinder used. They did not provide any information about the accuracy of their models.

In [11], Bone, Xue and Flett used discrete-valued model predictive control and a payload estimator. In vertical motion experiments with a zero to 90° cycloidal trajectory (where 90° produced the max. gravity load), the RMSE and SSE were 0.64° and 0.23°, respectively,

when only the pneumatic actuator was used. When the DC motor was activated the RMSE and SSE were reduced to 0.11° and 0.04°, respectively.

1.3.3 Manipulator Impact Safety

Researchers have proposed a wide variety of approaches for reducing the human-robot impact force. In [23] the impact force is reduced by applying a time-varying limit to the actuator torques based on a dynamic model of the robot. While this can work in certain situations, an undesirable reduction in the precision of the robot's trajectory tracking may also occur when the actuator torques are limited.

Reducing the inertia of the robot can be very effective at reducing the impact force. The robot developed by DLR [24] is a prime example of this approach whose special design and use of lightweight materials, such as carbon fiber, produced a very low inertia arm. However, this is a costly solution and obviously cannot be used to improve the safety of conventional robots.

Reducing the stiffness of the transmission between the actuators and links is another approach for improving the collision safety, e.g. [25][26]. With conventional robots the transmission between each actuator and link is very stiff so both of their inertias contribute to the severity of the collision. The objective of variable-stiffness actuation (VSA) is to dynamically decouple the actuator's rotor inertia from the link's inertia. Since the contact occurs between the human and the link, and the link's inertia is lower than the combined inertia, the impact force will be reduced by the VSA's decoupling effect. The lower the stiffness the lower the force, however low transmission stiffness also tends to lower the precision of the robot's position control. Similarly, a lower arm velocity also reduces the impact force, but clearly sacrifices the robot's performance. The VSA mitigates these two problems by lowering the stiffness when the velocity is high and increasing the stiffness when the velocity is low. This addresses the safety aspect but will also cause the tracking precision to deteriorate during the higher velocity sections of its motion trajectories. Furthermore, using VSAs for the robot's six joints will increase the complexity, cost, and inertia of the arm.

Adding an electromechanical clutch between the link and actuator is an alternate approach to decouple the actuator's and link's inertias [27][28]. This behaves like a VSA with two stiffnesses and is termed a "series clutch actuator" (SCA). When clutch is engaged the transmission's stiffness is very high, and when it is disengaged the stiffness drops to zero. Unlike a VSA, the SCA should not affect the robot's performance during normal conditions since the clutch should only disengage when a collision happens. The clutch's torque threshold can also be varied to satisfy both the safety and performance requirements [27]. Unfortunately, using SCAs will increase the complexity, cost, and inertia of the robot arm.

Another approach is to add an active collision detection and reaction strategy to the robot's control software, e.g. [29][30][31]. The detection can use either the robot's existing sensors [29][30] or externally mounted sensors [31]. The former approach requires a dynamic model of the robot while the latter does not. Using either approach detection times of a few ms can be achieved [29][30][31]. Various reaction strategies may be executed after contact detection to reduce the impact force, such as: braking to a stop [29][31], switching the actuator off [30], or having the arm reflexively withdrawn from the location of the impact [29]. These methods do not add to inherent safety of the robot arms. Like all active methods, these approaches are prone to failure due software bugs, hardware failures, and unexpected operating situations.

One fail-safe method for increasing the inherent safety of robot arms is to add a compliant cover over its surface, e.g. [29][32][33]. The cover's stiffness can be chosen to satisfy a safety constraint without being excessively thick [33]. The compliant cover cannot be used with the end-effector if it interferes with its function. If this is the case, quick release mechanisms, such as the QuickSTOP collision device (Applied Robotics Inc.), can be used to increase the safety of collisions with the end-effector.

When studying the impact between a robotic arm and a human, an impact with the head is known to be one of the most critical cases with the potential to cause the most serious damage. The "head injury criterion" developed for the automotive industry has been proposed and used to assess the injury risk of an impact between a robotic arm and human

head (e.g. [1] and [34]). This criterion is based on the magnitude of head acceleration after the impact.

1.3.4 Input Allocation for Redundant Actuators

With a hybrid actuator, like a HPEA, two actuators with different characteristics are performing the same task, which results in actuator redundancy. Since each of these actuators has completely distinct capabilities, the HPEA's best performance can be obtained by systematically allocating the forces/torques between them according to their characteristics.

The motion controller structure for HPEAs and other redundant actuators incorporates three levels [35]: (1) The high-level motion controller that uses a control method to determine the virtual high-level inputs (force or torque), (2) The input allocation level that distributes the virtual inputs between the actuators using predefined algorithms, and (3) The internal controller within each actuator that defines the low level inputs (like command signals to the valves) that can provide the virtual input with enough accuracy. With optimization-based motion controllers, it is possible to merge the motion control and input allocation problems and address them in a single control law.

Input allocation for redundant actuators has been a topic of interest mainly to control aircraft and autonomous vehicles. Several studies have been devoted to providing mathematical frameworks for the input allocation of dynamic systems. In [36], a modified quadratic programming method has been proposed to include the actuator rates and their bandwidth limitations within the standard quadratic programming problem for input allocation purposes. Optimization-based methods have been the most common allocation approaches in the literature.

In [37], an optimal control approach is used with a generic linear plant model that can handle a redundant actuator tracking multi-sinusoidal reference. In [35], several optimization-based techniques have been presented to solve unconstrained and constrained input allocation problems for generic linear and nonlinear plant models. Since optimization-based approaches mostly require high computational load and

implementation complexity, researchers have developed tools to help with implementing the optimization techniques with high computational efficiency (see [38][39][40]).

Although there have been some papers focused on position controller design for HPEAs (e.g.[11],[41]), very few have used a controller that incorporates each actuator's characteristics and studied the allocation problem alongside the position control problem.

In [42], an optimization method is proposed for the torque allocation of a HPEA consisting of a PMA and an electric motor. They proposed a two-stage optimization approach that can be used for redundant actuators that consist of a higher bandwidth actuator and a lower bandwidth one. Their approach approximates the nonlinear open-loop pressure dynamics using a first-order linear model.

1.4 Thesis Organization

This thesis was prepared in accordance with the regulations of a "sandwich" thesis format containing previously published material. Since chapters 2 to 4 were published as stand-alone journal papers ([43], [44] and [45]), each chapter has its own introduction, conclusion, and bibliography. Some overlap might exist between chapters, mainly in the introduction part of each.

The remainder of this thesis comprises the following five chapters:

- Chapter 2 studies the position control of a rotary pneumatic actuator. The pneumatic subsystem is the highly nonlinear component of a HPEA; hence significantly challenging to be effectively modeled and accurately controlled. This chapter studies only the pneumatic subsystem of a HPEA that actuates a 1-DOF arm. The modelling, controller design and experimental verification of a high accuracy position controlled rotary pneumatic actuator is presented. A novel model-based pressure controller is designed as an inner-loop controller within a

cascade control architecture. Experimental results are included for a 1-DOF arm moving in the vertical plane. The hardware features low-cost on/off solenoid valves and low-cost pressure sensors.

- Chapter 3 studies the implementation and position control of a novel rotary pneumatic HPEA that benefits from the high accuracy pneumatic actuator introduced in chapter 2. It presents the design of a hybrid actuator with low mechanical impedance, high impact safety and higher torque output than previous designs. This actuator is compared with an equivalent electric actuator in terms of safety through head impact simulations. The implementation of this HPEA on a rotary arm is experimentally tested for position control accuracy, robustness, and friction compensation. The HPEA performance is compared to the results from the pneumatic actuator alone to demonstrate the superiority of the hybrid design.
- Chapter 4 studies a comprehensive controller structure that incorporates both the pneumatic and electric actuators and performs position control and force distribution/allocation effectively. This study emphasizes the importance of effective input allocation in a redundant actuator, like HPEA compared to independently controlled actuators. After developing a model for a linear motion HPEA-driven system, several novel MPC-based controllers are designed and simulated for simultaneously handling the position control and optimal input allocation problems. The results and comparisons indicate the importance of

optimal input allocation between the actuators, and the effects of taking different approaches in the allocation design.

- Chapter 5 presents the design and implementation of a HPEA-driven elbow joint that is added to the existing 1-DOF arm to create a 2-DOF planar HPEA-driven manipulator. The kinematic and kinetic models of the arm, as well as the geometry of the elbow joint are studied. The new joint and the two-DOF manipulator are experimentally tested.
- Chapter 6 concludes the thesis. It summarizes the important findings and provides recommendations for the continued research and development of HPEA-driven robots.

References

[1] Shen X, Zhang J, Barth EJ, Goldfarb M. Nonlinear Model-Based Control of Pulse Width Modulated Pneumatic Servo Systems. J Dyn Syst Meas Control 2005;128:663–9. https://doi.org/10.1115/1.2232689.

[2] Nguyen, T.; Leavitt, J.; Jabbari, F.; Bobrow JE. Accurate Sliding-Mode Control of Pneumatic Systems Using Low Cost Solenoid Valves. IEEE Trans Mechatronics 2007;12:216–9. https://doi.org/10.1109/TMECH.2007.892821.

[3] Bobrow JE, McDonell BW. Modeling, identification, and control of a pneumatically actuated, force controllable robot. IEEE Trans Robot Autom 1998;14:732–42. https://doi.org/10.1109/70.720349.

[4] Rao Z, Bone GM. Nonlinear modeling and control of servo pneumatic actuators. IEEE Trans Control Syst Technol 2008. https://doi.org/10.1109/TCST.2007.912127.

[5] Van Varseveld RB, Bone GM. Accurate position control of a pneumatic actuator using on/off solenoid valves. IEEE/ASME Trans Mechatronics 1997;2:195–204. https://doi.org/10.1109/3516.622972.

[6] Falcão Carneiro J, Gomes De Almeida F. Modeling pneumatic servovalves using neural networks. Proc 2006 IEEE Conf Comput Aided Control Syst Des CACSD 2007:790–5. https://doi.org/10.1109/CACSD.2006.285478.

[7] Pandian S. Control performance of an air motor. Int Conf Robot Autom 1999;14:518–24. https://doi.org/10.1109/ROBOT.1999.770029.

[8] Hodgson S, Tavakoli M, Pham MT, Leleve A. Nonlinear discontinuous dynamics averaging and pwm-based sliding control of solenoid-valve pneumatic actuators. IEEE/ASME Trans Mechatronics 2015;20:876–88. https://doi.org/10.1109/TMECH.2014.2326601.

[9] Rahman RA, He L, Sepehri N. Design and experimental study of a dynamical adaptive backstepping-sliding mode control scheme for position tracking and regulating of a low-cost pneumatic cylinder. Int J Robust Nonlinear Control 2016;26:853–75. https://doi.org/10.1002/rnc.3341.

[10] Bone GM, Chen X. Position control of hybrid pneumatic-electric actuators. Am Control Conf (ACC), 2012 2012:1793–9. https://doi.org/10.1016/j.mechatronics.2014.10.009.

[11] Bone GM, Xue M, Flett J. Position control of hybrid pneumatic-electric actuators using discrete-valued model-predictive control. Mechatronics 2015. https://doi.org/10.1016/j.mechatronics.2014.10.009.

[12] Ashby G, Bone GM. Improved hybrid pneumatic-electric actuator for robot arms, 2016. https://doi.org/10.1109/aim.2016.7576750.

[13] Tuvayanond W, Parnichkun M. Position control of a pneumatic surgical robot using PSO based 2-DOF H∞ loop shaping structured controller. Mechatronics 2017;43:40–55. https://doi.org/10.1016/j.mechatronics.2017.03.001.

[14] Chen Y, Godage IS, Tse ZTH, Webster RJ, Barth EJ. Characterization and control of a pneumatic motor for MR-conditional robotic applications. IEEE/ASME Trans Mechatronics 2017;22:2780–9. https://doi.org/10.1109/TMECH.2017.2767906.

[15] Shearer JL. Study of Pneumatic Processes in the Continuous Control of Motion With Compressed Air – I. Trans ASME n.d.:233–42.

[16] Richer E, Hurmuzlu Y. A high performance pneumatic force actuator system: Part I—nonlinear mathematical model. J Dyn Syst Meas Control Trans ASME 2000;122:416–25. https://doi.org/10.1115/1.1286336.

[17] Shu Ning, Bone GM. Development of a nonlinear dynamic model for a servo pneumatic positioning system. IEEE Int Conf Mechatronics Autom 2005 2005:43–8. https://doi.org/10.1109/ICMA.2005.1626520.

[18] Taheri B, Case D, Richer E. Force and stiffness backstepping-sliding mode controller for pneumatic cylinders. IEEE/ASME Trans Mechatronics 2014;19:1799–809. https://doi.org/10.1109/TMECH.2013.2294970.

[19] L. J. Petrosky. Hybrid Electro-Pneumatic Robot Joint Actuator. 478 225 828, n.d.

[20] Takemura F, Pandian SR, Nagase Y, Mizutani H, Hayakawa Y, Kawamura S. Control of a hybrid pneumatic/electric motor. IEEE Int. Conf. Intell. Robot. Syst., 2000. https://doi.org/10.1109/iros.2000.894606.

[21] Dongjun Shin, Sardellitti I, Khatib O. A hybrid actuation approach for human-friendly robot design 2008:1747–52. https://doi.org/10.1109/ROBOT.2008.4543453.

[22] Nakata Y, Noda T, Morimoto J, Ishiguro H. Development of a pneumatic-electromagnetic hybrid linear actuator with an integrated structure. 2015 IEEE/RSJ Int. Conf. Intell. Robot. Syst., IEEE; 2015, p. 6238–43. https://doi.org/10.1109/IROS.2015.7354267.

[23] Heinzmann J, Zelinsky A. Quantitative safety guarantees for physical human-robot interaction. Int J Rob Res 2003;22:479–504.

[24] Hirzinger G, Albu-Schäffer A, Hähnle M, Schaefer I, Sporer N. On a new generation of torque controlled light-weight robots. Proc - IEEE Int Conf Robot Autom 2001;4:3356–63. https://doi.org/10.1109/robot.2001.933136.

[25] Bicchi A, Tonietti G. Fast and "Soft-Arm" Tactics. IEEE Robot Autom Mag 2004;11:22–33. https://doi.org/10.1109/MRA.2004.1310939.

[26] Hyun D, Yang HS, Park J, Shim Y. Variable stiffness mechanism for human-friendly robots. Mech Mach Theory 2010. https://doi.org/10.1016/j.mechmachtheory.2010.01.001.

[27] Lauzier N, Gosselin C. Performance Indices for Collaborative Serial Robots With Optimally Adjusted Series Clutch Actuators. J Mech Robot 2012. https://doi.org/10.1115/1.4005723.

[28] Moghani M, Kermani MR. Design and development of a hybrid magneto-rheological clutch for safe robotic applications. Robot. Autom. (ICRA), 2016 IEEE Int. Conf., IEEE; 2016, p. 3083–8.

[29] Suita K, Yamada Y, Tsuchida N, Imai K, Ikeda H, Sugimoto N. A failure-to-safety" Kyozon" system with simple contact detection and stop capabilities for safe human-autonomous robot coexistence. Robot. Autom. 1995. Proceedings., 1995 IEEE Int. Conf., vol. 3, IEEE; 1995, p. 3089–96.

[30] De Luca A, Albu-Schaffer A, Haddadin S, Hirzinger G. Collision detection and safe reaction with the DLR-III lightweight manipulator arm. Intell. Robot. Syst. 2006 IEEE/RSJ Int. Conf., IEEE; 2006, p. 1623–30.

[31] Jeong S, Takahashi T. Impact force reduction of manipulators using a dynamic acceleration polytope and flexible collision detection sensor. Adv Robot 2009;23:367–83.

[32] Haddadin S, Laue T, Frese U, Wolf S, Albu-Schäffer A, Hirzinger G. Kick it like a

Safe Robot: Requirements for 2050. Rob Auton Syst 2009;57:761–75.

[33] Zeng L, Bone GM. Design of elastomeric foam-covered robotic manipulators to enhance human safety. Mech Mach Theory 2013. https://doi.org/10.1016/j.mechmachtheory.2012.09.010.

[34] Van Damme M, Vanderborght B, Verrelst B, Van Ham R, Daerden F, Lefeber D. Proxy-based sliding mode control of a planar pneumatic manipulator. Int J Rob Res 2009;28:266–84. https://doi.org/10.1177/0278364908095842.

[35] Johansen TA, Fossen TI. Control allocation - A survey. Automatica 2013;49:1087–103. https://doi.org/10.1016/j.automatica.2013.01.035.

[36] Härkegård O. Dynamic Control Allocation Using Constrained Quadratic Programming. J Guid Control Dyn 2004;27:1028–34. https://doi.org/10.2514/1.11607.

[37] Galeani S, Pettinari S. On dynamic input allocation for fat plants subject to multi-sinusoidal exogenous inputs. Proc IEEE Conf Decis Control 2014;2015-Febru:2396–403. https://doi.org/10.1109/CDC.2014.7039754.

[38] Löfberg J. YALMIP: A toolbox for modeling and optimization in MATLAB. Proc IEEE Int Symp Comput Control Syst Des 2004:284–9. https://doi.org/10.1109/cacsd.2004.1393890.

[39] Mattingley J, Boyd S. CVXGEN: A code generator for embedded convex optimization. Optim Eng 2012;13:1–27. https://doi.org/10.1007/s11081-011-9176-9.

[40] Hanger M, Johansen TA, Mykland GK, Skullestad A. Dynamic model predictive control allocation using CVXGEN. IEEE Int Conf Control Autom ICCA 2011:417–22. https://doi.org/10.1109/ICCA.2011.6137940.

[41] Teramae T, Noda T, Hyon SH, Morimoto J. Modeling and control of a Pneumatic-Electric hybrid system. IEEE Int. Conf. Intell. Robot. Syst., 2013. https://doi.org/10.1109/IROS.2013.6697061.

[42] Ishihara K, Morimoto J. An optimal control strategy for hybrid actuator systems: Application to an artificial muscle with electric motor assist. Neural Networks 2018. https://doi.org/10.1016/j.neunet.2017.12.010.

[43] Rouzbeh B, Bone GM, Ashby G. High-Accuracy Position Control of a Rotary Pneumatic Actuator. IEEE/ASME Trans Mechatronics 2018;23:2774–81. https://doi.org/10.1109/TMECH.2018.2870177.

[44] Rouzbeh B, Bone GM, Ashby G, Li E. Design, Implementation and Control of an Improved Hybrid Pneumatic-Electric Actuator for Robot Arms. IEEE Access 2019;7:14699–713. https://doi.org/10.1109/ACCESS.2019.2891532.

[45] Rouzbeh B, Bone GM. Optimal force allocation and position control of hybrid pneumatic-electric linear actuators. Actuators 2020. https://doi.org/10.3390/act9030086.

[46] Kim NH, Kim JM, Khatib O, Shin D. Design optimization of hybrid actuation combining macro-mini actuators. Int J Precis Eng Manuf 2017. https://doi.org/10.1007/s12541-017-0062-z.

[47] Findlay D, Jafarinasab M, Sirouspour S. Optimization-based design of a novel hybrid aerial/ground mobile manipulator. IEEE Int Conf Intell Robot Syst 2015;2015-Decem:2467–72. https://doi.org/10.1109/IROS.2015.7353712.

[48] Sharbafi MA, Shin H, Zhao G, Hosoda K, Seyfarth A. Electric-pneumatic actuator: A new muscle for locomotion. Actuators 2017. https://doi.org/10.3390/act6040030.

[49] Mori S, Tanaka K, Nishikawa S, Niiyama R, Kuniyoshi Y. High-Speed Humanoid Robot Arm for Badminton Using Pneumatic-Electric Hybrid Actuators. IEEE Robot Autom Lett 2019. https://doi.org/10.1109/LRA.2019.2928778.

[50] Craig JJ. Introduction to Modern Robotics: Mechanics, Planning, and Control. 2004.

[51] International Organization for Standardization. ISO/TS 15066:2016 - Robots and robotic devices - Collaborative robots. ISO/TC 299 Robot 2016.

Chapter 2. High Accuracy Position Control of a Rotary Pneumatic Actuator

Abstract

Rotary pneumatic actuators provide several advantages over electromechanical actuators (e.g., higher power-to-weight ratio, lower cost and inherent safety) but are generally inferior in terms of accuracy and robustness when closed-loop position controlled. This paper presents the modelling, controller design and experimental verification of a high accuracy position controlled rotary pneumatic actuator. A novel inverse valve model enables the development of a fast and precise inner-loop pressure control law. The outer-loop position control law combines feedback with model-based terms, including an adaptive friction compensator. The robust stability of the inner and outer subsystems is analyzed. Experimental results are included for rotating an arm in the vertical plane. The hardware features low-cost on/off solenoid valves and low-cost pressure sensors. For a multiple cycloidal reference trajectory covering a 90° range the root mean square error averaged over five tests was 0.156°. Steady-state errors less than or equal to 0.0045° were achieved for these moves and for moves as small as 0.045°. Robustness to unknown payloads was achieved using an improved payload estimator. For example, for a payload 53% less than nominal the root mean square error with the estimator was 75% less than without it. The experimental results are superior to those reported in the prior literature.

Index Terms: **Pneumatic actuators, position control, servosystems, on/off valves, friction compensation, nonlinear control systems, collaborative robots.**

2.1 Introduction

Pneumatic actuators are known for their high torque-to-weight ratio, low cost, and lack of thermal problems (such as overheating) compared with conventional electro-mechanical actuators. They are also inherently safer due to the natural compliance of air. This makes them well suited for applications where collisions with humans may occur, such as collaborative robots. On the other hand, their use of a highly compressible fluid to transfer

power and the presence of seal friction makes them much more difficult to model and precisely control than electromechanical actuators.

This challenging control problem has attracted extensive research interest both in past decades (e.g., [1]-[7]) and in recent years [8]-[14]. The majority of the previous research has been on the position control of actuators providing linear motion. We will use the term "rotary actuator" to refer to any actuator that rotates an output shaft or arm, including those employing cylinders and linear-to-rotary mechanisms; and vane-type actuators that rotate directly. Even though they are much more commonly used with robotic arms, relatively few researchers have investigated the position control of rotary pneumatic actuators.

Bobrow and McDonell [2] developed nonlinear model-based hierarchical control laws for the position control of a robotic arm with three rotary joints. Each joint was actuated by a pneumatic cylinder connected by cables to a pulley. A 5/3 servo valve was connected to each cylinder. Tracking errors as large as 4° were observed for 100° moves in their experiments. Pandian *et al*. [3] controlled a vane-type rotary actuator using two proportional valves and a model-based adaptive control law. Unfortunately, they did plot or not report any numerical values for the tracking errors. Much later, Bone and Chen [8] proposed a discrete-valued model-predictive control algorithm for pneumatic actuators driven by on/off solenoid valves. The hardware included two 3/2 solenoid valves, a pneumatic cylinder and a rack and pinion mechanism to produce the rotary motion. They also connected an electric motor in parallel with the pneumatic actuator to form a hybrid pneumatic-electric actuator. A maximum tracking error of 2.9° was achieved for a 115° vertical cycloidal trajectory experimentally using the pneumatic actuator alone. It is important to note that the robot arm was much smaller in [8] than in [2]. Rahman, He and Sepehri [10] controlled a rotary joint consisting of pneumatic cylinder connected to a link using pin joints. They utilized a 5/3 proportional valve and proposed an adaptive backstepping–sliding mode control law to control the position of the cylinder. Unfortunately, they only reported linear position control results. For a 0.1 Hz, 100 mm amplitude, sinusoidal reference trajectory the maximum tracking error was 5 mm. For a multiple-step polynomial trajectory the maximum tracking error was similar, and the

average SSE was 0.52 mm. In [11], improved hardware and the addition of a payload estimator allowed their rotary actuator to improve upon the position control results reported in [8]. It had a maximum pneumatic torque output of 9.0 Nm. For a 90° vertical cycloidal reference trajectory the root mean square error (RMSE) was 0.64° and the SSE was 0.23°. A much more powerful rotary actuator (with maximum pneumatic torque of 36.6 Nm) employing four pneumatic cylinders to drive a rack and pinion mechanism was presented by Ashby and Bone in [12]. As in [8] and [11] they used an electric motor in parallel with the pneumatic actuator for some of their experiments. The pneumatic actuator was controlled using two 3/2 on/off solenoid valves, an outer position control loop and two inner pressure control loops. The controller for the pneumatic actuator consisted of a model-based outer-loop position control law, an inner-loop linear feedforward plus feedback pressure control law (not model-based) and an adaptive friction compensator. When the pneumatic actuator was used alone, the arm followed a 90° vertical cycloidal trajectory with a RMSE of 0.096° and a SSE of 0.0045°. Tuvayanond and Parnichkun proposed an H_∞ loop shaping controller based on particle swarm optimization for a pneumatic robot arm with three joints [13]. The first joint used a rotary actuator consisting of two pistons driving rack gears meshed with a common pinion gear. The air flow was controlled by a 5/3 proportional valve. For a 60° reference trajectory the maximum error was 0.96° and the SSE was 0.3° or less. Chen *et al*. proposed a novel actuator combining a plastic vane-type pneumatic motor with a 100:1 gearbox for use in surgical robots [14]. The actuator was controlled using conventional proportional plus integral plus derivative feedback and a 5/3 proportional valve. For a 120° step reference inputs the RMSE was 0.9° and the SSE was 0.7°.

Note that the majority of these papers used proportional or servo valves [2][3][10][13][14]. These valves allow the air flow to be continuously varied making the position problem easier. However, they are much more expensive than on/off solenoid valves (e.g., U.S.$800 vs. U.S.$40). Since one of the benefits of pneumatic actuators is their low cost we will be using on/off valves like those used in [1][4][6][[8][11][12] in this paper even though they make precise position control more challenging.

This paper presents a significantly improved version of the position controlled rotary pneumatic actuator presented in [12]. Both the theoretical and experimental aspects have been improved. Regarding the theoretical aspect, the development of a novel inverse valve model motivated replacing the feedforward plus feedback control law used in the two inner-loop pressure controllers with a faster and more precise model-based control law. Robustness to unknown payloads is now provided by adding an improved version of the payload estimation algorithm from [11]. An analysis of the system's robust stability has also been added. Lastly, the experimental results included are all new and demonstrate superior performance. This paper is organized as follows. The system design and modelling are presented in section 2.2. In section 2.3 the controller design and stability analysis are presented. The offline payload estimation algorithm is described in section 2.4. The experimental hardware, procedure and results are presented in section 2.5. A comparison with prior work is given in section 2.6, followed by conclusions in section 2.7.

2.2 System Design and Modeling

The design of the rotary pneumatic actuator and arm are shown in Figure 2.1. The arm rotates in the vertical plane and the actuator is designed to produce the large torques needed to overcome gravity. Four rodded cylinders are symmetrically distributed with respect to the top-bottom and left-right directions. The top pair and bottom pair of cylinders are each connected to a rack gear which is meshed with a pinion gear directly rotating the joint. The rack gears translate on spring-loaded ball rollers to minimize friction and gear backlash. The arm is rigidly connected to the joint. Various payloads can be bolted to the end of the arm. A counterweight balances the arm's gravity torque when no payload is attached. The eight chambers inside the four cylinders are grouped into two chamber groups (CGs): chamber group 1 (CG1) is the combination of the four chambers that push the arm up when pressurized, and vice versa for chamber group 2 (CG2). Each CG is connected to a pair of PWM-driven 2/2 on-off solenoid valves. This four-valve pneumatic circuit allows each CG to be pressurized and discharged independently. There are pressure sensors to measure each CG's pressure and an encoder connected to the joint to measures the arm's angle. The angle, θ, is defined as zero when the arm is pointing vertically straight down. Figure 2.2

shows a detailed view of the actuator components located inside the housing. The ball rollers are not shown. Further explanations of the mechanical design are provided in [12] and [15].

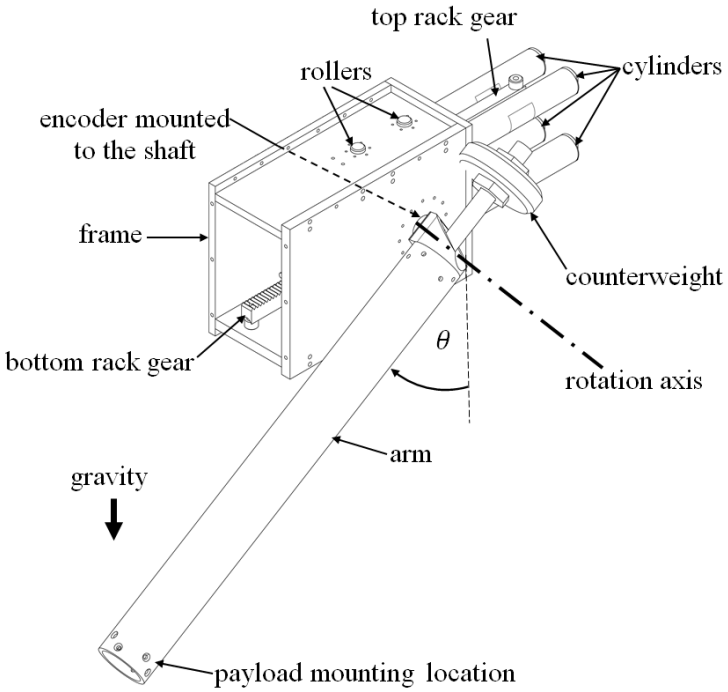

Figure 2.1 Assembly drawing of the pneumatic rotary actuator and arm.

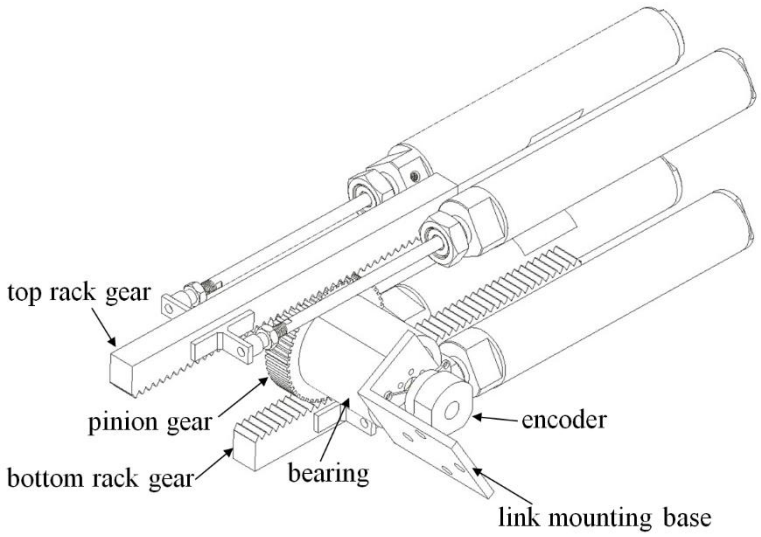

Figure 2.2 Detailed view of the actuator components located inside the housing.

The mathematical equation governing the arm's position is given in (2.1).

$$\tau_{\mathrm{p}} - \tau_{\mathrm{g}} - \tau_{\mathrm{f}} = I_{\mathrm{total}}\ \ddot{\theta} \tag{2.1}$$

where τ_{p}, τ_{g}, τ_{f}, I_{total}, and $\ddot{\theta}$ are the pressure torque, gravity torque, friction torque, total moment of inertia, and arm's angular acceleration, respectively. The pressure and gravity torques are defined by (2.2) and (2.3). In these equations r_{gear}, m_{payload}, g, and L are the pinion gear radius, payload mass, gravitational acceleration, and arm length, respectively. P_1 and P_2 are the pressures of each CG, and $A_{\mathrm{cg}} = 4A_{\mathrm{p}} - 2A_{\mathrm{r}}$ is the total cross-sectional area of each CG, in which A_{p} is the cross-sectional area of each piston and A_{r} is the cross-sectional area of each rod. Note that each CG consists of two rodless sides and two rodded sides of the four cylinders, so the forces from the atmospheric pressure on the rods cancel each other out.

$$\tau_{\mathrm{p}} = \left(P_1 - P_2\right) A_{\mathrm{cg}} r_{\mathrm{gear}} = \Delta P A_{\mathrm{cg}} r_{\mathrm{gear}} \tag{2.2}$$

$$\tau_{\mathrm{g}} = m_{\mathrm{payload}} \mathrm{g} L \sin(\theta) \tag{2.3}$$

Modeling friction is a challenge in mechanical systems due to its complex and uncertain nature. A simple model, that will form the basis of the adaptive friction compensator described in section III, is employed in this research. The model of the friction torque is given by (2.4).

$$\tau_{\mathrm{f}} = \begin{cases} \tau_{\mathrm{f}}^{+} & \dot{\theta} > 0 \\ 0 & \dot{\theta} = 0 \\ \tau_{\mathrm{f}}^{-} & \dot{\theta} < 0 \end{cases} \tag{2.4}$$

Considering the ideal gas law, conservation of mass, and conservation of energy for each CG, leads to (2.5) and (2.6) for the mass flow rate and its time derivative. Here v is the CG volume, P is the CG pressure, T is the absolute temperature of the air, k is the ratio of specific heats of air, and R is the universal gas constant.

$$\dot{m} = \left(\mathrm{k}P\dot{v} + \dot{P}v\right) \Big/ \left(\mathrm{k}\mathrm{R}T\right) \tag{2.5}$$

$$\ddot{m} = \left(\mathrm{k}P\ddot{v} + \ddot{P}v + (1+\mathrm{k})\dot{P}\dot{v}\right) \Big/ \mathrm{k}\mathrm{R}T \tag{2.6}$$

Mass flow rate also depends on the flow through the PWM-driven supply and discharge valves. Assuming the supply pressure, P_{s}, and atmospheric pressure, P_0, are constant, the relationships between the mass flow rates into the CGs and the valve inputs are defined by (2.7).

$$\begin{cases} \dot{m}_1 = f_1(u_1, P_1) \\ \dot{m}_2 = f_2(u_2, P_2) \end{cases} \tag{2.7}$$

In (2.7), u_1 and u_2 are the commanded PWM duty cycles for the supply valves for CG1 and CG2, respectively. The duty cycles for the CG1 and CG2 discharge valves are simply defined as: $1-u_1$ and $1-u_2$. The functions f_1 and f_2 depend on the valve's internal geometry and are highly nonlinear. Combining (2.5) and (2.7), the pressure derivative models for CG1 and CG2 in (2.8) are obtained.

$$\begin{cases} \dot{P}_1 = \left(f_1\left(u_1, P_1\right)\mathrm{k}\mathrm{R}T - \mathrm{k}P_1\dot{v}_1 \right)/v_1 \\ \dot{P}_2 = \left(f_2\left(u_2, P_2\right)\mathrm{k}\mathrm{R}T - \mathrm{k}P_2\dot{v}_2 \right)/v_2 \end{cases} \tag{2.8}$$

Where:

$$\begin{cases} v_1 = v_{01} + A_{\mathrm{cg}} r_{\mathrm{gear}} \theta \\ v_2 = v_{02} - A_{\mathrm{cg}} r_{\mathrm{gear}} \theta \end{cases} \tag{2.9}$$

In (2.9), v_{01} and v_{02} are the CG1 and CG2 volumes at $\theta = 0$, respectively.

2.3 Controller Design

The overall system controls the position, velocity and acceleration of the arm by manipulating the duty cycles of the valves. This is broken into three subsystems. Hence, three controllers are designed: inner-loop pressure controllers for CG1 and CG2; and an outer-loop position controller. Figure 2.3 shows the structure of the subsystems within the overall system.

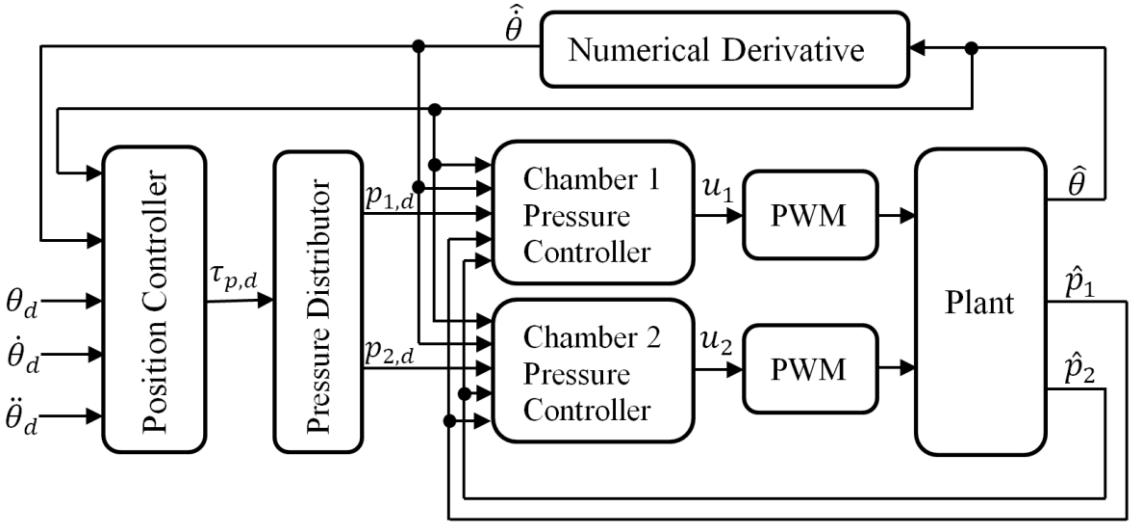

Figure 2.3 Overall control system and its subsystems.

2.3.1 Model-based Position Controller

The position controller is the outer-loop controller, receiving the measured and desired position and their derivatives; and outputting the desired pressure to the inner- loop

pressure controllers. It includes feedforward terms based on (2.1) to (2.3) to provide a rapid response, and feedback terms to provide robustness. The control law is as follows.

$$\tau_{\mathrm{p,d}}(t_i) = \hat{I}_{\mathrm{total}}\ddot{\theta}_{\mathrm{d}}(t_i) + \hat{\tau}_{\mathrm{g}}(t_i) + \tau_{\mathrm{f}}{}^{*}(t_i) - K_P\hat{e}_{\theta} - K_D\hat{\dot{e}}_{\theta} \tag{2.10}$$

where $t_i = iT_s, i \in \mathbf{Z}^+$ is the time of the current sample; $\hat{I}_{\mathrm{total}}\ddot{\theta}_{\mathrm{d}}(t_i)$, $\hat{\tau}_{\mathrm{g}}(t_i)$ and $\tau_{\mathrm{f}}{}^{*}(t_i)$ are the inertia, gravity and adaptive friction compensation terms, respectively; $\hat{e}_{\theta} = \hat{\theta}(t_i) - \theta_{\mathrm{d}}\ (t_i)$ is the position error, $\hat{\dot{e}}_{\theta} = \hat{\dot{\theta}}(t_i) - \dot{\theta}_{\mathrm{d}}(t_i)$ is the velocity error, $\hat{\theta}\left(t_i\right)$ is the sensed position; $\hat{\dot{\theta}}(t_i)$ is the estimated velocity; K_P is the positive proportional gain; K_D is the positive derivative gain; and the symbol " ˆ " denotes the measured or estimated value for the variable. $\hat{\dot{\theta}}(t_i)$ is estimated by backward differencing and low-pass filtering the sensed position. Equation (2.11) shows how the friction compensation torque is calculated. When the desired velocity is zero, $\tau_{\mathrm{f}}{}^{*}(t_i)$ is adjusted until the position error magnitude is less than the threshold δ. λ^+ and λ^- are positive constants that define the torque adaptation step sizes for positive and negative errors, respectively. Note that in (2.11) $\dot{\theta}_{\mathrm{d}}(t_i)$ is used instead of $\hat{\dot{\theta}}(t_i)$. This choice disagrees with the physics of friction, but has the advantage of avoiding the detrimental effects of a noisy velocity estimate, especially near $\dot{\theta} = 0$.

$$\tau_f{}^{*}(t_i) = \begin{cases} \tau_f{}^{+} & \dot{\theta}_d(t_i) > 0 \\ \tau_f{}^{-} & \dot{\theta}_d(t_i) < 0 \\ \tau_f{}^{*}(t_{i-1}) & \dot{\theta}_d(t_i) = 0 \wedge \left|\hat{e}_\theta(t_i)\right| \le \delta \\ \tau_f{}^{*}(t_{i-1}) - \lambda^+ & \dot{\theta}_d(t_i) = 0 \wedge \hat{e}_\theta(t_i) > \delta \wedge \\ & \tau_f{}^{*}(t_{i-1}) > \tau^*_{f,min} \\ \tau_f{}^{*}(t_{i-1}) + \lambda^- & \dot{\theta}_d(t_i) = 0 \wedge \hat{e}_\theta(t_i) < -\delta \wedge \\ & \tau_f{}^{*}(t_{i-1}) < \tau^*_{f,max} \end{cases} \tag{2.11}$$

The desired pressure difference is calculated from the desired torque via (2.12).

$$\Delta P_{\mathrm{d}}(t_i) = \tau_{\mathrm{p,d}}(t_i) \Big/ \left(A_{\mathrm{cg}} r_{\mathrm{gear}} \right) \tag{2.12}$$

Obviously, infinite combinations of $P_{1,\mathrm{d}}$ and $P_{2,\mathrm{d}}$ can provide the same pressure difference. The strategy used in this paper is to keep the average of the two desired CG pressures equal to the average of the atmospheric and supply pressures. The desired pressures are then given by (2.13) and (2.14). This strategy tends to keep both CG at pressures above atmospheric, which we have found improves the position tracking performance.

$$P_{1,\mathrm{d}}(t_i) = \tfrac{1}{2}\left(P_0 + P_{\mathrm{s}} + \Delta P_{\mathrm{d}}(t_i) \right) \tag{2.13}$$

$$P_{2,\mathrm{d}}(t_i) = \tfrac{1}{2}\left(P_0 + P_{\mathrm{s}} - \Delta P_{\mathrm{d}}(t_i) \right) \tag{2.14}$$

2.3.2 Inverse Valve Models

An inverse valve model is required for the model-based pressure controller. The typical approach in the literature is to fit a forward valve model that is linear or quadratic in u and then solve it for the unknown u given the desired mass flow rate(s) and measured chamber pressure(s), volume(s) and volume time derivative(s) e.g. [2][4][7]. A few researchers have fit a neural network as an inverse valve model, e.g, [5].

To avoid having to simplify the forward model to make it invertible, and also avoid the training difficulties (e.g., data hungry, local minima and overfitting) associated with neural networks, a different approach is proposed in this paper. Here the inverse behavior of each valve is modelled by a polynomial in three variables as follows:

$$\begin{cases} u_1(t_i) = f_{1inv}\left(\hat{\dot{m}}_{1\mathrm{d}}(t_i), \hat{\ddot{m}}_{1\mathrm{d}}(t_i), \hat{P}_1(t_i) \right) \\ u_2(t_i) = f_{2inv}\left(\hat{\dot{m}}_{2\mathrm{d}}(t_i), \hat{\ddot{m}}_{2\mathrm{d}}(t_i), \hat{P}_2(t_i) \right) \end{cases} \tag{2.15}$$

$$f_{1inv} = \sum_{\alpha=0}^{A}\sum_{\beta=0}^{B}\sum_{\gamma=0}^{G} C_{\alpha,\beta,\gamma}\, \hat{\dot{m}}_{1\mathrm{d}}(t_i)^{\alpha}\, \hat{\dot{m}}_{1\mathrm{d}}(t_i)^{\beta}\, \hat{P}_1(t_i)^{\gamma}$$
$$f_{2inv} = \sum_{\alpha=0}^{A}\sum_{\beta=0}^{B}\sum_{\gamma=0}^{G} C_{\alpha,\beta,\gamma}\, \hat{\dot{m}}_{2\mathrm{d}}(t_i)^{\alpha}\, \hat{\dot{m}}_{2\mathrm{d}}(t_i)^{\beta}\, \hat{P}_2(t_i)^{\gamma} \qquad (2.16)$$

where $\hat{P}$ are the sensed pressures, $\hat{\dot{m}}_d$ are the desired mass flow rates and $\hat{\ddot{m}}_d$ are the desired mass flow rate time derivatives for the CGs. The inclusion of $\hat{\ddot{m}}_d$ in (2.16) was found to improve the fit of the model when rapid changes in $\dot{m}$ occurred. The optimal coefficients $C_{\alpha,\beta,\gamma}$ may be found by linear regression, avoiding the possibility of local minima.

2.3.3 Model-based Pressure Controller

With the inverse valve model known, a control law based on feedback linearization will be used to control the highly nonlinear CG pressures. The pressure controller equations (2.17)-(2.19) are derived by considering $\dot{P}$ as the equivalent input and adding proportional plus integral feedback to provide robustness as follows:

$$\tilde{\dot{P}}(t_i) = \dot{P}_{\mathrm{d}}(t_i) - K_p{}'\hat{e}_P(t_i) - K_I\hat{E}_P(t_i) \qquad (2.17)$$

Where $\hat{e}_{\mathrm{p}}(t_i) = \hat{P}(t_i) - P_{\mathrm{d}}(t_i)$ is the pressure error; $\hat{E}_P = \int_0^t \hat{e}_p dt$; and $K_p{}'$ and K_I are positive proportional and integral gains, respectively. In (2.17), $\hat{E}_P(t_i)$ is bounded to avoid integral windup. Equations (2.18) and (2.19) are then derived using feedback linearization with (2.5), (2.6) and (2.17).

$$\hat{\dot{m}}_{\mathrm{d}}(t_i) = \left(\mathrm{k}\hat{P}(t_i)\hat{v}(t_i) + \tilde{\dot{P}}(t_i)\hat{v}(t_i)\right)\Big/\mathrm{k}RT \qquad (2.18)$$

$$\hat{\dot{m}}_{\mathrm{d}}(t_i) = \left(\mathrm{k}\hat{P}(t_i)\dot{\hat{v}}(t_i) + \ddot{P}_d(t_i)\hat{v}(t_i) + (1+\mathrm{k})\tilde{\dot{P}}(t_i)\hat{v}(t_i) \right) \Big/ \mathrm{kR}T \tag{2.19}$$

Finally, the valve duty cycles can be calculated by substituting the values from (2.18) and (2.19), and the sensed pressures, into (2.15).

2.3.4 Analysis of Robust Stability

To prove the robust stability of the position controller it is first necessary to prove the robust stability of the inner-loop pressure controllers. Defining uncertainties $\Delta\dot{P} = \tilde{\dot{P}} - \dot{P}$ and $\Delta P = \hat{P} - P$, from (2.17) we obtain:

$$\dot{e}_p + K_p{}' e_p = \Delta U_1 \tag{2.20}$$

$$\Delta U_1 = \Delta\dot{P} - K_p{}'\Delta P - K_I \hat{E}_p \tag{2.21}$$

Since bounded integral action controller was used in (2.17), the term $K_I \hat{E}_p$ is bounded. The bound on $\Delta\dot{P}$ depends on the accuracy of the inverse valve model, where a better accuracy will give a tighter bound. ΔP is the uncertainty of the pressure measurement which is also bounded. Therefore, the total uncertainty, ΔU_1, is bounded. Since $K_p{}' > 0$, (2.20) shows that e_p is guaranteed to converge within a bounded region; thus the pressure subsystem is bounded-input bounded-output stable. This statement applies to the subsystems for both chambers, so both $e_{\mathrm{p},1}$ and $e_{\mathrm{p},2}$ will be bounded for a bounded input.

Now the stability of the position control subsystem will be proven. If $\Delta\tau_{\mathrm{p}} = \tau_{\mathrm{d}} - \tau_{\mathrm{p,d}}$ is defined as the pneumatic torque uncertainty, substitution into (2.2) gives:

$$\begin{aligned} \Delta\tau_{\mathrm{p}} &= \left(P_1 - P_2\right) A_{\mathrm{cg}} r_{\mathrm{gear}} - \left(P_{1,\mathrm{d}} - P_{2,\mathrm{d}}\right) A_{\mathrm{cg}} r_{\mathrm{gear}} \\ &= \left(e_{\mathrm{p},1} - e_{\mathrm{p},2}\right) A_{\mathrm{cg}} r_{\mathrm{gear}} \end{aligned} \tag{2.22}$$

Equation (2.22) shows that $\Delta\tau_{\mathrm{p}}$ is also bounded. Re-writing (2.10) gives:

$$\tau_{\mathrm{p}} = \hat{I}_{\mathrm{total}}\ddot{\theta}_{\mathrm{d}} + \hat{\tau}_{\mathrm{g}} + \tau_{\mathrm{f}}^{*} - K_p(\hat{e}_{\theta}) - K_D(\hat{\dot{e}}_{\theta}) + \Delta\tau_{\mathrm{p}} \tag{2.23}$$

The remaining bounded uncertainties are defined by $\Delta\theta = \hat{\theta} - \theta$, $\Delta\dot{\theta} = \hat{\dot{\theta}} - \dot{\theta}$, $\Delta I_{\mathrm{total}} = \hat{I}_{total} - I_{\mathrm{total}}$, $\Delta\tau_{\mathrm{g}} = \hat{\tau}_{\mathrm{g}} - \tau_{\mathrm{g}}$, and $\Delta\tau_{\mathrm{f}} = \tau_{\mathrm{f}}^{*} - \tau_{\mathrm{f}}$. Substituting τ_p from (2.1) into (2.23) leads to (2.24) and (2.25).

$$I_{\mathrm{total}}\ddot{e}_{\theta} + K_D\dot{e}_{\theta} + K_{\mathrm{p}}e_{\theta} = \Delta U_2 \tag{2.24}$$

$$\Delta U_2 = \Delta\tau_{\mathrm{p}} + \Delta I_{\mathrm{total}}\ddot{\theta}_{\mathrm{d}} + \Delta\tau_{\mathrm{f}} + \Delta\tau_{\mathrm{g}} - K_p\Delta\theta - K_D\Delta\dot{\theta} \tag{2.25}$$

The total uncertainty ΔU_2 for the position subsystem is made up of bounded terms so it is also bounded. Since $I_{\mathrm{total}} > 0$, $K_D > 0$, and $K_p > 0$, (2.24) guarantees that e_{θ} converges inside a bounded region when inputs θ_{d}, $\dot{\theta}_{\mathrm{d}}$, and $\ddot{\theta}_{\mathrm{d}}$ are bounded. So the position control subsystem is bounded-input bounded-output stable.

2.4 Offline Payload Estimation

The advantages of model-based controllers can be undermined by uncertainties in the system dynamics. In this system the uncertainty of friction is addressed by the adaptive friction compensator. The other major source of uncertainty occurs when the arm is carrying an unknown payload. A payload estimation algorithm was presented in [11] to improve the controller's performance with unknown payloads. In this section an improved algorithm that produces more accurate estimates in the presence of actuator friction is proposed. In the context of rotary motion, the unknown payload contributes an unknown moment of inertia. Its estimate is denoted as $\hat{I}_{\mathrm{payload}}$. The estimation algorithm is as follows.

1. Choose an initial estimate, $\hat{I}_{\mathrm{payload}}(0)$. A value of zero can be used if no information about the payload is available.
2. Start stage 1 by moving the arm upward with constant low speed and go to step 4.
3. Start stage 2 by moving the arm downward with constant low speed.

4. Calculate the estimated total system inertia, $\hat{I}_{\text{total}}(t_i)$, by summing $\hat{I}_{\text{payload}}(t_i)$ with the inertias of the unloaded arm and actuator components.
5. Compute the torque error, τ_{e}, using:

$$\tilde{\tau}_{\text{g}} = \hat{I}_{\text{payload}}(t_i) g \sin\hat{\theta}(t_i) \big/ L \tag{2.26}$$

$$\tau_{\text{e}}(t_i) = \hat{I}_{\text{total}}(t_i)\ddot{\theta}_{\text{d}}(t_i) + \tilde{\tau}_{\text{g}}(t_i) + \tau_{\text{f}}^{*}(t_i) - \hat{\tau}_{\text{p}}(t_i) \tag{2.27}$$

6. If $\left|\tau_{\text{e}}(t_i)\right| < \tau_{\text{e,threshold}}$ or $\left|\sin\hat{\theta}(t_i)\right| < S_{threshold}$ then go to step 9.
7. Obtain the raw estimate, $\hat{I}^{*}_{\text{payload}}$, using (2.28) and (2.29).

$$\hat{\tau}_{\text{g}}(t_i) = \hat{\tau}_{\text{p}}(t_i) - \hat{I}_{\text{total}}(t_i)\ddot{\theta}_{\text{d}}(t_i) \tag{2.28}$$

$$\hat{I}^{*}_{\text{payload}}(t_i) = \hat{\tau}_{\text{g}}(t_i) L \big/ g \sin\hat{\theta}(t_i) \tag{2.29}$$

8. If $0 \le \hat{I}^{*}_{\text{payload}}(t_i) \le I_{\text{payload,max}}$ then update the smoothed estimate using (2.30), else go to step 9.

$$\hat{I}_{\text{payload}}(t_{i+1}) = C_f \hat{I}_{\text{payload}}(t_i) + (1 - C_f)\hat{I}^{*}_{\text{payload}}(t_i) \tag{2.30}$$

where C_f is a forgetting factor and $0 \le C_f \le 1$.

9. Re-use the prior estimation as $\hat{I}_{\text{payload}}(t_{i+1}) = \hat{I}_{\text{payload}}(t_i)$.
10. When stage 1 finishes, save $\hat{I}_{\text{payload}}(t_{i+1})$ as κ_1 and go to step 3; otherwise continue.
11. When stage 2 finishes, save $\hat{I}_{\text{payload}}(t_{i+1})$ as κ_2 and continue, otherwise go to step 4 to start the next iteration.
12. Calculate final estimate as $\hat{I}_{\text{payload}} = \frac{1}{2}(\kappa_1 + \kappa_2)$.

13. Stop.

The idea behind the payload estimation algorithm is to estimate the payload inertia from the estimated gravity torque. The two stage estimation strategy allows it to succeed without precise prior knowledge of the friction torque. The algorithm initially estimates the payload torque plus friction torque while moving in two opposite directions. It assumes that the magnitude of the friction torques during the slow constant speed trajectories in steps 2 and 3 are identical in magnitude but opposite in sign due to the change in direction. The values the estimate converges to while moving upward and downward are recorded as κ_1 and κ_2 , respectively. In theory $\kappa_1 = I_{\text{payload}} + \psi$ and $\kappa_2 = I_{\text{payload}} - \psi$ where ψ is the estimation error caused by friction. The effect of friction is then mitigated using $\hat{I}_{\text{payload}} = \frac{1}{2}(\kappa_1 + \kappa_2)$ in step 12. Note that since the estimation is not performed online it does not affect the stability of the closed-loop system.

2.5 Experiments

2.5.1 Hardware

The control system hardware consists of four Festo MHJ10 2/2 on/off solenoid valves, two SSI Technologies P51 pressure sensors, a Quantum Devices QR12-20000 encoder, and four SMC NCMB106 low-friction air cylinders. With quadrature counting the encoder provides 80,000 counts/rev. Since it is directly coupled to the output shaft the resolution of the position measurement is $0.0045°$. A National Instruments PCI-6602 DAQ board, and a PC with an Intel i5 2400 3.1 GHz processor are used for data acquisition and control. The sampling periods and PWM periods were 1 ms and 2 ms, respectively. The supply pressure was set to 0.48 MPa absolute. Figure 2.4 shows the rotary actuator. A nominal payload mass (not visible in Figure 2.4) of 1.4 kg was attached to the end of the 0.7 m arm, making the nominal payload's moment of inertia equal to 0.69 kgm^2.

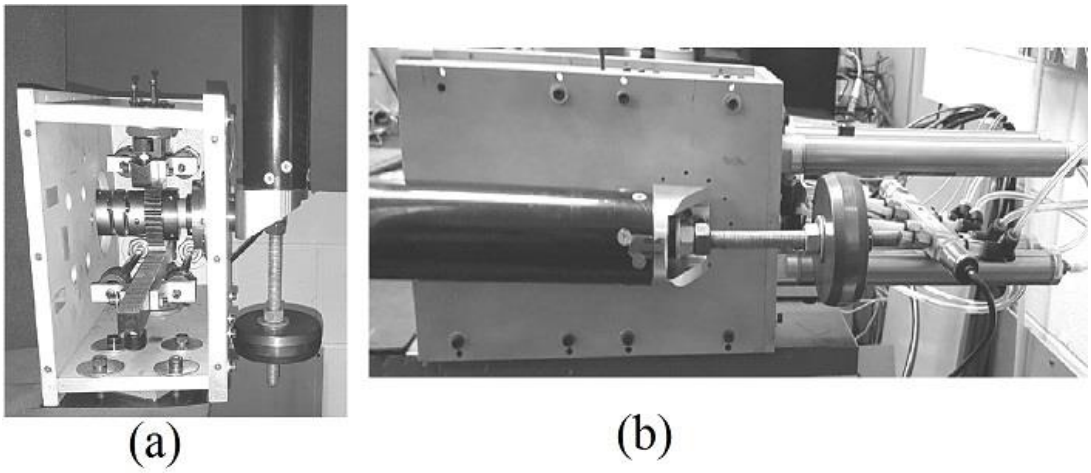

Figure 2.4 Rotary pneumatic actuator and partial view of the 0.7 m long arm used for the experiments when: (a) θ=180°, and (b) θ=90°.

2.5.2 Identification of Inverse Valve Models

The inverse valve models have to be identified before the pressure control loops can be implemented. To cover a large range of operating conditions 180 random values of duty cycle were used in the test for each valve. These random values were passed through a zero order hold with predefined period of 0.5 s. This period was chosen to allow the pressures to reach steady state before applying new u values. To perform the identification tests safely, the arm was fixed at the midrange angle, $\theta = 90°$. Backlash was negligible due to the preload applied to the meshing gears. Thus the CG volume could be considered constant which made $\dot{m}$ and $\ddot{m}$ proportional to $\dot{P}$ and $\ddot{P}$, respectively. $\hat{P}_1$ and $\hat{P}_2$ were continuously recorded during the test. After collecting the data and computing $\dot{m}$ and $\ddot{m}$ the coefficients of the polynomials in (2.16) were calculated using least squares. The orders were chosen as the smallest values that yielded an acceptable fitting error. This kept the models parsimonious and avoided overfitting. The chosen values were A=1, B=3, and G=3; and the fit had RMSE values of 3.7% and 4.1% for u_1 and u_2, respectively.

2.5.3 Performance of the Pressure Control Loops

The inner-loop pressure controllers must be implemented before the outer-loop position controller. In normal operation the position controller supplies the desired pressure values for each of the CGs to control the arm motion. In its absence the arm was fixed at $\theta = 90°$ and a smooth desired pressure trajectory was used with one CG, while the other CG was maintained at atmospheric pressure. The gains in (2.17) were manually tuned. Figure 2.5 shows a pressure control result for CG1. Averaged over five experiments, the pressure tracking resulted in an RMSE of 1.18 kPa (or 0.29% of $\max(P_{1d})$) and Maximum Absolute Error (MaxAE) of 2.86 kPa (or 0.71%). Similar performance was obtained with CG2.

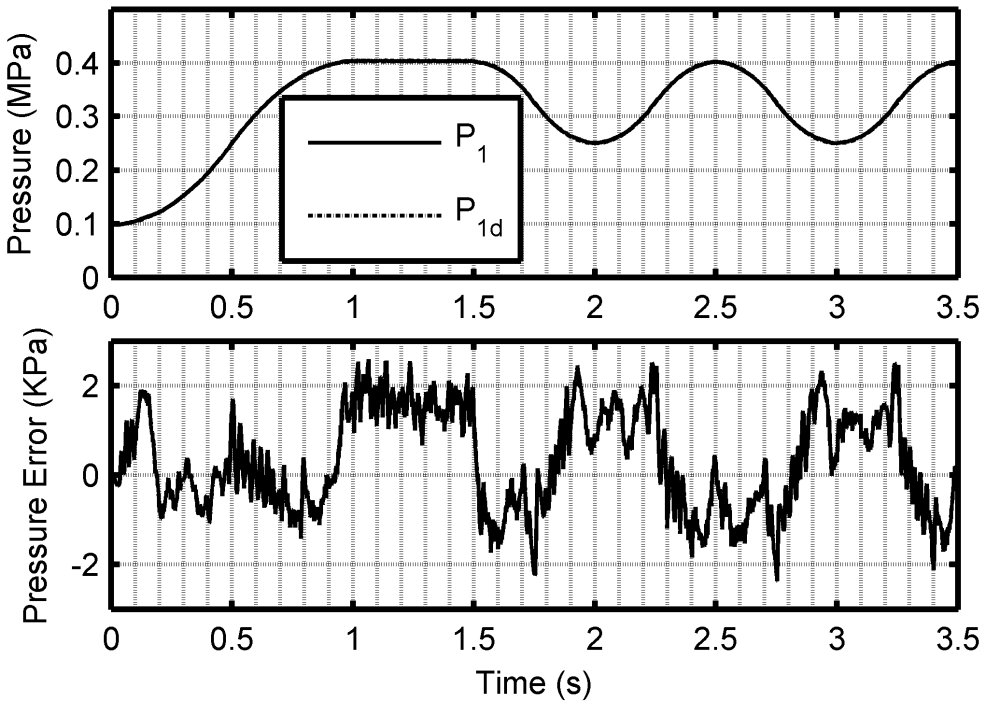

Figure 2.5 Pressure control results for CG1.

2.5.4 Performance of the Position Control

After finalizing the pressure loop gains, the parameters of the position controller (2.10) and adaptive friction compensator (2.11) were manually tuned based on numerous experiments.

The position tracking performance was then tested for a variety of challenging reference trajectories.

Sinusoidal reference trajectories are commonly used to evaluate the tracking control performance of position controlled pneumatic actuators, e.g., [6]-[10]. Position control results for 0.5 Hz and 1 Hz trajectories are shown in Figure 2.6. Averaged over five tests, for the 1 Hz case the RMSE and MaxAE were 0.736° and 1.280° respectively, and for the 0.5 Hz case the RMSE and MaxAE were 0.299° and 0.547° respectively.

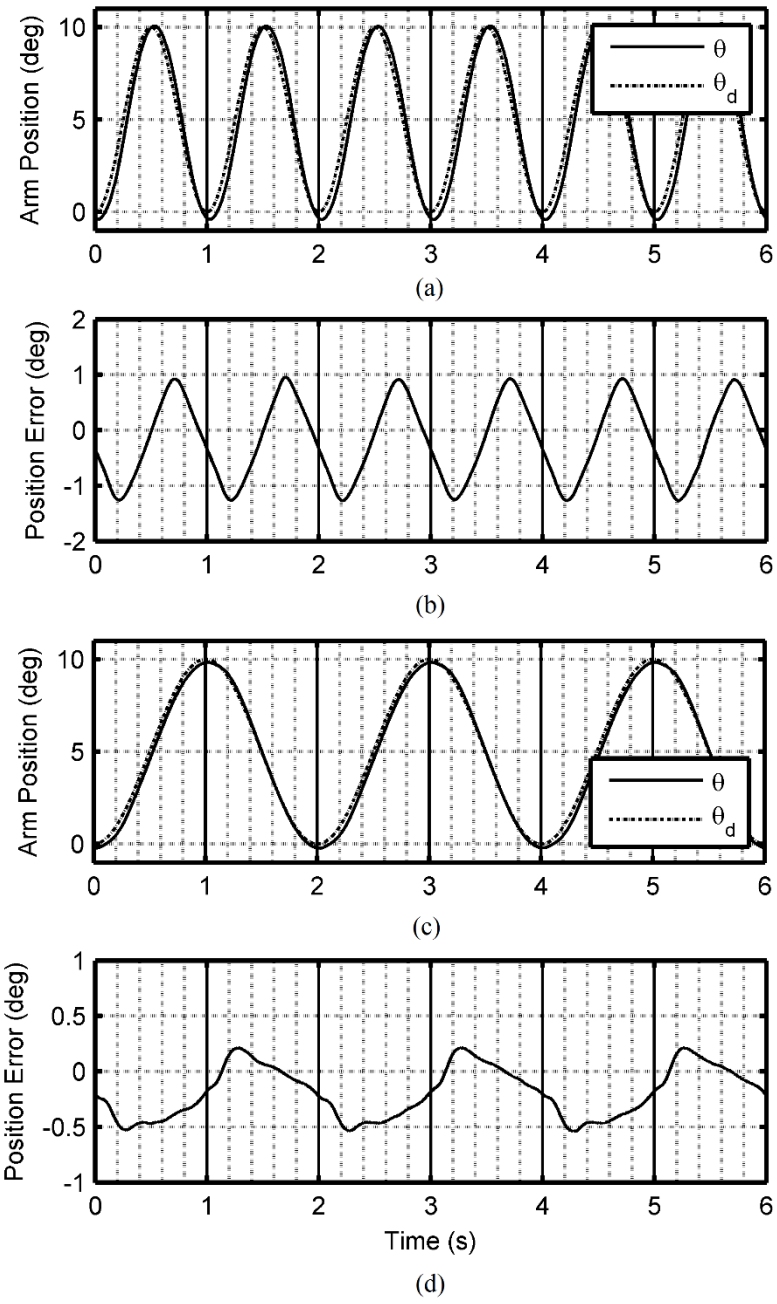

Figure 2.6 Tracking results for sinusoidal reference position trajectories. (a) 1 Hz tracking, (b) 1 Hz position error, (c) 0.5 Hz tracking, and (d) 0.5 Hz position error.

Figure 2.7 shows the position controller response for a multiple cycloidal desired trajectory. This trajectory allows both the transient and steady-state performances to be evaluated. Note that one of the steady-state sections is at $\theta = 90°$ since the maximum

gravity torque occurs at this arm angle. The plotted curves are the desired and sensed positions, position tracking error and pressures of CG1 and CG2. SSE values of 0.0045° or less were achieved consistently. Averaged over five experiments, an RMSE of 0.156° and MaxAE of 0.500° were achieved. For the pressure controller, the averages were RMSE of 0.74 kPa and 0.64 kPa; and MaxAE of 7.90 kPa and 8.47 kPa, for CG1 and CG2 respectively. The pressure tracking errors are larger than those reported in section V.*C* since the arm was moving and the desired pressure trajectory changed much more rapidly in these experiments.

Performing small moves is difficult for servo systems due to the effects of stiction. To further challenge the position controller we added a 0.045° move away from $\theta_d = 90°$ during time = 3 to 5 s. Recall that the actuator is also being subject to the maximum gravity torque at this arm angle. The response plotted in Figure 2.8 shows that the actuator is able to perform this tiny move in both directions with SSE values of 0.0045° or less. The SSE performance for this move and for the other much larger moves demonstrate the contributions of the adaptive friction compensator and pressure controllers.

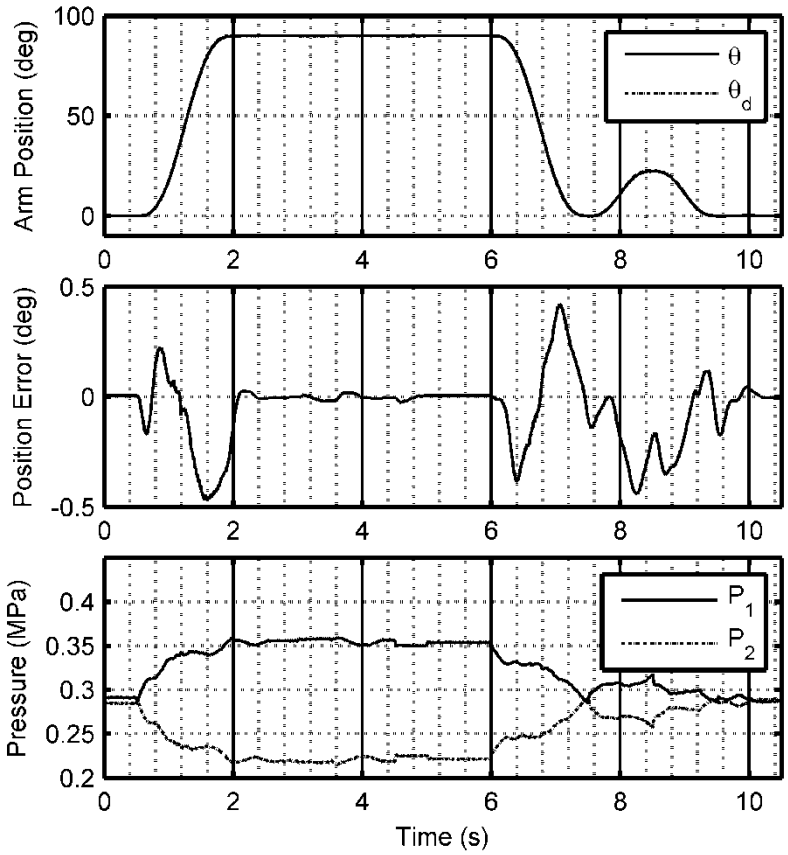

Figure 2.7 Position control performance when tracking a multiple cycloidal trajectory.

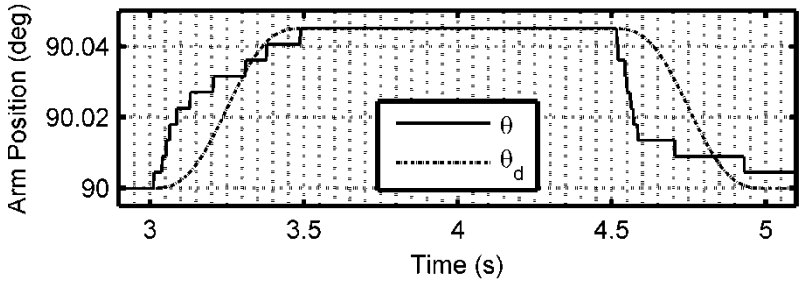

Figure 2.8 Magnified view of the 0.045° move added to the multiple cycloidal trajectory from time = 3 to 5 s.

2.5.5 Robustness to Unknown Payloads

To test the controller robustness to unknown payloads, two alternate payloads were used, one with a 53% decrease, and the other with a 34.7% increase in inertia relative to the

nominal value. Figure 2.10 shows the tracking error with and without using the payload estimator beforehand when following a multiple cycloidal trajectory. The reference trajectory (not shown) was identical to the one in Figure 2.7 except that the 2 s 0.045° movement section was not included. Table 2.1 lists the numerical results for different test conditions, averaged over five experiments. These results clearly demonstrate the improved position tracking that occurs when the offline payload estimator is used. Figure 2.9 shows the output of the inertia estimation algorithm during a sample experiment. Applying step 12 of the algorithm to the plotted values, the final estimate is given by $\hat{I}_{\text{payload}} = \frac{1}{2}(\kappa_1 + \kappa_2) = 0.86$ kgm^2. The actual inertia of the payload was 0.83 kgm^2 so the estimation error with this experiment was 4.1%.

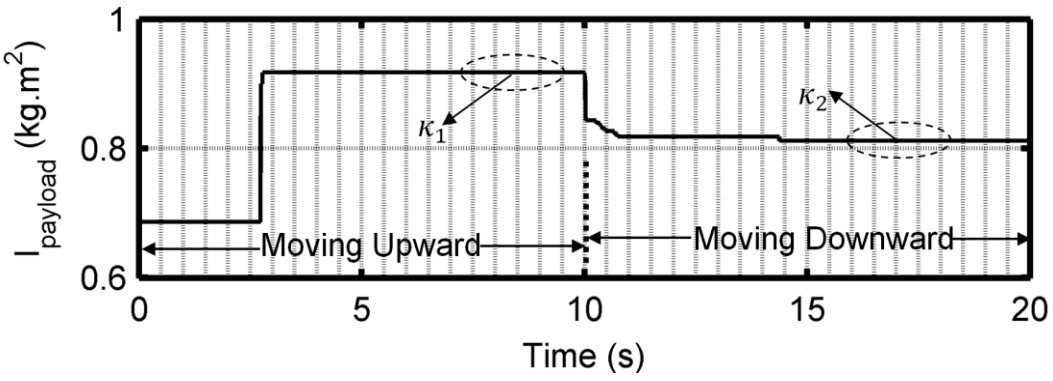

Figure 2.9 Offline payload estimation algorithm output during a sample experiment. This figure shows how the values of κ_1 and κ_2 are found during an estimation experiment.

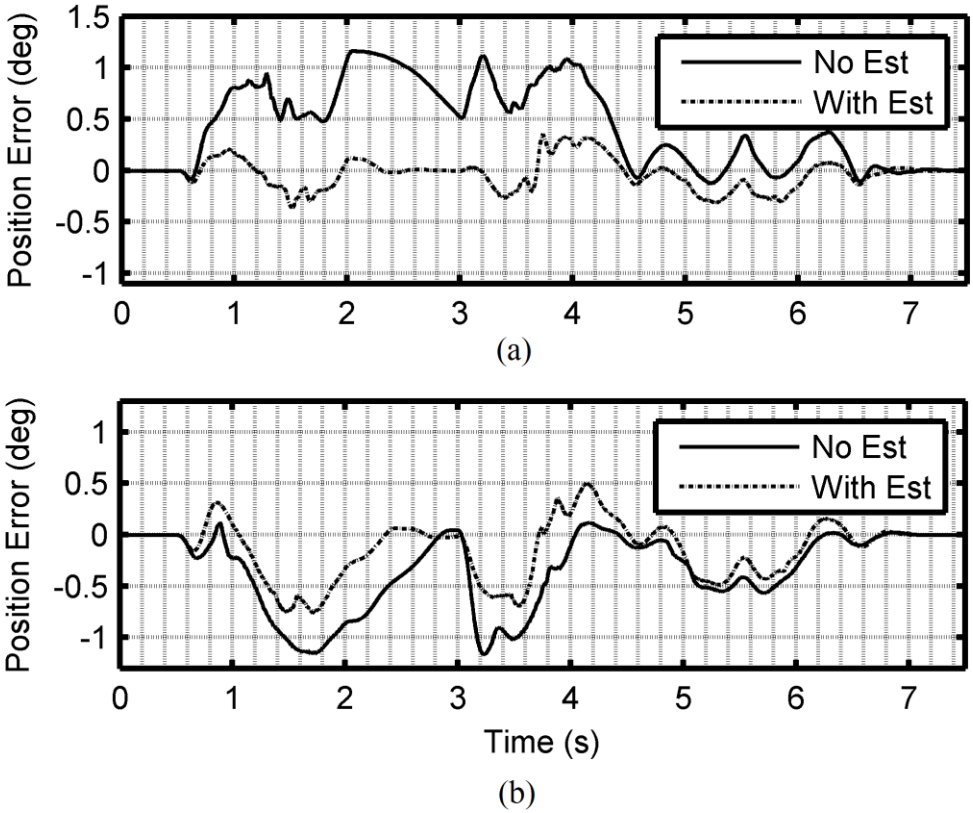

Figure 2.10 Tracking error for unknown payload experiments with and without using the payload estimator algorithm beforehand for: (a) lower-than-nominal payload, and (b) higher-than-nominal payload.

Table 2.1 Unknown payload tests results

Payload	*Estimator Status*	*RMSE (deg)*	*MaxAE (deg)*
Nominal	Off	0.169	0.494
Light	Off	0.457	1.218
(-53.0%)	On	0.116	0.394
Heavy	Off	0.397	1.176
(+34.7%)	On	0.203	0.790

2.6 Comparison with Prior Research Results

It is useful to compare the included results with the published results from existing position controlled rotary pneumatic actuators. The hardware used in this paper is very similar to that used in [12]. For trajectories similar to the one in Figure 2.7, the pressure MaxAE was 28 kPa (see p. 146 in [15]) with their pressure controller, while it was less than 8.5 kPa with the proposed controller. The improved pressure controller enabled improved position tracking. In [12], a 50% undershoot was observed with a 0.2° move experiment. Here a 0.045° move with no overshoot or undershoot was achieved. For the same cycloidal trajectory as in [12], the position RMSE with our actuator was 0.064° (i.e., 33% smaller). The actuator in [2] is 2nd closest actuator in the literature, although it is much more powerful, i.e., 81.3 Nm vs. 36.6 Nm. In [2] the MaxAE for a 100° move with a similar profile to the 90° cycloidal move in 2.5.4 was about 4° and the SSE was about 2° based on their plots. The values achieved with our actuator were 0.5° and ≤0.0045°, respectively. The other systems in [3][8][10]-[14] are too different for direct comparisons to be made.

2.7 Conclusion

The modelling, controller design and experimental verification of a high accuracy position controlled rotary pneumatic actuator were presented. The angular position is measured by an encoder directly coupled to the output shaft. Low-cost valves and pressure sensors were employed. The novel inverse valve model enabled the development of a faster and more precise model-based inner-loop pressure control law. The outer-loop position control law achieved small tracking errors using model-based terms plus position and velocity feedback. Mainly due to the adaptive friction compensator, the SSE was less than or equal to the encoder's resolution. Robustness to unknown payloads was achieved using an improved offline payload estimator. The experimental results are superior to those reported in the prior literature.

References

[1] R. B. van Varseveld and G. M. Bone, “Accurate position control of a pneumatic actuator using on/off solenoid valves,” *IEEE/ASME Transactions on Mechatronics*, vol. 2, no. 3, pp. 195-204, 1997.

[2] J. Bobrow and B. McDonell, “Modeling, identification, and control of a pneumatically actuated, force controllable robot,” *IEEE Transactions on Robotics and Automation*, vol. 14, no. 5, pp. 732-742, 1998.

[3] S. R. Pandian, Y. Hayakawa, F. Takemura and S. Kawamura, "Control performance of an air motor - can air motors replace electric motors?", in *Proc. IEEE International Conference on Robotics and Automation*, 1999, pp. 518-524.

[4] X. Shen, J. Zhang, E. J. Barth and M. Goldfarb, "Nonlinear model-based control of pulse width modulated pneumatic servo systems", *ASME Journal of Dynamic Systems, Measurement, and Control*, vol. 128, no. 3, pp. 663-669, 2006.

[5] J. F. Carneiro and F. G. Almeida, “Modeling Pneumatic Servovalves Using Neural Networks,” in *Proc. IEEE Conference on Computer Aided Control Systems Design*, Munich, Germany, 2006, pp. 790–795.

[6] T. Nguyen, J. Leavitt, F. Jabbari and J. E. Bobrow, "Accurate sliding-mode control of pneumatic systems using low-cost solenoid valves", *IEEE/ASME Transactions on Mechatronics*, vol. 12, no. 2, pp. 216-219, 2007.

[7] Z. Rao and G. M. Bone, “Nonlinear modeling and control of servo pneumatic actuators,” *IEEE Transactions on Control System Technology*, vol. 16, pp. 562-569, 2008.

[8] G. M. Bone and X. Chen, “Position control of hybrid pneumatic-electric actuators,” in *Proc. American Control Conf.*, 2012, pp. 1793-1799.

[9] S. Hodgson, M. Tavakoli, M. T. Pham and A. Leleve, "Nonlinear discontinuous dynamics averaging and PWM-based sliding mode control of solenoid-valve pneumatic actuators", *IEEE/ASME Transactions on Mechatronics*, vol. 20, no. 2, pp. 876-888, 2015.

[10] R. Rahman, L. He and N. Sepehri, "Design and experimental study of a dynamical adaptive backstepping-sliding mode control scheme for position tracking and regulating of a low-cost pneumatic cylinder", *International Journal of Robust and Nonlinear Control*, vol. 26, no. 4, pp. 853-875, 2015.

[11] G. M. Bone, M. T. Xue and J. Flett, "Position control of hybrid pneumatic–electric actuators using discrete-valued model-predictive control", *Mechatronics*, vol. 25, pp. 1-10, 2015.

[12] G. Ashby and G. M. Bone, "Improved hybrid pneumatic-electric actuator for robot arms", in *Proc. IEEE International Conference on Advanced Intelligent Mechatronics*, 2016, pp. 100-106.

[13] W. Tuvayanond and M. Parnichkun, "Position control of a pneumatic surgical robot using PSO based 2-DOF H_∞ loop shaping structured controller," *Mechatronics*, vol. 43, pp. 40-55, 2017.

[14] Y. Chen, I. S. Godage, Z. T. H. Tse, R. J. Webster and E. J. Barth, "Characterization and Control of a Pneumatic Motor for MR-Conditional Robotic Applications," *IEEE/ASME Transactions on Mechatronics*, vol. 22, no. 6, pp. 2780-2789, 2017.

[15] G. Ashby, "Design and validation of an improved hybrid pneumatic-electric actuator," M.A.Sc. thesis, Mech. Eng. Dept., McMaster University, Hamilton, Ontario, Canada, 2015.

Chapter 3. Design, Implementation and Control of an Improved Hybrid Pneumatic-Electric Actuator for Robot Arms

Abstract

Actuators used in robot arms need to be powerful, precise and safe. We present the design, implementation and control of a novel rotary hybrid pneumatic-electric actuator (HPEA) for use in robot arms, and collaborative robots in particular (also known as "cobots"). This HPEA is capable of producing torque 3.5 times larger than existing HPEA designs, while maintaining low mechanical impedance (due to low values of friction and inertia) and inherent safety. The HPEA prototype has 450 times less inertia and 15 times less static friction in comparison to a conventional robot actuator with similar maximum continuous output torque. The HPEA combines the large slow torque generated by four pneumatic cylinders, connected to the output shaft via rack and pinion gears, with the small fast torque generated by a small DC motor directly connected to the output shaft. The direct connection of the motor avoids the higher cost and lower precision caused by a gearbox or harmonic drive. The control system consists of an outer position control loop and two inner pressure control loops. High precision position tracking control is achieved due to the combination of a model-based pressure controller, model-based position controller, adaptive friction compensator and offline payload estimator. Experiments were performed with the actuator prototype rotating a link and payload in the vertical plane. Averaged over five tests, a root-mean-square error of 0.024° and a steady-state error (SSE) of 0.0045° were achieved for a fast multi-cycloidal trajectory. This SSE is almost ten times smaller than the best value reported for previous HPEAs. An offline payload estimation algorithm is used to improve the control system's robustness. Finally, the superior safety of the HPEA is shown by modeling and simulating a constrained head-robot impact, and comparing the result with similar electric and pneumatic actuators.

INDEX TERMS Collaborative robots, hybrid pneumatic-electric actuator, impact modeling, pneumatic actuators, position control, robot control.

3.1 Introduction

Robot arms need actuators with high continuous torque capacity and high precision. Electric motors are commonly used for driving robot joints as they are easy to control, and can achieve a fast and accurate response. Due to their relatively low torque-to-mass ratio, electric motors need to be coupled with high-ratio transmissions such as gearboxes or harmonic drives (typically with ratios of 100:1 or larger). Using a high-ratio transmission causes the actuator's mechanical impedance to increase. This increase in impedance can then increase impact forces to dangerous levels. These impact forces are of particular concern with robots working in close proximity to humans (known as collaborative robotics), where high impact collisions may result in injury. Furthermore, for high impedance actuators to achieve precise force control either expensive joint torque or tool force sensors are required.

The high impedance of the actuator is caused by two main sources. First, the moment of inertia at the gearbox output is equal to the motor's inertia multiplied by the transmission ratio squared. With such large transmission ratios, even with small motor inertia, the moment of inertia at the output shaft becomes quite large. Secondly, the actuator's friction torque is calculated by taking the friction torque of the motor multiplied by the transmission ratio and then adding the friction torque introduced by the transmission drive. Again, when large transmission ratios are used even small torques are significantly amplified. Another disadvantage of electric motors is their tendency to overheat when providing large continuous torques, a common requirement during tasks where the robot arm is carrying a heavy payload. Compared to electric motors, pneumatic actuators are more cost effective, able to produce better power to weight ratios, avoid overheating and have naturally low impedance due to the inherent compliance of air. However, pneumatic actuators are unable to obtain the same level of fast and precise control that is possible with traditional electric motors.

A hybrid pneumatic-electric actuator (HPEA) can combine the advantages of both electric and pneumatic actuators, while mitigating their disadvantages. With a HPEA, the electric

and pneumatic actuators may be connected in series or in parallel. Both series and parallel configurations produce lower impedance than the conventional motor plus high-ratio transmission electric actuator. Connecting them in series increases the speed and position control precision compared to a pneumatic actuator, but does not increase the power output. Connecting them in parallel improves the output power and power to weight ratio compared with an electric actuator; and the speed and position control precision compared to a pneumatic actuator. Furthermore, the large torque provided by the pneumatic actuator allows a low transmission ratio (or even no transmission) to be used with the motor, allowing the actuator's mechanical impedance to remain low. For these reasons, only parallel-connected HPEA will be considered in this paper. A HPEA is an embodiment of the DM^2 actuation approach proposed in [1]. In [1], the DM^2 advantages relative to series-elastic actuation (e.g., used by Baxter robot from ReThink Robotics) and joint torque controlled actuation (e.g., used by the Kuka LBR iiwa robot) are also explained.

Many position control algorithms have been investigated for pneumatic actuators, including sliding-mode control (SMC) [2]-[5] and [28], adaptive control [6]-[8], iterative learning control [9], backstepping [10], PID [11], and feedback linearization [27]. However, unlike pneumatic actuators, very limited research has been conducted on HPEAs.

An early concept for a rotary actuator combining a pneumatic actuator and electric motor was proposed in a patent from 1987 [12]. This design was created to solve the aforementioned overheating problem and provide the desired low power to weight ratio for high payload applications. As this design was never actually produced, we consider the HPEA designs from [13]-[20] to be the most relevant.

In [13], a DC motor was connected in parallel with a rotary pneumatic motor using a pair of gears. This motor was used to drive a single-link robot through a second set of gears attached to the output shaft. The gear ratio between the pneumatic actuator and the output shaft was 30:1, and the 15:1 between the electric motor and the output shaft. The pneumatic torque was controlled using two servo valves, and two pressure sensors. The angle of the

output shaft was measured with an optical encoder. Two different control algorithms were studied. A sinusoidal position trajectory was tracked using a SMC strategy. This SMC strategy made use of a linearized model of the hybrid actuator. For point-to-point motion control, a mixture of the SMC strategy and a simple PD control was implemented. Experimental results for different horizontal motions were included for: step inputs, and a 200° peak-to-peak, 0.5 Hz, sine wave trajectory. In comparison to the pneumatic actuator with SMC control, the HPEA was able to reduce the settling time of the system from 1.2 s to 0.5 s for the step input, and reduce the maximum following error from 20° (10%) to less than 10° (5%) for the sine wave trajectory.

The HPEA prototypes described in [14][16][18] included one or two pneumatic muscle actuators (PMAs) connected by cable(s) to an output pulley, along with a DC motor connected to the output pulley by a gearbox. In [14] a 0.0305 m radius pulley was used with a gearbox with a 28:1 reduction ratio. The PMA pressure was controlled using a proportional valve and a simple PID controller. The angular position of the joint was controlled using acceleration feedforward plus PD controller. This work included experimental results for 12° peak-to-peak, 1 Hz and 3 Hz sine wave position trajectories. The experimental results showed that the HPEA reduced the maximum following error from approximately 50% to about 10%, compared with the PMAs operating alone. In [16] a single PMA was controlled using a model-based plus PI controller, while a feedforward torque controller was used to control the DC motor. Experimental results were presented for 190° step change and 30° peak-to-peak 2 Hz sinusoidal position trajectories. For the step change the steady-state error (SSE) was 3.4° (11%). For the sinusoidal trajectory the maximum tracking error was about 9° (30%). A two-stage optimal control strategy for a PMA plus DC motor was proposed in [18]. Their strategy first solved for the optimal motor and PMA inputs using a long term prediction horizon with a coarse time resolution. In the 2nd stage, the input for the motor was re-optimized using a shorter prediction horizon with a finer time resolution. Experimental results were presented for 1.2 rad peak-to-peak, 0.25 Hz and 1.0 Hz sinusoidal trajectories. For 1.0 Hz vertical motions with no payload, the root

mean square error (RMSE) values for the PMA alone and the HPEA were 0.24 rad and 0.075 rad, respectively.

A unique design for a linear HPEA was presented in [17]. Their design integrates a pneumatic cylinder and a linear electric motor into a very compact device. They controlled the forces produced by the cylinder and motor using separate PI controllers. The HPEA reduced the force RMSE to 1.77 N compared to the 6.26 N obtained using only the pneumatic cylinder. They did not control the HPEA's position or use it to drive a rotary joint.

The HPEA proposed in [15] and [19] generated most of its torque through a single pneumatic cylinder. This cylinder was used to both push and pull a rack gear that meshed with a pinion gear directly connected to the output shaft. The remainder of the torque was generated by a DC motor which drove the same pinion via a smaller gear (giving a 5:1 ratio). Instead of controlling the on/off solenoid valves with pulse-width modulation (PWM), the valves were switched on/off by a discrete-valued model predictive control algorithm. The electric motor was controlled using a form of inverse dynamics control. The authors of [19] reported improved position control results using these methods. In their experiments, the actuators rotated loads in the vertical plane from 0° to 90° following a cycloidal trajectory; where 90° corresponded to the maximum gravity load. With only the pneumatic actuator, the RMSE and SSE from these experiments were 0.64° and 0.23°, respectively, With the HPEA the RMSE and SSE were reduced to 0.11° and 0.04°, respectively.

This paper is an extended and improved version of our previous conference paper [20]. It also builds upon our pneumatic actuator controller from [27] and uses our electric-actuated robot impact model from [22].

The contributions of this paper are as follows:

1. A new HPEA design that produces higher torque than all previous designs, avoids the cost and lower precision caused by a gearbox (or harmonic drive).

2. Using model-based pressure control [27] with the HPEA rather than the PI control used in [20].
3. A high precision position controller has been developed that provides robustness to unknown payloads and friction uncertainty.
4. Robust stability analysis of the HPEA including the inner-loop pressure controllers and outer-loop position controller (not included in [20]).
5. Dynamic models for constrained impacts between a human's head and a robot arm are developed and simulated for electric, pneumatic and hybrid actuated robotic arms.
6. Experimental results demonstrating superior position tracking performance compared to [20], [27] and the best results from the literature.

In section 3.2, the design's advancements are compared to previous designs, and the implementation details of the prototype are described. This is followed by a quantitative comparison of the new HPEA to prior HPEAs, along with a conventional robot actuator in section 3.3. The system model and control algorithm are then presented in sections 3.4 and 3.5, respectively. The payload estimator is described in section 3.6. The human-robot impact models and simulation results are given in section 3.7. Finally, experimental results and conclusions are presented in sections 3.8 and 3.9, respectively.

3.2 Mechatronic Design and Implementation of the Hybrid Pneumatic-Electric Actuator

The new HPEA design introduces several advancements over previous HPEA design approaches. First, the electric motor is directly attached to the output shaft rather than being connected via gears as in [13]-[16][18][19]. By eliminating these gears, the associated friction and backlash from the gears are also eliminated. Furthermore, by directly coupling the motor to the output shaft, the amplification of mechanical impedance caused by a gearbox (as discussed in section I) is also avoided.

Second, we are able to directly measure the output shaft's angle, instead of inferring it from the piston position, or from a geared encoder as was done in [15][19]. By directly

measuring the angle we are able to obtain more precise position control. This stems from the fact that all errors caused by the gears between the sensor and output shaft have been eliminated.

Third, the power generated by the pneumatic actuator is transmitted with a pair of rack gears that are meshed with a single pinion coupled to the output shaft. This approach allows the extension and retraction forces from the pneumatic actuator to be used, rather than only the retraction forces, as is the case with a belt-pulley or cable-pulley transmission [14][16][18]. This however comes with the tradeoff that it is less compact than those previous designs. In the proposed design, the rack gears are located above and below the pinion, reducing the loading on the output shaft and its support bearings, compared with the single rack design utilized in [15][19].

Fourth, low friction pneumatic cylinders were chosen over rotary pneumatic motors [13] or PMAs [14][16][18]. Rotary pneumatic motors suffer from large friction torques caused by their seals, while PMAs suffer from friction induced hysteresis and a displacement dependent output force [23]. By using low friction pneumatic cylinders, both disadvantages were avoided; making precise position control easier and reducing the energy lost to friction.

The design details of the HPEA assembly can be seen in Figure 3.1. As the drawing shows, the actuator has a top and bottom rack gear, each controlled with a pair of pneumatic cylinders on the corresponding top and bottom. These cylinders are located to the left and right of each of the rack gears. This configuration allows a compact arrangement, since the racks are able to travel in between the pairs of cylinders. Furthermore, the arrangement applies zero net moment to the racks when the cylinder pairs push or pull together.

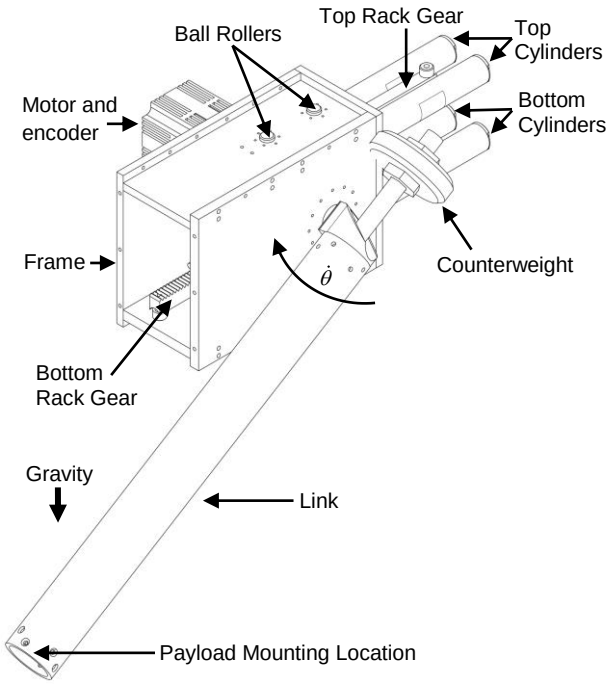

Figure 3.1 Assembly drawing of the rotary hybrid actuator.

A novel approach is used to guide each of the rack gears. First, a semicircular groove was machined into the back of each gear. Second, a pair of ball rollers are located such that their balls roll in each groove. This allows the minimum constraint for proper meshing to occur, without binding the assembly. Furthermore, the preload force at each of the ball rollers can be adjusted, to allow the backlash between the rack and pinion gears to be tuned and minimized. As can also be seen in the figure, the pinion gear is mounted on the output shaft. This output shaft can be connected to a rigid robot link to provide rotational motion. A counterweight is also added to the output shaft to balance the torque due to gravity from the mass of the link. The link angle θ, is defined as zero when the link is pointing vertically downwards and positive in the clockwise direction.

The stroke of the cylinder, and the pitch ratio of the pinion are key HPEA design parameters. Both parameters influence the output torque, the range of rotary motion, and the size of the actuator. A larger cylinder stroke will increase the range of motion, but will also increase the actuator size. A larger pitch radius increases the output torque, but decreases the range of motion, as well as increasing the actuator size. In our design we

chose a design constraint of 180° as the minimum range of motion. This was chosen as it was considered enough motion for a either a shoulder or elbow joint in a robot. A value of 40 Nm was chosen as the target for the maximum continuous output torque. This value was selected to ensure the actuator was comparable to the rated continuous joint torque of a small industrial robot (e.g. Universal Robots UR3 [24] or CRS A465 [25]). These design specifications are achieved in our implementation using four low friction cylinders with a 27 mm bore and 152 mm stroke (SMC, model NCMB106); and a stainless-steel pinion with a 31.5 mm pitch radius.

The optimal ratio of maximum electric motor torque to maximum total HPEA torque is an open problem. The motor should generate enough torque to compensate for the deficiencies of the pneumatic actuator, but should still be small enough that it does not increase the HPEA size or mass significantly. The motor should also have a low inertia rotor to keep the HPEA's overall mechanical impedance low, but as stated before, this typically comes at the expense of reduced torque. For the proposed design, a small brushless DC motor was selected (Animatics, model SM3430D, in current control mode). This motor is capable of a peak torque of 3.25 Nm, a continuous torque of 1.09 Nm, and has a 1.34×10^{-4} kgm^2 rotor inertia. The angle of the output shaft is obtained with a high-resolution encoder mounted on the motor's rear shaft (Quantum Devices, model QR12-20000, giving 8×10^4 counts/rev using quadrature counting). Since the motor is directly coupled to the output shaft, the resolution of the position measurement is 0.0045°.

Figure 3.2 presents a schematic diagram for the pneumatic, electrical and mechanical components of the HPEA. Based on the assembly of the racks and cylinders, the top cylinders' chambers containing rods and the bottom cylinders' chambers without rods, work together to form what we term "Chamber Group 1" (CG1). Similarly, "Chamber Group 2" (CG2), is made up of the top cylinders' chambers without rods and the bottom cylinders' chambers containing rods (i.e. the opposite of CG1).

The area of both chamber groups is equal to four times the bore's cross-sectional area, minus two times the rod's cross-sectional area. Furthermore, CG1 drives the output shaft

in the positive direction when its pressure is greater than CG2, with CG2 driving the shaft in reverse when the opposite is true.

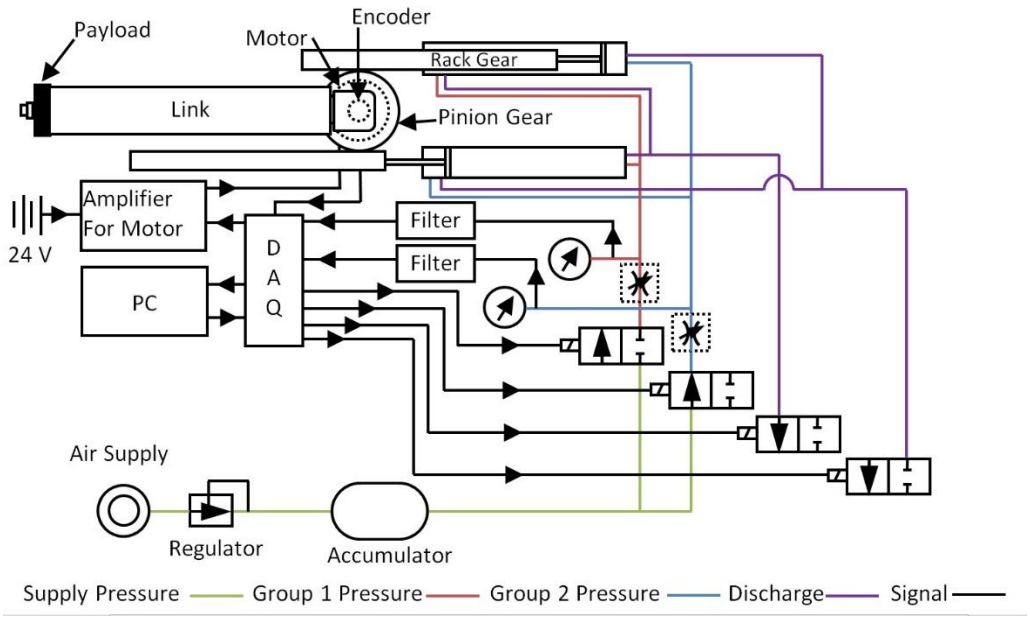

Figure 3.2 Schematic diagram of the pneumatic, electrical and mechanical components of the hybrid actuator.

Simple on/off solenoid valves were chosen, as they are considerably less expensive than proportional/servo valves ($40 USD vs. $800 USD). PWM was utilized to approximate the flow behavior of a proportional/servo valve, as was done in [3][5][11]. To allow each CG's pressure to be controlled independently two high speed 2/2 solenoid valves (FESTO MHJ10) are connected to each CG, i.e. one valve is used for charging and other for discharging the CG. To attenuate high frequency noise, the pressure sensor outputs (SSI Model P51-100) were passed through low pass filters with a 95 Hz cut off frequency. The pressure and position measurements are obtained using a National Instruments (NI) data acquisition system (DAQ). The DAQ (NI, models PCIe-6353 and PCI-6602) samples the sensors at 1 kHz and outputs the PWM signals to the valve drivers. The control algorithms are implemented in C language on a PC containing an Intel Core i5 2400 (3.1 GHz) processor. A photograph of the finished prototype is shown in Figure 3.3.

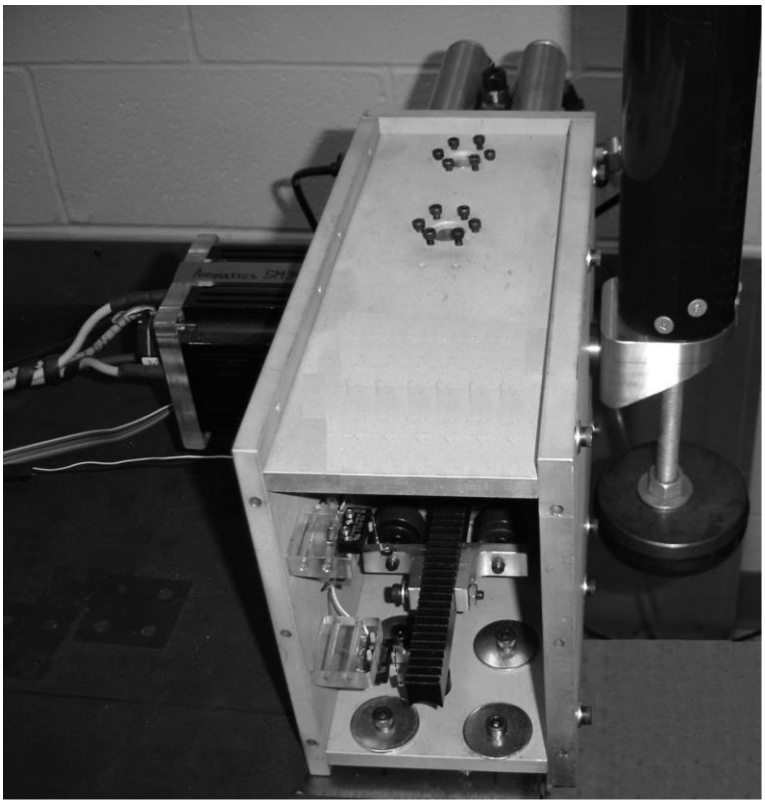

Figure 3.3 Photograph of the hybrid actuator with the link at θ=180º.

3.3 Comparison of New HPEA to Prior HPEAs and a Conventional Robot Actuator

The specifications of the new HPEA design were compared to those for previous HPEAs and for a conventional robot actuator. The results are listed in Table 3.1. The ratios of motor torque to total torque were calculated using the maximum continuous torque values. Also note that several of the specifications are underestimated as explained in the table's footnotes.

Table 3.1 Comparison of HPEA and DC motor plus Harmonic Drive actuator specifications

Spec.	Robot Actuator				
	HPEA from [13]	***HPEA from [14]***	***HPEA from [15][19]***	***New HPEA***	***DC motor + HDT [a] [25][26]***
Max. cont. torque (Nm)	10.9	7.1	10.0[b]	37.7[b]	39.5
Ratio of motor torque to total torque (%)	14	14	10	3	100
Static friction torque at output shaft (Nm)	> 9.7[c]	n/a [d]	0.1	0.23	>3.4[e]
Moment of inertia at output shaft (kgm^2)	$>1.5\times10^{-3}$ [f]	$>9.1\times10^{-4}$ [g]	6.4×10^{-5}	2.0×10^{-3}	0.90

a. Used for CRS A465 robot arm joints 1 and 3.

b. For 700 kPa absolute supply pressure.

c. Due to a lack of information in [13] this value does not include the friction torques from the DC motor, gears and bearings.

d. The information in [14] was insufficient to estimate the static friction torque.

e. This value does not include the unknown friction torques from the harmonic drive and the joint's bearings.

f. Due to a lack of information in [13] this value only includes the inertia of the DC motor.

g. Due to a lack of information in [14] this value only includes the inertia of the DC motor.

Based on the Table 3.1 data, the new HPEA design is capable of producing 3.5 more times continuous torque and is subject to 40 times less friction in comparison to the HPEA design in [13]. The new design also produces 5.4 times more torque than the design from [14]. The closest competitor is the HPEA from [15][19], with the new design producing 3.77 times more torque. However, the new design does suffer from 2.3 times more friction, and 31 times higher inertia in comparison to the design in [15][19].

The new HPEA design is also able to achieve significantly more precise movement compared to previous designs. These findings are detailed in section VIII. Lastly, the new HPEA design is able to achieve this with a ratio of motor torque to total torque of only 3%.

This value is significantly smaller than previous HPEA designs. As discussed in section 3.2, the motor torque is only required to compensate for the short comings in the response time and precision of the pneumatic actuator. We chose a smaller motor under the assumption that torque from the pneumatic cylinders could be accurately controlled; thereby the electric motor would only be required to minor torque contributions. This assumption is validated by the experimental results presented in section 3.8.

The most common actuator used by industrial robots is a DC motor connected to a harmonic drive transmission (HDT). To present a reasonable comparison, the proposed HPEA design is compared to a DC motor with a 100:1 HDT whose continuous rated torque is similar to the new HPEA. This motor plus HDT are used in joints 1 and 3 of the CRS A465 robot. This actuator was also chosen since its inertia and friction values can be estimated from the specifications of its CMC model 3515 motor [25][26]. While the specifications of the actuators show that their torques are similar, the DC motor plus HDT have a moment of inertia that is 450 times larger than the proposed HPEA design. Furthermore, the static friction of the DC motor plus HDT is 15 times greater than that of the HPEA actuator. Given the significantly lower inertia, and lower static friction, we can conclude that the new HPEA design has much lower mechanical impedance than the conventional actuators used in robot arms. This lower impedance will lead to smaller collision forces when human-robot impacts occur. This safety issue will be investigated in section 3.7.

3.4 System Modeling

In this section we will introduce the system model that will be used to control the HPEA actuator. The system is comprised of two solenoid valves, four pneumatic cylinders, rack and pinion gears, an amplifier, a DC motor, a counterweight, rigid link and a payload mass. The rotational dynamics are defined by:

$$I_{total}\ddot{\theta} = \tau_m + \tau_p - \tau_g - \tau_f \tag{3.1}$$

where I_{total} is the total moment of inertia; $\ddot{\theta}$ is the angular acceleration of the output shaft; τ_p is the torque produced by the pneumatic cylinders; τ_m is torque output of the motor; τ_g is torque due to gravity acting on the payload, link and counterweight; and τ_f is the friction torque. Note that I_{total} is the total moment of inertia including the payload mass, link, counterweight, pinion gear, rack gears, and various minor components. Recalling the CGs defined in section 3.2, the pneumatic torque is given by:

$$\tau_p = r_p A_g \left(P_1 - P_2 \right) \tag{3.2}$$

where r_p is the pinion gear's pitch radius; $A_g = 4A_p - 2A_r$ is the total cross-sectional area of each CG; A_p and A_r are the cross-sectional areas of the each cylinder's piston and rod, respectively; P_1 and P_2 are the pressures inside CG1 and CG2, respectively. Employing the ideal gas law, conservation of mass, and conservation of energy for each CG, the pressure dynamic equation for each chamber group is:

$$V_j \dot{P}_j + kP_j \dot{V}_j = \dot{m}_j kRT \quad j \in \{1, 2\} \tag{3.3}$$

where $\dot{m}_j$ is the overall mass flow rate into the j^{th} CG, k is the ratio of specific heats for air (1.4), R is the universal gas constant (287 $\text{Pa}\cdot\text{m}^3\cdot\text{K}^{-1}$), T is the air temperature, V_j is the CG volume, and P_j is the CG pressure. The time derivative of mass flow rate can be derived from (3.3) as:

$$\ddot{m}_j = \left(\text{k} P_j \ddot{V}_j + \ddot{P}_j V_j + (1+\text{k}) \dot{P}_j \dot{V}_j \right) \Big/ \text{k} \text{R} T \quad j \in \{1, 2\} \tag{3.4}$$

The mass flow rate into each CG is dependent on the flow through the PWM driven supply and the discharge valves. Assuming the supply pressure (P_s) and atmospheric pressure (P_0) remain constant, the relationships between the mass flow rates into the CGs and the valve inputs are defined by (3.5).

$$\dot{m}_j = f_j(u_j, P_j) \quad j \in \{1, 2\} \tag{3.5}$$

In (3.5), u_j is the PWM duty cycle for the supply valve of the associated CG. The duty cycle for the discharge valve of each CG is simply defined as: $1-u_j$. The functions f_1 and f_2 depend on the valve's internal geometry and are highly nonlinear. Combining (3.3) and (3.5), the pressure derivative model for each CG in (3.6) is obtained.

$$\dot{P}_j = \left(f_j\left(u_j, P_j\right) \mathrm{kR}T - \mathrm{k}P_j\dot{V}_j \right) \Big/ V_j \quad j \in \{1, 2\} \tag{3.6}$$

where:

$$\begin{cases} V_1 = V_{01} + A_g r_p \theta \\ V_2 = V_{02} - A_g r_p \theta \end{cases} \tag{3.7}$$

In (3.7), V_{01} and V_{02} are the CG1 and CG2 volumes at $\theta = 0$, respectively.

Since finding an accurate friction model is very difficult, if not impossible, a simple model is considered for the friction torque which will form the basis of implementing the adaptive friction compensator. This will be described in section 3.5. Equation (3.8) shows the simple friction model.

$$\tau_{\mathrm{f}} = \begin{cases} \tau_{\mathrm{f}}^{+} & \dot{\theta} > 0 \\ 0 & \dot{\theta} = 0 \\ \tau_{\mathrm{f}}^{-} & \dot{\theta} < 0 \end{cases} \tag{3.8}$$

The motor dynamics are much simpler than the dynamics of the pneumatic actuator. The torque from the electric motor can be modelled as:

$$\tau_m = f_m\left(u_m\right) \tag{3.9}$$

where u_m is the command signal sent to the amplifier, and $f_m(\cdot)$ is a nonlinear function. This function can be identified by calibration tests.

As mentioned in Section 3.2, the counterweight balances the gravity torque acting on the link. Thus the remaining gravity torque is:

$$\tau_g = d_p m_p g \sin(\theta) \tag{3.10}$$

where m_p is the mass of the payload attached to the end of the link, and d_p is the distance from the axis of rotation to the payload's center of mass. To draw a comparison between the rotary HPEA and a linear actuator, the mass equivalent to I_{total} can be calculated with:

$$m_{eq} = \frac{F}{\ddot{y}_b} = \frac{\tau / r_p}{r_p \ddot{\theta}} = \frac{I_{total} \ddot{\theta} / r_p}{r_p \ddot{\theta}} = \frac{I_{total}}{r_p^2} \tag{3.11}$$

3.5 Controller Design

The control system manipulates the duty cycles of the valves and the motor current to control the motion of the arm. The system requires four controllers to be designed: two inner-loop pressure controllers for CG1 and CG2; and two position controllers for the pneumatic actuator and the electric motor that form the outer-loop. Figure 3.4 shows the structure of the overall control system.

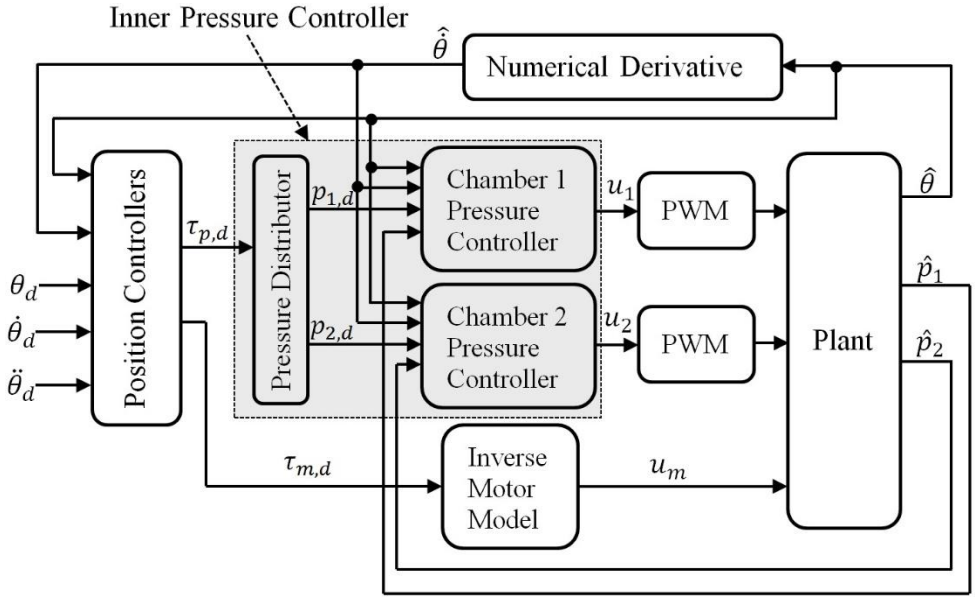

Figure 3.4 Overall control system structure

3.5.1 Model-Based Position Controller for the Pneumatic Actuator

For position control of the pneumatic actuator we employed our model-based control law from [27]. It will be briefly summarized in this section. The control law includes feedforward terms based on (1), (2), (8) and (10). These feedforward terms provide a rapid response, while the feedback terms provide robustness. The desired torque from the pneumatic actuator is then:

$$\tau_{p,d}(t_i) = \hat{I}_{total}\ddot{\theta}_d(t_i) + \hat{\tau}_g(t_i) + \tau_f^{\,*}(t_i) - K_P\hat{e}_\theta - K_D\hat{\dot{e}}_\theta \qquad (3.12)$$

where $t_i = iT_s, i \in \mathbf{Z}^+$ is the time of the current sample; $\hat{I}_{total}\ddot{\theta}_d(t_i)$, $\hat{\tau}_g(t_i)$ and $\tau_f^{\,*}(t_i)$ are the inertia, gravity and adaptive friction compensation terms, respectively; $\hat{e}_\theta = \hat{\theta}(t_i) - \theta_d\ (t_i)$ is the position error, $\hat{\dot{e}}_\theta = \hat{\dot{\theta}}(t_i) - \dot{\theta}_d(t_i)$ is the velocity error, $\hat{\theta}(t_i)$ is the sensed position; $\hat{\dot{\theta}}(t_i)$ is the estimated velocity; K_P is the positive proportional gain, K_D is the positive derivative gain, and the symbol " ˆ " denotes the measured or estimated value for the variable. $\hat{\dot{\theta}}(t_i)$ is estimated by backward differencing and low-pass filtering the sensed position. The adaptive friction compensator is defined by (3.13). In this equation, $\tau_f^{\,+}$, are the values from the friction model shown in (8); and λ^+ and λ^- are the adaptation increments. Also $\tau^*_{f,min}$, and $\tau^*_{f,\max}$ are the lower and $\tau_f^{\,-}$ upper limits for the friction torque adaptation, respectively. When the desired velocity is zero, $\tau_f^{\,*}(t_i)$ is adjusted until the position error magnitude is less than the threshold δ. Note that in (13) $\dot{\theta}_d(t_i)$ is used instead of $\hat{\dot{\theta}}(t_i)$ to avoid the detrimental effects of a noisy velocity estimate, especially near $\dot{\theta} = 0$.

$$\tau_f^*(t_i) = \begin{cases} \tau_f^+ & \dot{\theta}_d(t_i) > 0 \\ \tau_f^- & \dot{\theta}_d(t_i) < 0 \\ \tau_f^*(t_{i-1}) - \lambda^+ & \dot{\theta}_d(t_i) = 0 \wedge \hat{e}_\theta(t_i) > \delta \wedge \\ & \tau_f^*(t_{i-1}) > \tau_{f,min}^* \\ \tau_f^*(t_{i-1}) + \lambda^- & \dot{\theta}_d(t_i) = 0 \wedge \hat{e}_\theta(t_i) < -\delta \wedge \\ & \tau_f^*(t_{i-1}) < \tau_{f,max}^* \\ \tau_f^*(t_{i-1}) & \text{Otherwise} \end{cases} \quad (3.13)$$

The desired chamber pressures are given by:

$$P_{1,\mathrm{d}}(\mathrm{t_i}) = \tfrac{1}{2}\left(P_0 + P_s + \Delta P_d(t_i)\right) \quad (3.14)$$

$$P_{2,d}(\mathrm{t_i}) = \tfrac{1}{2}\left(P_0 + P_s - \Delta P_d(\mathrm{t_i})\right) \quad (3.15)$$

$$\Delta P_d(t_i) = \tau_{p,d}(t_i) \Big/ \left(A_g r_p\right) \quad (3.16)$$

Equations (3.14)-(3.16) are designed to keep the CG pressures well above atmospheric since we have observed that the resulting higher air density improves the position tracking performance.

3.5.2 Position Controller for the Electric Actuator

The electric motor improves the powerful but relatively slow pneumatically generated torque by adding smaller, high-frequency torques according to its position control law. A standard PD controller is effective for this application due to the simple dynamics of the electric motor. The control law is given by (3.17). Recalling (3.9), here an inverse motor calibration is performed to find function $f'_m(.)$ needed to calculate the motor input, u_m, as shown by equation (3.18).

$$\tau_{m,d}(t_i) = -K_{P,m}\hat{e}_\theta - K_{D,m}\dot{\hat{e}}_\theta \quad (3.17)$$

$$u_m = f'_m\left(\tau_{m,d}\right) \tag{3.18}$$

3.5.3 Inverse Valve Models

Inverse valve models are required to implement the model-based pressure controller. Typically this involves fitting a forward valve model, that is either linear or quadratic in *u*, and then solving it for the unknown *u* using the known values: desired mass flow rate, measured chamber pressure, volume and volume time derivatives [3][6][10]. Inverse valve models have also been developed, e.g. using neural networks [21].

To avoid over simplifying the forward model to make it invertible, and also avoid the training difficulties (e.g., data hungry, local minima and overfitting) associated with neural networks, we employ the approach presented in [27]. With this approach the inverse behavior of each valve is modelled by a polynomial in three variables as follows:

$$\begin{cases} u_1(t_i) = f_{1inv}\left(\hat{\dot{m}}_{1d}(t_i), \hat{\ddot{m}}_{1d}(t_i), \hat{P}_1(t_i)\right) \\ u_2(t_i) = f_{2inv}\left(\hat{\dot{m}}_{2d}(t_i), \hat{\ddot{m}}_{2d}(t_i), \hat{P}_2(t_i)\right) \end{cases} \tag{3.19}$$

$$\begin{cases} f_{1inv} = \sum_{\alpha=0}^{A}\sum_{\beta=0}^{B}\sum_{\gamma=0}^{G} C_{\alpha,\beta,\gamma}\, \hat{\ddot{m}}_{1d}(t_i)^{\alpha}\, \hat{\dot{m}}_{1d}(t_i)^{\beta}\, \hat{P}_1(t_i)^{\gamma} \\ f_{2inv} = \sum_{\alpha=0}^{A}\sum_{\beta=0}^{B}\sum_{\gamma=0}^{G} C_{\alpha,\beta,\gamma}\, \hat{\ddot{m}}_{2d}(t_i)^{\alpha}\, \hat{\dot{m}}_{2d}(t_i)^{\beta}\, \hat{P}_2(t_i)^{\gamma} \end{cases} \tag{3.20}$$

where $\hat{P}$ are the sensed pressures, $\hat{\dot{m}}_d$ are the desired mass flow rates and $\hat{\ddot{m}}_d$ are the desired mass flow rate time derivatives for the CGs. The inclusion of $\hat{\ddot{m}}_d$ in (3.20) was found to improve the fit of the model when rapid changes in $\dot{m}$ occurred. The optimal coefficients $C_{\alpha,\beta,\gamma}$ may be found by linear regression, avoiding the possibility of local minima.

3.5.4 Model-Based Pressure Controller

Each CG pressure will be controlled using the model-based control law we employed in [27]. Its equations are briefly summarized here, as follows:

$$\tilde{\dot{P}}(t_i) = \dot{P}_d(t_i) - K_P{}'\hat{e}_P(t_i) - K_I\hat{E}_P(t_i) \tag{3.21}$$

$$\hat{\dot{m}}_d(t_i) = \left(\mathrm{k}\hat{P}(t_i)\hat{\dot{V}}(t_i) + \tilde{\dot{P}}(t_i)\hat{V}(t_i)\right)\Big/\mathrm{kR}T \tag{3.22}$$

$$\hat{\ddot{m}}_d(t_i) = \left(\mathrm{k}\hat{P}(t_i)\hat{\ddot{V}}(t_i) + \ddot{P}_d(t_i)\hat{V}(t_i) + (1+\mathrm{k})\tilde{\dot{P}}(t_i)\hat{\dot{V}}(t_i)\right)\Big/\mathrm{kR}T \tag{3.23}$$

where $\hat{e}_P(t_i) = \hat{P}(t_i) - P_d(t_i)$ is the pressure error; $\hat{E}_P = \int_0^t \hat{e}_p dt$; $K_p{}'$ and K_I are positive proportional and integral gains, respectively. Note that $\hat{E}_P(t_i)$ is bounded to avoid integral windup. The valve duty cycles are calculated by substituting the values from (3.22) and (3.23), and the sensed pressures, into (3.19).

3.5.5 Analysis of Robust Stability

To prove the robust stability of the HPEA's position control system it is first necessary to prove the robust stability of the inner-loop pressure control subsystems. In [27] it was proven that the pressure control subsystems for a rotary pneumatic actuator are bounded-input bounded-output stable when the model uncertainties are bounded. Since the dynamics of those subsystems are unchanged with the HPEA, the proof in [27] applies to them as well.

With the outer-loop position control system, the addition of the motor's torque requires that the stability proof from [27] be extended for the HPEA. Defining $\Delta\tau_p = \tau_p - \tau_{p,d}$ as the pneumatic torque uncertainty, substitution into (2) gives:

$$\begin{aligned}\Delta\tau_p &= \left(P_1 - P_2\right)A_g r_p - \left(P_{1,d} - P_{2,d}\right)A_g r_p \\ &= \left(e_{p,1} - e_{p,2}\right)A_g r_p\end{aligned} \tag{3.24}$$

Equation (24) shows that $\Delta\tau_p$ is also bounded. Similarly for the electric actuator, electric torque uncertainty is defined as $\Delta\tau_m = \tau_m - \tau_{m,d}$. Substituting (3.9) and (3.18) into the definition of $\Delta\tau_m$ gives:

$$\Delta\tau_m = f_m\left(u_m\right) - \tau_{m,d} = f_m\left(f'_m\left(\tau_{m,d}\right)\right) - \tau_{m,d} \tag{3.25}$$

With proper motor calibration, the estimated functions f_m and f'_m will nearly cancel out each other so $\Delta\tau_m$ will be a small bounded value. Re-writing (3.12) gives:

$$\tau_p = \hat{I}_{total}\ddot{\theta}_d + \hat{\tau}_g + \tau_f^{\,*} - K_P(\hat{e}_\theta) - K_D(\hat{\dot{e}}_\theta) + \Delta\tau_p \tag{3.26}$$

The remaining bounded uncertainties are defined by $\Delta\theta = \hat{\theta} - \theta$, $\Delta\dot{\theta} = \hat{\dot{\theta}} - \dot{\theta}$, $\Delta I_{total} = \hat{I}_{total} - I_{total}$, $\Delta\tau_g = \hat{\tau}_g - \tau_g$, and $\Delta\tau_f = \tau_f^{\,*} - \tau_f$. Substituting τ_p from (3.1) into (3.26) gives:

$$\begin{aligned}&I_{total}\ddot{e}_\theta + K_D\dot{e}_\theta + K_p e_\theta = \\ &\quad \Delta\tau_p + \Delta I_{total}\ddot{\theta}_d + \Delta\tau_f + \Delta\tau_g + \tau_m - K_p\Delta\theta - K_D\Delta\dot{\theta}\end{aligned} \tag{3.27}$$

Now substituting from (3.17) into (3.27), gives (3.28) and (3.29).

$$I_{total}\ddot{e}_\theta + \left(K_D + K_{D,m}\right)\dot{e}_\theta + \left(K_P + K_{P,m}\right)e_\theta = \Delta U_2 \tag{3.28}$$

$$\begin{aligned}\Delta U_2 &= \Delta\tau_p + \Delta\tau_m + \Delta I_{total}\ddot{\theta}_d + \Delta\tau_f + \Delta\tau_g \\ &\quad -\left(K_P + K_{P,m}\right)\Delta\theta - \left(K_D + K_{D,m}\right)\Delta\dot{\theta}\end{aligned} \tag{3.29}$$

The total uncertainty ΔU_2 is made up of bounded terms so it is also bounded. Since $I_{total} > 0$, $K_D + K_{D,m} > 0$, and $K_P + K_{P,m} > 0$, (28) guarantees that e_θ converges inside

a bounded region when inputs θ_d , $\dot{\theta}_d$, and $\ddot{\theta}_d$ are bounded. So the HPEA's position control system is bounded-input bounded-output stable.

3.6 Offline Payload Estimation

Uncertainties in system dynamics are known to negatively affect the performance of model-based controllers. The proposed position controller uses the adaptive friction compensator (3.13) to address the uncertainty of friction. The other major source of uncertainty is caused by the arm carrying an unknown payload. The payload estimation algorithm from [27] will be used to improve the controller's performance with unknown payloads. The algorithm requires the parameters C_f , $S_{threshold}$ and $\tau_{\text{e,threshold}}$ to be manually tuned. Note that the payload estimation does not affect the stability of the closed-loop system since it is performed offline (i.e., prior to the position control).

3.7 Constrained Impact Modelling and Simulation

In this section, dynamic models are developed and used to simulate a constrained impact between a robot arm and a human's head. These models can be used to simulate and compare the safety of electric, pneumatic and hybrid actuators. Since head injuries are the most serious a constrained impact scenario, where the head is prevented from moving away from the robot, will be studied. In some of the prior robotics literature, the "Head Injury Criterion (HIC)" has been used to assess the injury risk of an impact with human head (e.g. [28]). This criterion is based on the magnitude of head acceleration after the impact. It cannot be used with constrained impact case studied here since the head doesn't move. Instead, the peak impact force is considered as the safety criterion as in the international standard [29].

Figure 3.5 illustrates the impact scenario. A dynamic impact model for this scenario assuming an impact occurring near the arm's tip, arm rotation in the horizontal plane, and an electrically actuated robot was presented in our prior work [22]. It also assumed that the deflection of the joint transmission and the bending of the links were negligible. In the modelling equations all displacements were relative to the head's position, x_h. The

displacements of the arm, compliant cover, skull and pneumatic actuator are termed x_r, x_c, x_s and x_p, respectively.

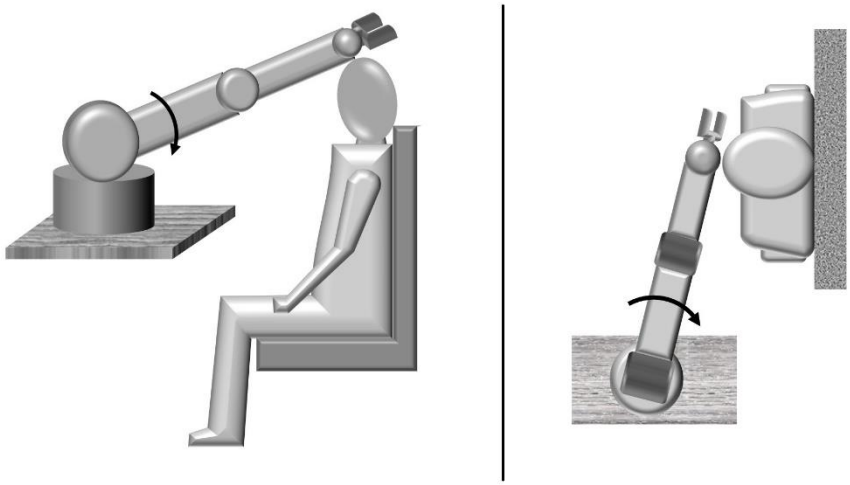

Figure 3.5 Illustrations of constrained head-robot impacts for a seated person (left) and standing person (right).

Two additional models are introduced in this paper to allow the simulation of robots employing pneumatic or hybrid actuators. As in [22], the impact dynamics in the normal direction are modelled by a linear one dimensional lumped parameter model. Figure 3.6 shows the new models below the original model developed for electric actuators. In the new model for the pneumatic actuator, air compliance is modeled as a linear spring acting between the piston position and joint position. The pneumatic model also includes a delay (not shown in the figure) since the pneumatic actuator's force changes relatively slowly. The hybrid impact model has both actuators acting in parallel. As in the original model [22] the electric actuator's delay is assumed to be negligible.

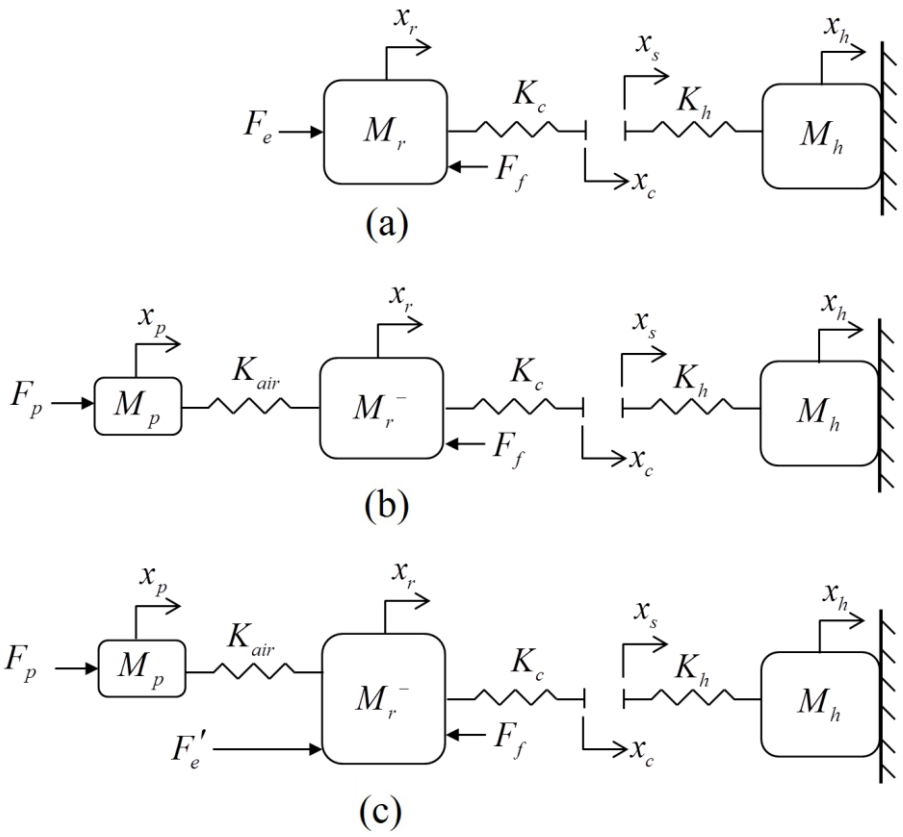

Figure 3.6 Impact model schematics for: (a) electric actuator [22], (b) pneumatic actuator and (c) hybrid pneumatic-electric actuator.

In these models, M_h, M_r and M_p are head mass, equivalent robot mass, and the equivalent mass of the pneumatic cylinders' pistons and rods, respectively. Also $M_r^- = M_r - M_p$ and K_h, K_c and K_{air} are the head equivalent stiffness, robot's compliant cover stiffness, and the equivalent air stiffness for the pneumatic actuator, respectively. F_e, F_p and F_f are the electric actuator force, pneumatic actuator force, and friction force in the robot joint, respectively. The robot's equivalent mass is calculated from the inertia of the actuator, $I_{actuator}$, and inertia of the link, I_{link}, using:

$$M_r = \left(I_{actuator} + I_{link}\right) / d_i^2 \tag{3.30}$$

where d_i is the distance from the impact point on the robot to the joint.

The friction force is modelled as the sum of dry and viscous friction components as follows:

$$F_f = \begin{cases} f_k \text{sign}(\dot{x}_r) + k_v \dot{x}_r & \text{if } \dot{x}_r \neq 0 \\ F_{cont} - F_i & \text{if } \dot{x}_r = 0 \wedge |F_{cont} - F_i| < f_s \\ f_s sign(F_{cont} - F_i) & \text{otherwise.} \end{cases} \tag{3.31}$$

where F_{cont} equals F_e, F_p or $F_e' + F_p$ for the electric, pneumatic and hybrid actuator, respectively; f_k is the kinetic friction force; f_s is the static friction force; and k_v is the coefficient of viscous friction.

Assuming a standard PD plus feedforward controller is used, the electric actuator's force is given by:

$$F_e = \hat{M}_r \ddot{x}_d - K_{P,e}(x_r - x_d) - K_{D,e}(\dot{x}_r - \dot{x}_d) \tag{3.32}$$

where $\hat{M}_r$ is the nominal value of M_r; x_r and x_d are actual and desired positions of the robot arm at the impact point, respectively; $K_{P,e}$ is the proportional gain; and $K_{D,e}$ is the derivative gain. The PD gains can be obtained from the desired closed-loop bandwidth, f_{bw}, and desired damping ratio, ζ, as follows:

$$\omega_n = 2\pi f_{bw} \Big/ \left(\zeta + \sqrt{1+\zeta^2}\right) \tag{3.33}$$

$$K_{P,e} = \hat{M}_r \omega_n^{\ 2} \tag{3.34}$$

$$K_{D,e} = 2\zeta \sqrt{K_{P,e} \hat{M}_r} \tag{3.35}$$

From (3.12) the desired pneumatic actuator force in the normal direction is:

$$F_{p,d} = \hat{M}_r \ddot{x}_d + \frac{\tau_f^*}{d_i} - K_{PL}(x_r - x_d) - K_{DL}(\dot{x}_r - \dot{x}_d) \tag{3.36}$$

where $K_{PL} = K_P / d_i^2$ and $K_{DL} = K_D / d_i^2$. The actual pneumatic actuator force is modelled as:

$$F_p(t) = F_{p,d}(t - t_d) \tag{3.37}$$

where t_d is the pneumatic actuator's delay.

With the hybrid actuator, the force from the electric motor is obtained from (3.17) as follows:

$$F_e' = -K_{PLM}(x_r - x_d) - K_{DLM}(\dot{x}_r - \dot{x}_d) \tag{3.38}$$

where $K_{PLM} = K_{P,m} / d_i^2$ and $K_{DLM} = K_{D,m} / d_i^2$.

For the electric actuator model (Figure 3.6-a) the robot's equation of motion is:

$$M_r \ddot{x}_r = F_e - F_f - F_i \tag{3.39}$$

Here F_i is the impact force applied to the head by the robot (and vice-versa) through the model's springs, defined by:

$$F_i = \begin{cases} K_{hc} x_r & x_r > 0 \\ 0 & x_r \le 0 \end{cases} \tag{3.40}$$

where:

$$K_{hc} = K_h K_c / (K_h + K_c) \tag{3.41}$$

For the pneumatic actuator (Figure 3.6-b), the robot's equation of motion (3.39) is replaced by (3.42) and (3.43).

$$M_r \ddot{x}_r = K_{\text{air}}(x_p - x_r) - F_f - F_i \tag{3.42}$$

$$M_p \ddot{x}_p = F_p - K_{air}(x_p - x_r) \tag{3.43}$$

When the hybrid actuator is used (Figure 3.6-c), (3.42) is replaced by:

$$M_r \ddot{x}_r = K_{air}(x_p - x_r) + F_e - F_f - F_i \tag{3.44}$$

Finally, the equivalent linear stiffness due to air compressibility must be calculated at the impact point. To do this we make the following assumptions:

1. Both chambers are assumed to be at the midpoint pressure $P_{mid} = \frac{1}{2}\left(P_0 + P_s\right)$ before the collision.
2. The arm's displacement during the impact is small enough to apply local linearization.

Change of volume in each chamber due to the displacement is:

$$dV = A_g r_p dx / d_i \tag{3.45}$$

where dx is the displacement at the impact point. The pressure in CG1 after the displacement, P_1', is then:

$$\begin{aligned} &P_{mid} V_1 = P_1'(V_1 + dV) \\ &\Rightarrow P_1' = \left(V_1 / (V_1 + dV)\right) P_{mid} \end{aligned} \tag{3.46}$$

Using the same approach:

$$P_2' = \left(V_2 / (V_2 - dV)\right) P_{mid} \tag{3.47}$$

The air stiffness equation is derived by dividing the pneumatic force equation by the equivalent linear displacement and linearizing the result. The following equations show the derivation.

$$\begin{aligned} K_{\text{air}} &= \left(P'_2 - P'_1\right) A_g / dx \\ &= P_{mid} A_g \left(V_2 / (V_2 - dV) - V_1 / (V_1 + dV)\right) / dx \\ &= P_{mid} A_g \left((V_1 + V_2) dV / \left(V_1 V_2 + (V_2 - V_1) dV - dV^2\right)\right) \end{aligned} \tag{3.48}$$

Linearizing (48) for $dV \approx 0$, substituting dV from (3.45) and simplifying gives:

$$\begin{aligned} K_{\text{air}} &= P_{mid} A_g \left(V_1 + V_2\right) dV \Big/ V_1 V_2 dx \\ &= P_{mid} A_g \left(V_1 + V_2\right)\left(A_g r_p dx \big/ d_i\right) \Big/ V_1 V_2 dx \\ &= P_{mid} {A_g}^2 r_p \left(V_1 + V_2\right) \Big/ d_i V_1 V_2 \end{aligned} \tag{3.49}$$

The impact models for the three actuators have been simulated using Verlet numerical integration. The simulation was programmed in Matlab. The simulations assume $\hat{M}_r = M_r$ and a zero payload. Table 3.2 shows the parameters used in the simulations. The controller gains in (3.32) were chosen such that the electric actuator has the same bandwidth as the electric component of the hybrid actuator, and $\zeta = 0.7$. The K_{air} value was calculated assuming the impact happens when $\theta = 90°$. Note that the value of M_h is irrelevant due to head being constrained in the simulations. The electric actuator parameters were obtained from the last column of Table 3.1. This actuator [25][26] is almost equivalent to the existing hybrid actuator in terms of maximum continuous output torque. The corresponding maximum controller force of 57 N was obtained by dividing the maximum torque by d_i. The parameters of the pneumatic and hybrid actuators were calculated from the tuned parameters used in the experiments, section 3.8.

Table 3.2 Impact simulation parameters

Parameter	Value	Description
d_i	0.7 m	Distance from the impact point on the robot to the joint
dt	0.01 ms	Solver time step
T_s	1 ms	Controller sampling period
K_c	25 kN/m	Compliant cover stiffness [30]
K_h	150 kN/m	Head stiffness [29]
Electric Actuator		
M_r	2.0 kg	Equivalent robot mass
f_k	4.9 N	Kinetic friction force
f_s	4.9 N	Static friction force
k_v	0.69 Ns/m	Coefficient of viscous friction
f_{bw}	19.4 Hz	Desired closed-loop bandwidth
$K_{P.e}$	7956.1 N/m	Position controller gain
$K_{D,e}$	175.5 Ns/m	Position controller gain
Pneumatic and Hybrid Actuators		
M_r	0.18 kg	Equivalent robot mass
M_p	0.052 kg	Equivalent mass of pistons and rods
K_{air}	490 N/m	Air stiffness
t_d	5 ms	Pneumatic actuator delay
f_k	0.33 N	Kinetic friction force
f_s	0.33 N	Static friction force
k_v	0.047 Ns/m	Coefficient of viscous friction
K_{PLM}	1428.6 N/m	Position controller gain for the electric component
K_{DLM}	10.2 Ns/m	Position controller gain for the electric component
K_{PL}	1020.4 N/m	Position controller gain for the pneumatic component
K_{DL}	12.2 Ns/m	Position controller gain for the pneumatic component

Figure 3.7 shows a comparison result for a robot moving at 0.25 m/s before impact. This speed is the maximum permitted by the international safety standard [31] when a human is within reach of a robot arm. The peak impact forces are 29.9 N, 41.2 N and 63.1 N for the hybrid, pneumatic and electric actuators, respectively. These results show the higher inherent safety of hybrid actuators. Although it has the same bandwidth as the electric component of the hybrid actuator, with the electric actuator the controller force increases fast and saturates. This contributes to the higher impact force caused by the electric actuator. The sudden large increase in the controller force doesn't occur with the hybrid actuator since the ratio of the electric force to the pneumatic force is small. With the x_r curves for the pneumatic and hybrid cases the arm moves back and loses contact after the first impact, due to their larger compliance. The arm driven by the electric motor does not lose contact and causes the relatively large skull deflection of 0.42 mm.

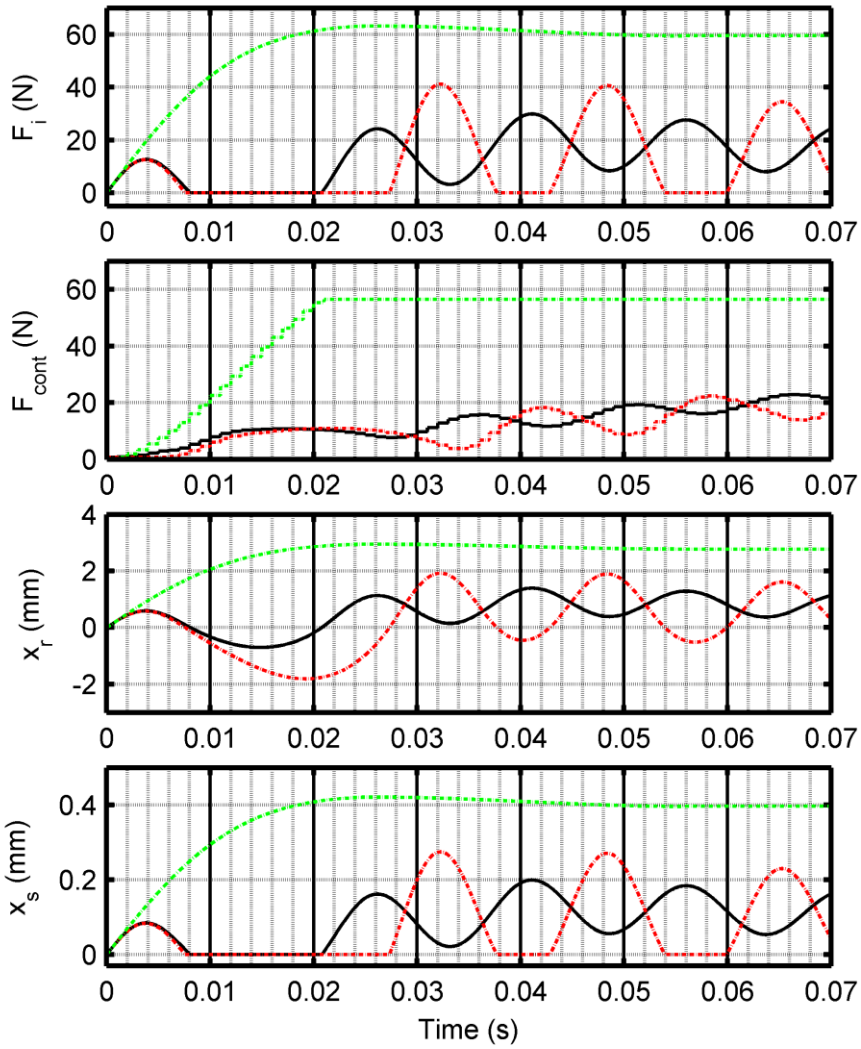

Figure 3.7 Impact simulation results for the three actuators, hybrid (black) pneumatic (red) and electric (green). A constrained head-robot impact has been modeled with the robot moving at a constant speed of 0.25 m/s before the impact. The actuators are almost equivalent in terms of maximum continuous output torque.

3.8 Experiments

For the experiments, a nominal payload mass (not visible in Figure 3.3) of 1.4 kg was attached to the end of the 0.7 m arm, making the nominal payload's moment of inertia equal to 0.69 kgm^2. The total rotational inertia is equivalent to a linear actuator translating a 573 kg mass. Tables 3.3 and 3.4 list the system parameters and the tuned controller parameters, respectively. The hardware details were presented in section 3.2.

Table 3.3 HPEA system parameters

Parameter	Value	Description
I_{total}	0.773 kgm^2	Total moment of inertia with nominal payload of 1.40 kg
r_p	0.0315 m	Pitch radius of the pinion gear
A_g	0.0022 m^2	Total cross-sectional area of each CG
V_{01}	1.50×10^{-4} m^3	CG1 volume at $\theta = 0$
V_{02}	3.65×10^{-4} m^3	CG2 volume at $\theta = 0$
d_p	0.7 m	Distance from axis of rotation to payload's center of mass
τ_f^+	0.2 Nm	Friction model parameter
τ_f^-	-0.5 Nm	Friction model parameter
P_s	675 kPa absolute	Supply pressure

Table 3.4 Tuned controller parameters

Parameter	Value	Description
K_P	500 Nm/rad	Pneumatic position controller gain
K_D	6 Nms/rad	Pneumatic position controller gain
$K_{P,m}$	700 Nm/rad	Electric position controller gain
$K_{D,m}$	5 Nms/rad	Electric position controller gain
K_P'	70 s^{-1}	Pressure controller gain
K_I	50 s^{-2}	Pressure controller gain
λ^+	0.004 Nm	Friction compensator parameter
λ^-	0.004 Nm	Friction compensator parameter
δ	8×10^{-5} rad	Friction compensator parameter
$\tau^*_{f,min}$	-1.5 Nm	Friction compensator parameter
$\tau^*_{f,\max}$	1.5 Nm	Friction compensator parameter
C_f	0.9	Payload estimator parameter
$S_{threshold}$	0.2	Payload estimator parameter
$\tau_{e,\text{threshold}}$	0.5 Nm	Payload estimator parameter

3.8.1 Identification of Inverse Valve Models

Identification of the inverse valve models is a prerequisite for implementation of the two pressure control loops. The pressure and duty cycle data were acquired using the procedure given in [27]. Next, the coefficients of the polynomials in (3.20) were calculated using least squares curve fitting. To keep the models parsimonious and avoid overfitting, the model orders were chosen as the smallest values that yielded an acceptable fitting error. The chosen values are $A=1,\ B=3,$ and $G=3.$ The fit had RMSE values of 3.4% and 3.7% for u_1 and u_2, respectively. Note that these models are different than in [27] due to the higher supply pressure used in this paper (i.e., 675 kPa vs. 480 kPa [27]).

3.8.2 Performance of the Pressure Control Loops

The gains of the two inner-loop pressure controllers (3.21) must be manually tuned before the outer-loop position controller can be implemented. The tuning was performed with the arm fixed at $\theta = 90°$. With the arm fixed, a smooth

desired pressure trajectory was used with one CG, while the other CG was left open to the atmosphere. This process was then repeated for the other CG. Figure 3.8 shows the results of this process for CG1. The pressure tracking resulted in an RMSE of 1.90 kPa (0.3% of $\max(P_{1d})$) and Maximum Absolute Error (MaxAE) of 5.1 kPa (0.8%) averaged over five experiments. Similar RMSE and MaxAE values were obtained with CG2. Figure 3.8 also shows that the control signal, u_1, is fairly smooth and does not saturate.

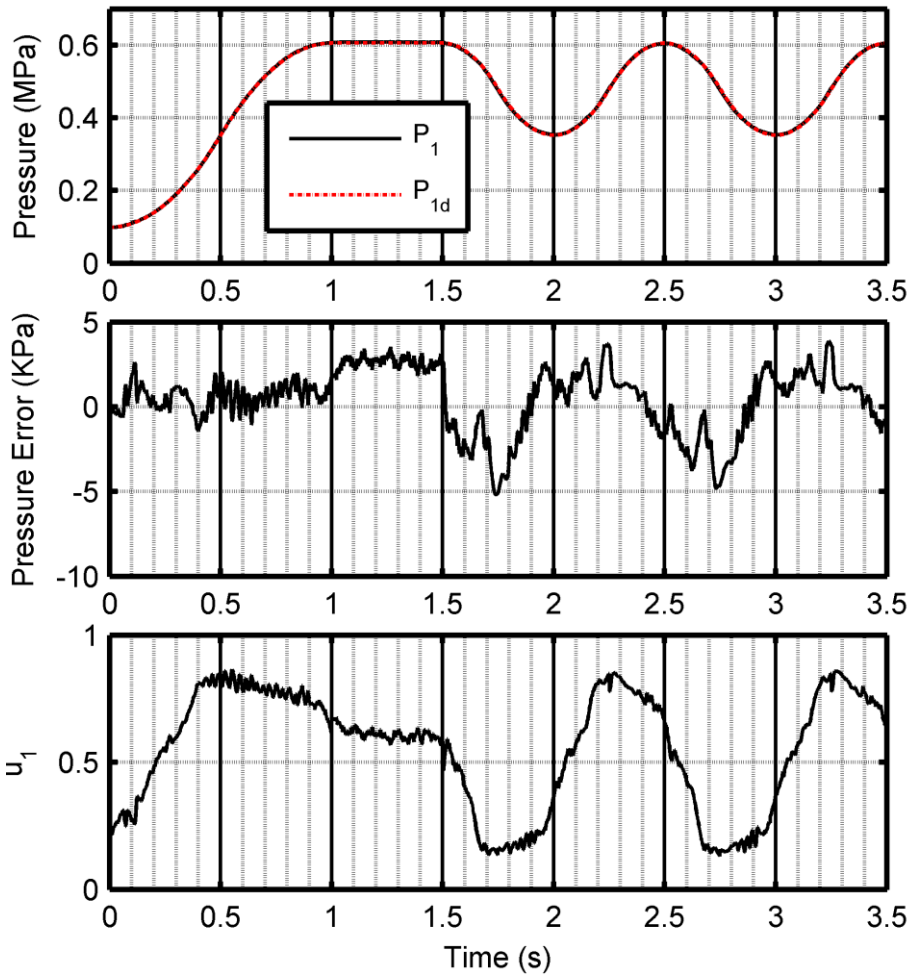

Figure 3.8 Experimental pressure control result for CG1.

3.8.3 Performance of the Position Control

A multi-cycloidal trajectory similar to that used in [6] was tested next. Example results are plotted in Figure 3.11. The pneumatic torque, τ_p, was calculated using the measured pressures and (3.2). The electric torque, τ_m,was calculated using u_m and (3.9). These torques will be discussed later. A slower multi-cycloidal trajectory similar to that used in [20] has also been used for this experiment to facilitate comparison. Tracking small moves can be a challenge for servo systems due to stiction effects. Thus a 0.045° move has been

added to the multi-cycloidal trajectory to further challenge the position controller and friction compensator.

This move has been added to the 90° section where the gravity torque is near its maximum. Figure 3.12 shows the overall results and Figure 3.13 shows a magnified view of the small move. It can be seen that both actuators are responsive to the 0.045° change in trajectory. The pneumatic actuator shows some overshoot tendency in positive direction movements but the electric motor successfully removes the overshoot for the hybrid case. The observed SSE for both actuators was less than or equal to the encoder resolution i.e. 0.0045°. Comparing the torque plots in Figures 3.11 and 3.12, it can be observed that the electric motor's contribution is much smaller with the slower trajectory in Figure 3.12. The reason is the pneumatic actuator was fast enough to supply most of the required torque with the slower trajectory, but with the fast trajectory more of the fast torque from the motor was necessary. Experiments were performed five times for each trajectory. The maximum absolute error (MaxAE) and RMSE values were calculated and averaged. Table 3.5 lists the averaged results. In this table, the 0.5 Hz sinusoidal trajectory, 1 Hz sinusoidal trajectory experiment, fast multi-cycloidal trajectory, and slow multi-cycloidal trajectory with 0.045° move are numbered 1-4, respectively.

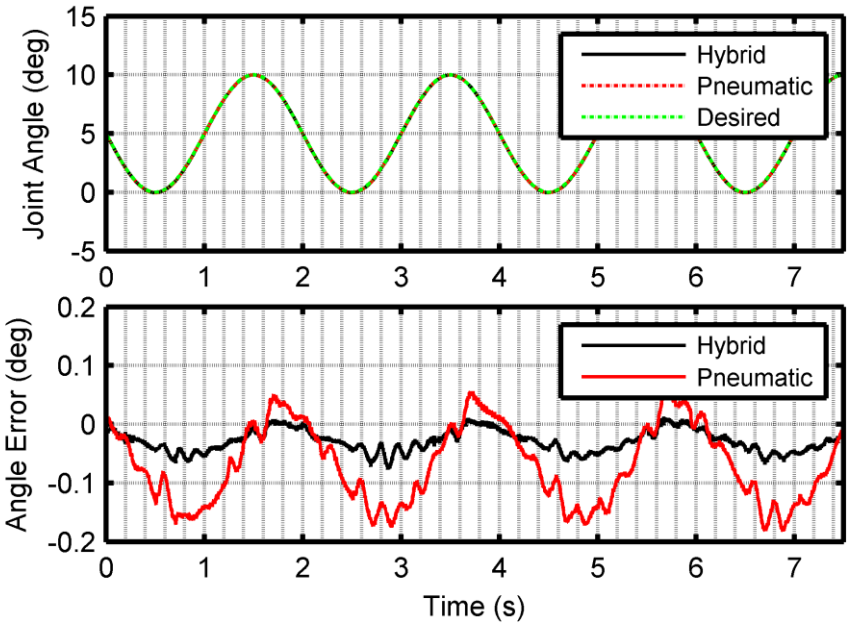

Figure 3.9 Experimental position control results for 0.5 Hz sinusoidal desired trajectory.

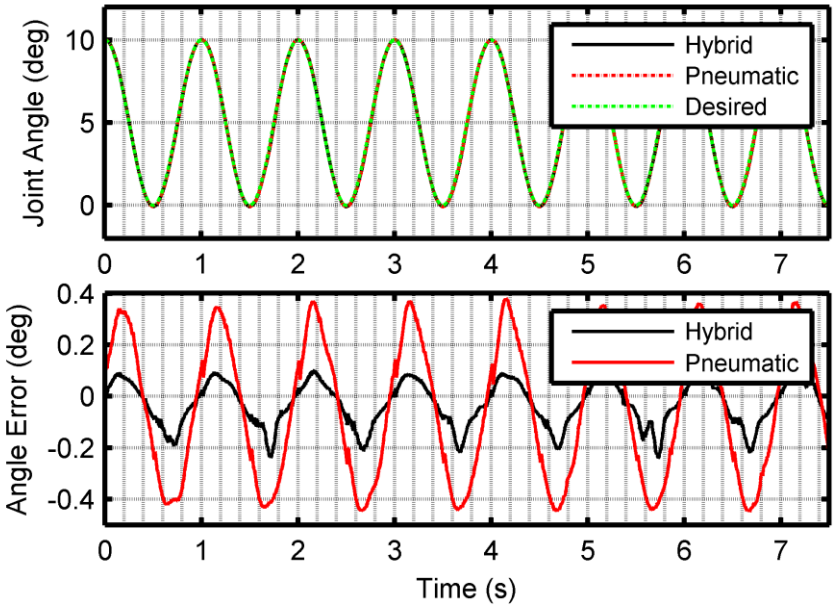

Figure 3.10 Experimental position control results for 1 Hz sinusoidal desired trajectory.

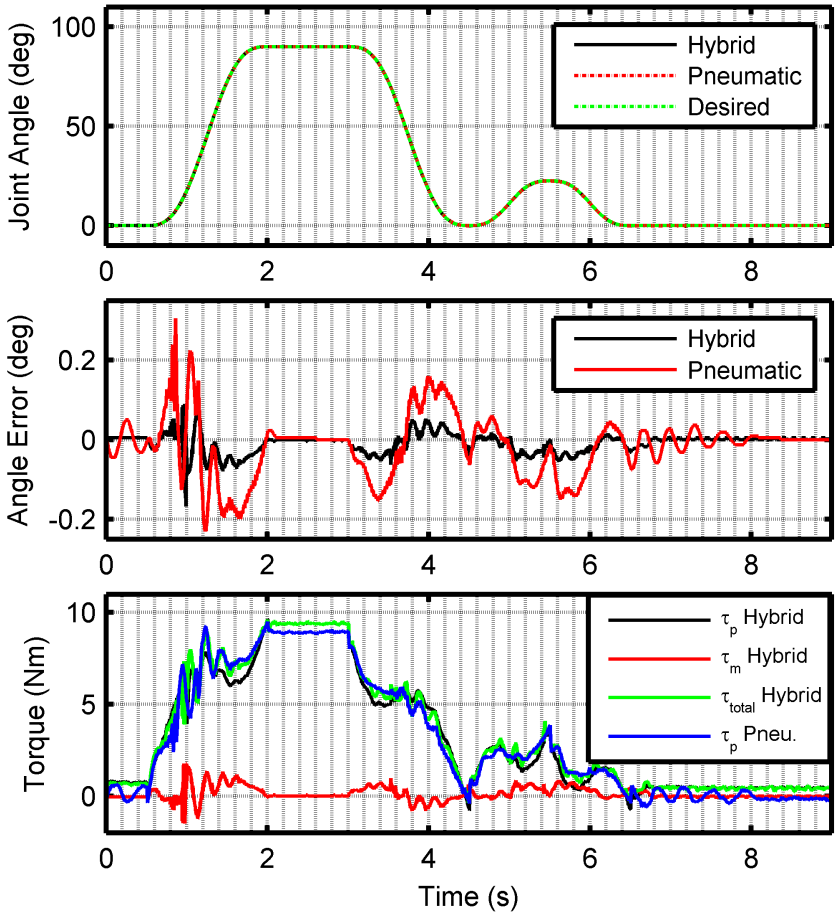

Figure 3.11 Experimental position control results when tracking the fast multi-cycloidal trajectory. $\tau_{total} = \tau_p + \tau_m$ is the total torque for the hybrid actuator.

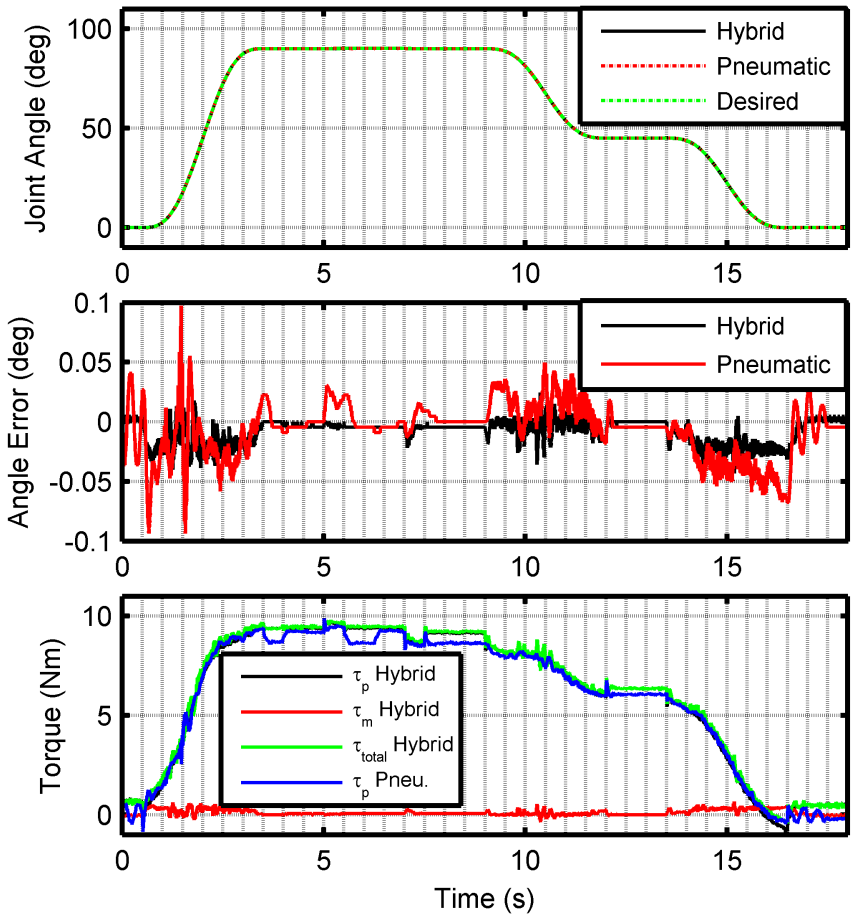

Figure 3.12 Experimental position control results for the pneumatic and the hybrid actuators tracking the slower multi-cycloidal trajectory containing a 0.045° move. $\tau_{total} = \tau_p + \tau_m$ is the total torque for the hybrid actuator.

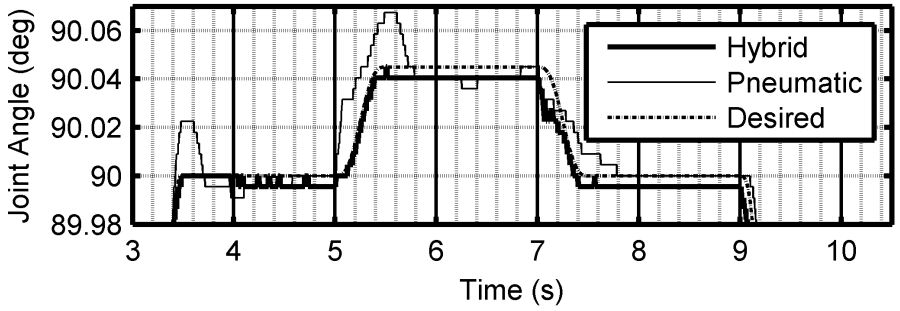

Figure 3.13 Magnified view of the results for a 0.045° move.

With trajectories 1, 2 and 3 a similar large RMSE reduction was observed when the hybrid actuator was used instead of the pneumatic one (64.6%, 65.6% and 67.6%, respectively).

For trajectory 4 this RMSE reduction was 55.7%. The reason for smaller reduction was the use of a slower trajectory which was less challenging for the pneumatic actuator. The hybrid actuator also reduced the MaxAE by 60.3%, 44.5%, 45.2%, and 55.7% for trajectories 1 to 4, respectively.

Table 3.5 Position control experimental results

Trajectory No.	Pneumatic Actuator		Hybrid Actuator	
	RMSE	MaxAE	RMSE	MaxAE
1	0.096°	0.194°	0.034°	0.077°
2	0.273°	0.454°	0.094°	0.252°
3	0.074°	0.305°	0.024°	0.167°
4	0.023°	0.097°	0.012°	0.043°

3.8.4 Robustness To Unknown Payloads

To evaluate the robustness of the control system to unknown payloads, the controller parameters were fixed and two different payloads were used. The first produced a 53% decrease in payload inertia relative to its nominal value, while the second produced a 34.7% increase in relative inertia. In Figure 3.14, example experimental results are shown for the tracking errors with, and without, the payload estimator. A multiple cycloidal trajectory identical to the one in Figure 3.11 was used for these tests. The results of the various test conditions are presented in Table 3.6. These values were obtained by averaging the RMSE and MaxAE values from five experiments performed at each test condition. They clearly demonstrate that improved position tracking was obtained when the offline payload estimator was used.

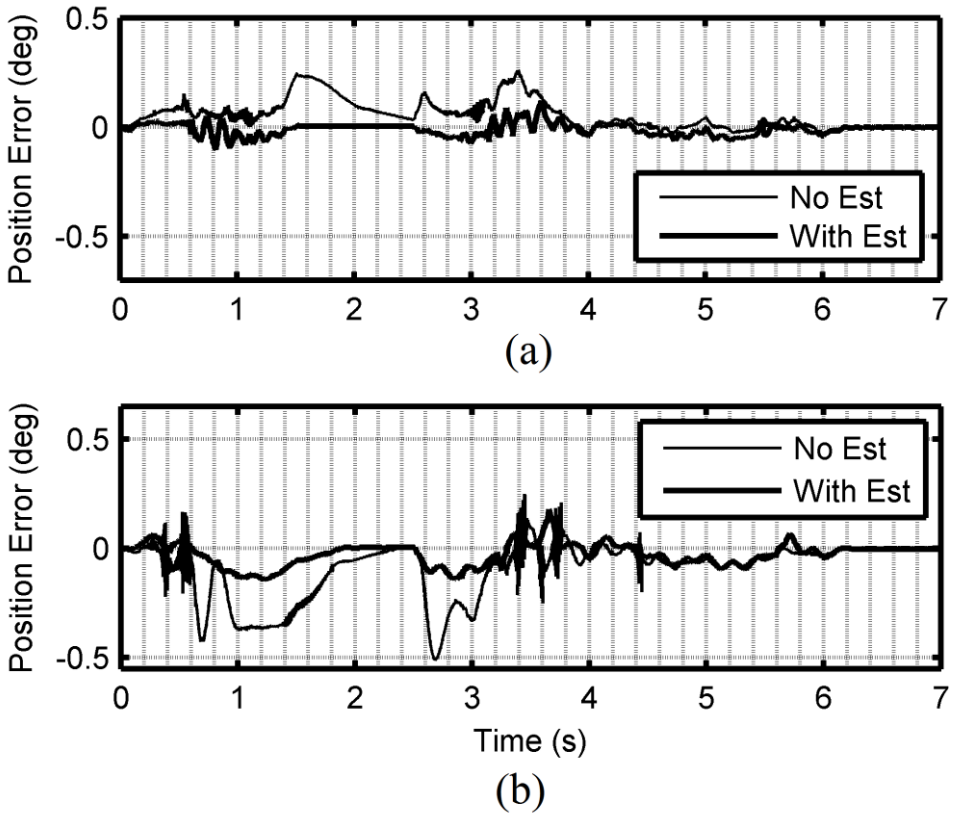

Figure 3.14 Tracking errors for unknown payload experiments with and without using the payload estimator for: (a) lower-than-nominal payload, and (b) higher-than-nominal payload.

Table 3.6 Payload robustness experimental results

Payload	Estimator Status	RMSE (deg)	MaxAE (deg)
Nominal	Off	0.024	0.167
Light	Off	0.076	0.262
(-53.0%)	On	0.027	0.121
Heavy	Off	0.139	0.513
(+34.7%)	On	0.052	0.178

3.8.5 Comparison With State of the Art

The best performances for a position controlled high torque pneumatic rotary actuator and position controlled HPEA were reported in [6] and [20], respectively. In [6] the SSE of the pneumatic actuator for a trajectory similar to trajectory 3 was about 2°, compared to

0.0045° in this paper. The RMSE of 4° from [6] was 53 times larger. Compared to the pneumatic actuator results in [27], the RSME with trajectory 3 was reduced by 56% (i.e., 0.074° vs. 0.169°). For the HPEA with similar hardware used in [20], the RMSE reported for trajectory 4 were 0.096° and 0.038° for the pneumatic and hybrid actuators, respectively. Thus the use of the model-based pressure controller and improved friction compensator in this paper has led to RMSE reductions of 76% and 68.4% for the pneumatic and the hybrid actuator, respectively.

3.9 Conclusion

In this paper a new HPEA design is presented with significantly higher torque output than previous designs, while maintaining the low mechanical impedance and inherent safety of the HPEA approach. This design is cost efficient since it does not require a high precision gearbox or harmonic drive to connect the motor to the output shaft, and uses solenoid on/off valves rather than costly proportional/servo valves. The HPEA is controlled by two inner-loop pressure controllers and an outer-loop position controller. The accuracy of the empirical inverse valve model enabled the pressure controllers to achieve high performance. Based on numerous experiments, the combination of adaptive friction compensation, model-based feedforward compensation, feedback compensation and offline payload estimation allowed the HPEA to outperform the state of the art in terms of position RMSE and SSE. Dynamic models were developed for a constrained impact between a human head and robot arm powered by either the HPEA, a pneumatic actuator, or a conventional electric actuator. The simulation results showed that the HPEA produced the smallest impact force. The proposed HPEA can provide future collaborative robot arms with precise positioning, better inherent safety than conventional actuators, and lower production cost.

References

[1] M. Zinn, B. Roth, O. Khatib, and J. K. Salisbury, “A new actuation approach for human friendly robot design,” *Int. J. Rob. Res.*, vol. 23, no. 4–5, pp. 379–398, 2004.

[2] A. K. Paul, J. K. Mishra, and M. G. Radke, “Reduced order sliding mode control for pneumatic actuator,” *IEEE Trans. Contr. Syst. Technol.*, vol. 2, pp. 271–276, 1994.

[3] X. Shen, J. Zhang, E. Barth, and M. Goldfarb, “Nonlinear model-based control of pulse width modulated pneumatic servo systems”, *ASME J. Dyn. Syst. Meas. Control*, vol. 128, pp. 663–669, 2006.

[4] T. Nguyen, J. Leavitt, F. Jabbari, and J. E. Bobrow, “Accurate sliding mode control of pneumatic systems using low-cost solenoid valves,” *IEEE/ASME Trans. Mechatron.*, vol. 12, no. 2, pp. 216–219, 2007.

[5] S. Hodgson, M. Tavakoli, M. T. Pham and A. Leleve, “Nonlinear discontinuous dynamics averaging and pwm-based sliding control of solenoid-valve pneumatic actuators,” *IEEE/ASME Trans. Mechatron.*, vol. 20, no. 2, pp. 876–888, 2015.

[6] J. Bobrow and B. McDonell, “Modeling, identification, and control of a pneumatically actuated, force controllable robot,” *IEEE Trans. Robot. Autom.*, vol. 14, no. 5, pp. 732–742, 1998.

[7] M. A. Azman, A.A.M. Faudzi, M.O. Elnimair, O.F. Hikmat, K. Osman, and K.C. Chang, “P-Adaptive Neuro-Fuzzy and PD-Fuzzy controller design for position control of a modified single acting pneumatic cylinder,” in *Proc. IEEE/ASME Int. Conf. Adv. Intel. Mechatron.*, 2013, pp.176–181.

[8] R. Rahman, L. He and N. Sepehri, "Design and experimental study of a dynamical adaptive backstepping-sliding mode control scheme for position tracking and regulating of a low-cost pneumatic cylinder", *Int. J. Robust Nonlin.*, vol. 26, no. 4, pp. 853–875, 2015.

[9] C. K. Chen and J. Hwang, “Iterative learning control for position tracking of a pneumatic actuated X–Y table,” *Control Eng. Pract.*, vol. 13, pp.1455–1461, 2005.

[10] Z. Rao and G. M. Bone, “Nonlinear modeling and control of servo pneumatic actuators,” *IEEE Trans. Control Syst.*, vol. 16, pp. 562–569, 2008.

[11] R. B. van Varseveld and G. M. Bone, “Accurate position control of a pneumatic actuator using on/off solenoid valves,” *IEEE/ASME Trans. Mechatron.*, vol. 2, no. 3, pp. 195–204, 1997.

[12] L. J. Petrosky, “Hybrid electro-pneumatic robot joint actuator,” U.S. Patent 478 225 828, October 1987.

[13] F. Takemura, S. Pandian, Y. Nagase, H. Mizutani, Y. Hayakawa, and S. Kawamura, “Control of a hybrid pneumatic/electric motor,” in *Proc. IEEE/RSJ Int. Conf. Intelligent Robots and Syst.*, 2000, pp. 209–214.

[14] D. Shin, I. Sardellitti, and O. Khatib, “A hybrid actuation approach for human-friendly robot design,” in: *Proc. IEEE Int. Conf. Robot. Autom.*, 2008, pp. 1747–1752.

[15] G. M. Bone and X. Chen, “Position control of hybrid pneumatic-electric actuators,” in *Proc. American Control Conf.*, 2012, pp. 1793–1799.

[16] T. Teramae, T. Noda, Sang-Ho Hyon, and J. Morimoto, “Modeling and control of a Pneumatic-Electric hybrid system,” in *2013 IEEE/RSJ Int. Conf. Intelligent Robots and Systems*, 2013, vol. 4, no. 8, pp. 4887–4892.

[17] Y. Nakata, T. Noda, J. Morimoto, and H. Ishiguro, “Development of a pneumatic-electromagnetic hybrid linear actuator with an integrated structure,” in *2015 IEEE/RSJ Int. Conf. Intelligent Robots and Systems*, 2015, pp. 6238–6243.

[18] K. Ishihara and J. Morimoto, “An optimal control strategy for hybrid actuator systems: Application to an artificial muscle with electric motor assist,” *Neural Networks*, vol. 99, pp. 92-100, 2018.

[19] G. M. Bone, M. T. Xue and J. Flett, "Position control of hybrid pneumatic–electric actuators using discrete-valued model-predictive control", *Mechatronics*, vol. 25, pp. 1–10, 2015.

[20] G. Ashby and G. M. Bone, "Improved hybrid pneumatic-electric actuator for robot arms", in *Proc. IEEE Int. Conf. Advanced Intelligent Mechatronics*, Banff, Canada, 2016, pp. 100–106.

[21] J. F. Carneiro and F. G. Almeida, “Modeling Pneumatic Servovalves Using Neural Networks,” in *Proc. IEEE Conf. Computer Aided Control Systems Design*, Munich, Germany, 2006, pp. 790–795.

[22] B. Rouzbeh and G. M. Bone, "Impact force reduction strategies to achieve safer human-robot collisions," in *Proc. CSME Int. Congr. 2018,* Toronto, Canada, 2018.

[23] S. Davis and D. G. Caldwell, "Braid effects on contractile range and friction modeling in pneumatic muscle actuators," *Int. J. Robot. Res.*, vol. 25 no. 4, pp. 359–369, 2006.

[24] Universal Robots (2015). Max. Joint Torques - 17260 [Online]. Available: http://www.universal-robots.com/how-tos-and-faqs/faq/ur-faq/max-joint-torques-17260/.

[25] CRS Robotics, *A465 Robot Arm User Guide,* 2000.

[26] Cleveland Motion Controls, *Torquemaster Brush Servo Motors 3500 Series Characteristics,* 2002.

[27] B. Rouzbeh, G. M. Bone and G. Ashby, "High accuracy position control of a rotary pneumatic actuator," *IEEE/ASME Trans. Mechatron.*, Accepted, DOI 10.1109/TMECH.2018.2870177.

[28] M. Van Damme, B. Vanderborght, B. Verrelst, R. Van Ham, F. Daerden, and D. Lefeber, "Proxy-based sliding mode control of a planar pneumatic manipulator," *Int. J. Rob. Res.*, vol. 28, no. 2, pp. 266–284, 2009.

[29] *ISO/TS 15066:2016, Robots and robotic devices - Collaborative robots*. International organization for standardization, 2016.

[30] Zeng, L. and Bone, G. M., "Design of Elastomeric Foam-Covered Robotic Manipulators to Enhance Human Safety," *Mech. Mach. Theory*, vol. 60, pp. 1-27, 2013.

[31] *ISO 10218-1:2011, Robots for industrial environments – Safety requirements – Part I: Robot*. International organization for standardization, 2011.

Chapter 4. Optimal Force Allocation and Position Control of Hybrid Pneumatic–Electric Linear Actuators

Abstract

Hybrid pneumatic–electric actuators (HPEAs) are redundant actuators that combine the large force, low bandwidth characteristics of pneumatic actuators with the large bandwidth, small force characteristics of electric actuators. It has been shown that HPEAs can provide both accurate position control and high inherent safety, due to their low mechanical impedance, making them a suitable choice for driving the joints of assistive, collaborative, and service robots. If these characteristics are mathematically modeled, input allocation techniques can improve the HPEA's performance by distributing the required input (force or torque) between the redundant actuators in accordance with each actuator's advantages and limitations. In this paper, after developing a model for a HPEA-driven system, three novel model-predictive control (MPC) approaches are designed that solve the position tracking and input allocation problem using convex optimization. MPC is utilized since the input allocation can be embedded within the motion controller design as a single optimization problem. A fourth approach based on conventional linear controllers is included as a comparison benchmark. The first MPC approach uses a model that includes the dynamics of the payload and pneumatics; and performs the motion control using a single loop. The latter methods simplify the MPC law by separating the position and pressure controllers. Although the linear controller was the most computationally efficient, it was inferior to the MPC-based controllers in position tracking and force allocation performance. The third MPC-based controller design demonstrated the best position tracking with RMSE of 46%, 20%, and 55% smaller than the other three approaches. It also demonstrated sufficient speed for real-time operation.

Keywords: redundant actuators; hybrid pneumatic–electric actuators; force allocation; model predictive control; assistive robots; collaborative robots; service robots.

4.1 Introduction

With the recent growth in assistive robots, collaborative robots, service robots, and their applications, enhancing robot safety has become an important area of research. These robots need to satisfy higher safety standards than conventional industrial robots [1]. Various approaches have been investigated for raising their level of safety. These approaches include active methods that monitor the environment and robot states using machine vision and/or sensor fusion and try to avoid risky situations; and passive methods that try to develop inherently safe robots that are not able to cause high damage in cases of system failure or unpredicted situations. Using hybrid pneumatic–electric actuators (HPEA) to drive the robot's joints has been proposed as a solution to increase inherent safety without sacrificing precision [2,3].

Since the introduction of the HPEA idea in 1987 [4], different designs have been proposed to develop this type of actuator. They include a combination of a DC motor and a rotary pneumatic motor in parallel [5], pneumatic muscle actuators (PMA) with a DC motor [2,6,7,8], pneumatic cylinders with a DC motor [9,10], and a pneumatic cylinder integrated within a linear motor [11,12].

With a hybrid actuator like HPEA, two actuators with different characteristics are performing the same task, which results in actuator redundancy. Since each of these actuators has completely distinct capabilities, the HPEA's optimal performance can be obtained by systematically allocating the forces/torques between them according to their characteristics.

The motion controller structure for HPEAs and other redundant actuators incorporates three levels [13]: (1) The high-level motion controller that uses a control method to determine the virtual high-level inputs (force or torque), (2) The input allocation level that distributes the virtual inputs between the actuators using predefined algorithms, and (3) The internal controller within each actuator that defines the low level inputs (like command signals to the valves of rudder motors) that can provide the virtual input with enough

accuracy. With optimization-based motion controllers, it is possible to merge the motion control and input allocation problems and address them in a single control law.

Input allocation for redundant actuators has been a topic of interest mainly to control aircraft and autonomous vehicles. Several studies have been devoted to providing mathematical frameworks for the input allocation of dynamic systems. In [14], a modified quadratic programming method has been proposed to include the actuator rates and their bandwidth limitations within the standard quadratic programming problem for input allocation purposes. Optimization-based methods have been the most common allocation approaches in the literature. In [15], an optimal control approach is used with a generic linear plant model that can handle a redundant actuator tracking multi-sinusoidal reference. In [13], several optimization-based techniques have been presented to solve unconstrained and constrained input allocation problems for generic linear and nonlinear plant models. Since optimization-based approaches mostly require high computational load and implementation complexity, researchers have developed tools to help with implementing the optimization techniques with high computational efficiency (see [16–18]).

Although there have been some papers focused on position controller design for HPEAs [3,6,10], very few have used a controller that incorporates each actuator's characteristics and studied the allocation problem alongside the position control problem. In [7], an optimization method is proposed for the torque allocation of a HPEA consisting of a PMA and an electric motor. They proposed a two-stage optimization approach that can be used for redundant actuators that consist of a higher bandwidth actuator and a lower bandwidth one. Their approach approximates nonlinear open-loop pressure dynamics using a first-order linear model.

In this paper, the position control and force allocation problems are studied for a HPEA-driven system. The plant structure and its mathematical model are presented in the next section. Then, three novel model predictive control (MPC) laws for this system are designed and tested. The MPC method is used since it searches for an optimal set of inputs in real-time that minimize the designed objective function. This objective function

considers both the position trajectory tracking and input allocation criteria, as well as the constraints of each actuator and the plant. A fourth controller using conventional linear controllers with no systematic input allocation strategy is presented last. The four controllers are applied to a simulated plant and their performances are compared. The execution speed of each controller in relation to the real-time requirements is also studied.

4.2 Plant Dynamics

4.2.1 Plant Structure

The structure of the HPEA-driven system is shown in Figure 4.1. A load mass is moving linearly on a horizontal low-friction surface. Two independent actuators are directly exerting force on this load in parallel. The first actuator is a pneumatic double-acting cylinder (with its two chambers denoted A and B); and the second one is a linear motor. To control the flow to/from each chamber, a pair of two-way proportional valves are used that operate with electric command signals. Two pressure sensors and a linear position sensor provide real-time feedback of the chamber pressures and the load position.

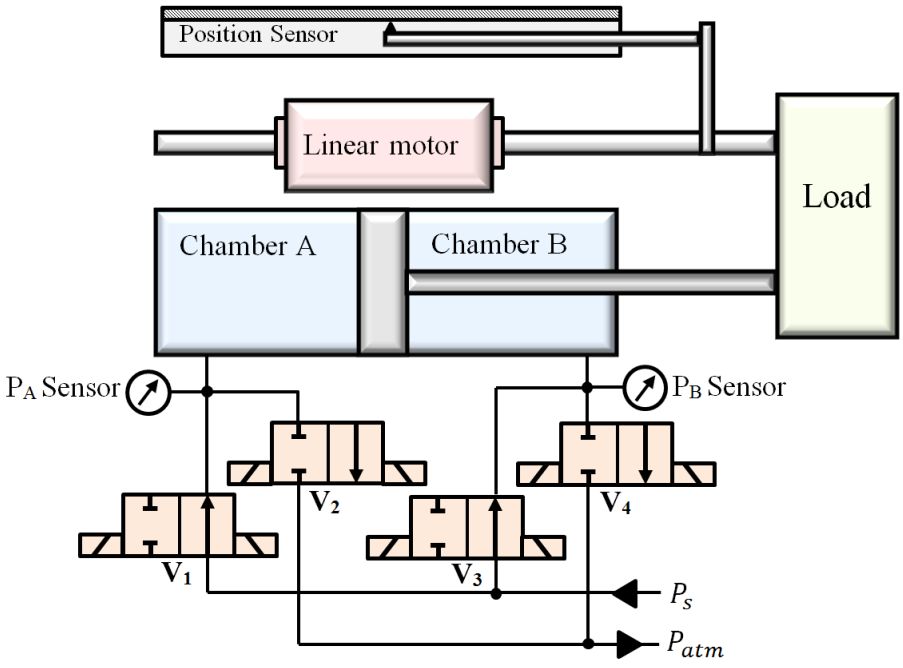

Figure 4.1 Schematic illustration of the HPEA-driven system.

4.2.2 Mathematical Model

In this section, mathematical equations are derived to model the system described in section 4.2.1. The dynamics of the load mass are defined by:

$$m_L \ddot{x}_p = F_p + F_e + F_f \tag{4.1}$$

where m_L, x_p, F_p, F_e, and F_f are the load mass, load position, the force from the pneumatic cylinder, the electric motor's force, and the total friction force, respectively. To keep the load motion range symmetric, its datum is located where the cylinder and the linear motor are in the middle of their range. The friction force is mainly from the pneumatic cylinder, and can be modeled as the sum of dry and viscous friction [19] as follows:

$$F_f = \begin{cases} -\left(F_p + F_e\right) & \dot{x}_p = 0 \text{ and } \left|F_p + F_e\right| < F_{sf} \\ -F_{sf}\, sign\left(F_p + F_e\right) & \dot{x}_p = 0 \text{ and } \left|F_p + F_e\right| > F_{sf} \\ -F_{kf}\, sign\left(\dot{x}_p\right) - C_v \dot{x}_p & \dot{x}_p \neq 0 \end{cases} \tag{4.2}$$

Typically, the electric motor's current input to force output response time is considerably smaller than the controller sampling period and the response times of other components. Thus, the motor's internal dynamics can be neglected. If the relation between the motor force and the current input to the motor is precisely known, we can consider F_e as an independent input to the position subsystem that can be provided accurately and instantaneously. The same assumptions cannot be made about the pneumatic force as it is a function of chamber pressures, which have significantly slower response time to the valve commands. In the next section, the pneumatic force's dynamic model is derived.

The pneumatic force is the result of the difference in the forces at the two sides of the piston, as indicated in (3). In this equation, P, A, and P_{atm} are the absolute chamber pressure, effective piston area of the chamber, and the atmospheric pressure, respectively.

$$F_p = (P_A - P_{atm})A_A - (P_B - P_{atm})A_B \tag{4.3}$$

Deploying conservation of mass, conservation of energy, and the ideal gas law for each chamber leads to (4.4) and (4.5) [20]. In these equations, $\dot{m}$, T, and R are the mass flow into the chamber, absolute temperature of the air, and specific gas constant of air (287 $J \cdot kg^{-1} \cdot K^{-1}$), respectively. L_S and L_{DV} are the stroke of the cylinder and equivalent length for the dead volume in each chamber, respectively.

$$\dot{P}_A = \frac{RT}{A_A(L_S/2 + L_{DV} + x_p)}\dot{m}_A - \frac{P_A}{L_S/2 + L_{DV} + x_p}\dot{x}_p \tag{4.4}$$

$$\dot{P}_B = \frac{RT}{A_B(L_S/2 + L_{DV} - x_p)}\dot{m}_B + \frac{P_B}{L_S/2 + L_{DV} - x_p}\dot{x}_p \tag{4.5}$$

Using the model for compressible flow through the orifice area and the ideal gas assumptions, the mass flow rate through each valve can be modeled as shown in (4.6) [21].

$$\dot{m}_v = \begin{cases} C_1 A_v C_f \dfrac{P_u}{\sqrt{T}}, & \dfrac{P_d}{P_u} \le P_{cr} \\ C_2 A_v C_f \dfrac{P_u}{\sqrt{T}} \left(\dfrac{P_d}{P_u}\right)^{1/K} \sqrt{1 - \left(\dfrac{P_d}{P_u}\right)^{(K-1)/K}}, & \dfrac{P_d}{P_u} \le P_{cr} \end{cases} \tag{4.6}$$

Here, C_f is the non-dimensional discharge coefficient of the valve, P_u is the upstream pressure, P_d is the downstream pressure, K is the ratio of specific heats for air (1.4), and A_v is the valve orifice area. The valve orifice area changes as the spool moves. For Enfield LS-V05s pneumatic valves, it has been shown [20] that the relation between the valve orifice area and the normalized spool displacement (z) can be approximated by fitting a curve in the form of (4.7), where λ_1, …, λ_7 are the coefficients calculated using experimental data points, and the least squares fitting method.

$$A_v = sign(z)\left(\lambda_1 + \lambda_2|z| + \lambda_3|z|^2 + \lambda_4|z|^3 + \lambda_5|z|^4\right)\left(1 - \tanh\left(\lambda_6|z| + \lambda_7\right)\right) \tag{4.7}$$

Since two-way valves are used in this study, each valve performs only one of the charging/discharging tasks; thus, $0 \le z \le 1$. Regarding [20], this normalized spool displacement inside each valve can be modeled as:

$$\dot{z} + \frac{1}{\tau_v} z = \frac{1}{\tau_v} u_v \tag{4.8}$$

In (4.8), u_v and τ_v are the normalized command to the valve and the spool time constant, respectively.

It should be noted that if a single three-way valve was used with each chamber, regarding (4.6) and (4.7), the pneumatic valve would switch between "charge" and "discharge" modes when the sign of spool displacement would change. Since the upstream and downstream pressures are different in each mode, there would be two distinct equations for the valve mass flow for charging and discharging. This would lead to a piecewise function for the mass flow rate of the valve. To be able to perform the controller in real-time, a linearized plant model with constant state space matrices is desirable (at least within the MPC prediction horizon). Therefore, a single mass flow equation is preferred to a piecewise function. Hence, the pneumatic circuit has been designed with a pair of two-way proportional valves for each chamber instead of a three-way proportional valve. With this structure (see Figure 1), the mass flow rates into the chambers are:

$$\dot{m}_A = \dot{m}_{V_1} - \dot{m}_{V_2} \tag{4.9a}$$

$$\dot{m}_B = \dot{m}_{V_3} - \dot{m}_{V_4} \tag{4.9b}$$

4.3 Controller Design

In this section, four different controllers are designed to address the position control and input allocation tasks for the HPEA-driven system. The first three controllers employ MPC for position control, while the fourth employs conventional linear controllers.

4.3.1 MPC1: Controller with Linearized Full Plant Model

Assuming that the full plant model of Section 4.2 and its parameters are known, an MPC law may be used for both position control and force allocation, outputting the electric force command and the inputs to the valves. The mass flow rates into the chambers are calculated using (4.6), which is a function of the upstream and downstream pressures. We term this approach MPC1. The controller structure is shown schematically in Figure 4.2.

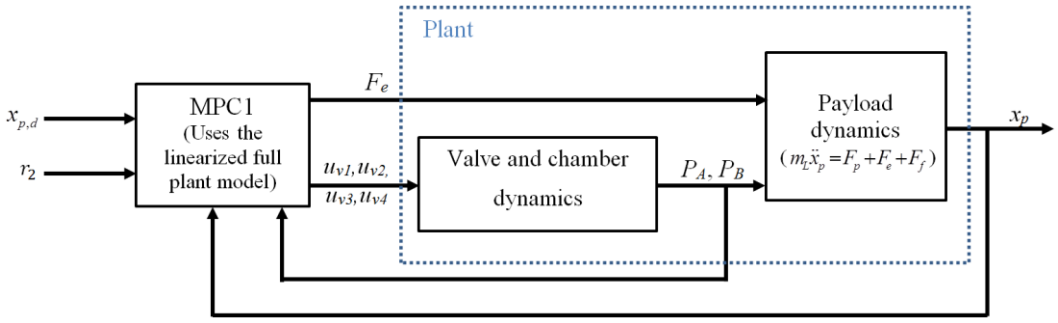

Figure 4.2 Controller structure used with MPC1.

The plant model must be linearized for use in the controller. The purpose of model linearization is to convert the nonlinear plant model into the linear discrete-time state space form of (4.10). The arguments k and $k + 1$ denote the kth and $(k + 1)$th samples.

$$\mathbf{x}(k+1) = \mathbf{A_d}\mathbf{x}(k) + \mathbf{B_d}\mathbf{u}(k) + \boldsymbol{\upsilon}(k) \tag{4.10a}$$

$$\mathbf{y}(k) = \mathbf{C_d}\mathbf{x}(k) + \mathbf{D_d}\mathbf{u}(k) \tag{4.10b}$$

To obtain the state space matrices (i.e., $\mathbf{A_d}$, $\mathbf{B_d}$, $\mathbf{C_d}$, and $\mathbf{D_d}$), Equations (4.1) and (4.4)–(4.6) are first used to derive the following vector equations:

$$\dot{\mathbf{x}} = \mathbf{f}(\mathbf{x},\mathbf{u}) \tag{4.11a}$$

$$\mathbf{y} = \mathbf{g}(\mathbf{x},\mathbf{u}) \tag{4.11b}$$

Given (4.11), the continuous-time state space matrices can be calculated as shown in (4.12). The discrete-time matrices can be simply calculated by applying a discretization method

to the matrices from (4.12). We used Euler's method to obtain the matrices as shown in (4.13).

$$\mathbf{A_c} = \left.\frac{\partial \mathbf{f}}{\partial \mathbf{x}^T}\right|_{op} \tag{4.12a}$$

$$\mathbf{B_c} = \left.\frac{\partial \mathbf{f}}{\partial \mathbf{u}^T}\right|_{op} \tag{4.12b}$$

$$\mathbf{C_c} = \left.\frac{\partial \mathbf{g}}{\partial \mathbf{x}^T}\right|_{op} \tag{4.12c}$$

$$\mathbf{D_c} = \left.\frac{\partial \mathbf{g}}{\partial \mathbf{u}^T}\right|_{op} \tag{4.12d}$$

$$\mathbf{A_d} = \mathbf{I} + T_s\mathbf{A_c} \tag{4.13a}$$

$$\mathbf{B_d} = T_s\mathbf{B_c} \tag{4.13b}$$

$$\mathbf{C_d} = \mathbf{C_c} \tag{4.13c}$$

$$\mathbf{D_d} = \mathbf{D_c} \tag{4.13d}$$

In (4.13a), $\mathbf{I}$ is the identity matrix and T_s is the controller sampling period. The full matrices are presented in Appendix A. The subscript "*op*" indicates linearization about an operating point. This is a point that includes states and inputs, as shown in (4.14).

$$\mathbf{x}_{op} = \begin{bmatrix} P_{A_{op}} & P_{B_{op}} & x_{p_{op}} & \dot{x}_{p_{op}} \end{bmatrix}^T \tag{4.14a}$$

$$\mathbf{u}_{op} = \begin{bmatrix} u_{v1_{op}} & u_{v2_{op}} & u_{v3_{op}} & u_{v4_{op}} & F_{e_{op}} \end{bmatrix}^T \tag{4.14b}$$

There are different options for selecting the operating point (4.14). One option is to use the current system states and input, i.e., $P_{A_{op}} = P_A(k)$, $P_{B_{op}} = P_B(k)$, $x_{p_{op}} = x_p(k)$, $\dot{x}_{p_{op}} = \dot{x}_p(k)$, $u_{vi_{op}} = u_{vi}(k-1)$, and $F_{e_{op}} = F_e(k-1)$. If this option is chosen, the operating point and the state space matrices need to be recalculated with every controller sampling period, passed to the MPC's optimization solver, and then, kept constant within the prediction horizon. Note that the mass flow rate through each valve is modeled using distinct equations for the choked and unchoked modes (see (4.6)). Having four valves and each valve having two modes means there are 16 distinct versions of $\mathbf{f}$ and $\mathbf{g}$. With each iteration, the correct version of the functions must be chosen (depending on the valve modes) and used in (4.12) to update the state space matrices. This makes the resulting MPC too computationally complex to implement with common processors at the 10 ms or faster sampling period required for this application. To achieve a computationally feasible controller, we instead use a fixed operating point for the plant model linearization. This leads to only one version for each of the state space matrices (instead of the 16 versions with the dynamic operating point).

The following three assumptions are made to derive the linear model about a fixed operating point: (4.1) The states and inputs stay close enough to the operating point, (4.2) Valve spool time-constant (τ_v) is small enough compared to the controller sampling time that the spool's dynamics can be neglected and $z = u_v$, and (4.3) Since the model is linearized about a constant operating point, the valve orifice area function in (4.7) may be replaced by a linear function of $A_v = \lambda_8 z + \lambda_9$ so that this single point will convey more information about the trend of the whole function. The state space state, input, and output vectors are shown below.

$$\mathbf{x}(k) = \begin{bmatrix} P_A(k) - P_{A_{op}} & P_B(k) - P_{B_{op}} & x_p(k) - x_{p_{op}} & \dot{x}_p(k) - \dot{x}_{p_{op}} \end{bmatrix}^T \tag{4.15a}$$

$$\mathbf{u}(k) = \begin{bmatrix} u_{v1}(k) - u_{v1_{op}} & u_{v2}(k) - u_{v2_{op}} & u_{v3}(k) - u_{v3_{op}} & u_{v4}(k) - u_{v4_{op}} & F_e(k) - F_{e_{op}} \end{bmatrix}^T \tag{4.15b}$$

$$\mathbf{y}(k)=\begin{bmatrix} x_p(k)-x_{p_{op}} & \dfrac{(P_A(k)-P_{A_{op}})+(P_B(k)-P_{B_{op}})}{2} \end{bmatrix}^T \tag{4.15c}$$

From (4.3), it can be seen that the cylinder can have infinite combinations of chamber pressures that produce the same pneumatic force. The strategy behind defining the second output is to limit the pressure choices by keeping the average of chambers pressures near $P_{mid}=\left(P_s+P_{atm}\right)/2$, which means requiring the second output to track a constant reference of $r_2=P_{mid}-\left(P_{A_{op}}+P_{B_{op}}\right)/2$. In this paper, the operating point elements have been picked as $\mathbf{u}_{op}=0$, $x_{p_{op}}=0$, and $\dot{x}_{p_{op}}=0$. The operating points for chamber pressures have been chosen such that they satisfy $(P_{A_{op}}-P_{atm})A_A-(P_{B_{op}}-P_{atm})A_B=0$ and $\left(P_{A_{op}}+P_{B_{op}}\right)/2=P_{mid}$. Therefore, the pressure operating points are:

$$P_{A_{op}}=\frac{2P_{mid}+\left(\dfrac{A_A}{A_B}-1\right)P_{atm}}{\dfrac{A_A}{A_B}+1} \tag{4.16a}$$

$$P_{B_{op}}=\frac{2P_{mid}+\left(\dfrac{A_B}{A_A}-1\right)P_{atm}}{\dfrac{A_B}{A_A}+1} \tag{4.16b}$$

The MPC1 law uses (4.10) to predict the future states. It solves the optimization problem (4.17) every sampling instant with a prediction horizon of N_p points, by using a time-efficient convex optimization algorithm. In (4.17), k is the current sample number, $\mathbf{r}=\begin{bmatrix} x_{p,d} & r_2 \end{bmatrix}^T$ is the vector of the two reference inputs, and $\mathbf{Q}$, $\mathbf{R_1}$, and $\mathbf{R_2}$ are positive-definite gain matrices.

$$
\begin{aligned}
&\textit{minimize} \quad \sum_{i=1}^{N_p} ((\mathbf{y}(k+i)-\mathbf{r}(k+i))^T \mathbf{Q}(\mathbf{y}(k+i)-\mathbf{r}(k+i))... \\
&\mathbf{u} \qquad\qquad + (\mathbf{u}(k+i))^T \mathbf{R}_1 \mathbf{u}(k+i) + (\mathbf{u}(k+i)-\mathbf{u}(k+i-1))^T \mathbf{R}_2 (\boldsymbol{u}(k+i)-\mathbf{u}(k+i-1)) \\
&\textit{subject to} \\
&\qquad \mathbf{x}(k+j+1) = \mathbf{A}_d \mathbf{x}(k+j) + \mathbf{B}_d \mathbf{u}(k+j) + T_s \mathbf{f}(\mathbf{x}_{op}, \mathbf{u}_{op}) \quad , j = 0,..., N_p - 1 \\
&\qquad \mathbf{y}(k+j) = \mathbf{C}_d \mathbf{x}(k+j) + \mathbf{D}_d \mathbf{u}(k+j) \quad , j = 1,..., N_p \\
&\qquad \mathbf{u}_{\min} \le \mathbf{u}(k+j) \le \mathbf{u}_{\max} \quad , j = 1,..., N_p \\
&\qquad \mathbf{x}_{\min} \le \boldsymbol{x}(k+j) \le \mathbf{x}_{\max} \quad , j = 1,..., N_p
\end{aligned}
\tag{4.17}
$$

4.3.2 MPC2: Simplified Two-Loop Controller

The MPC1 approach must solve an optimization problem every sampling period, which is computationally expensive since it includes models of both the payload dynamics and pneumatic dynamics. As a faster alternative, with our second approach, termed MPC2, the MPC law neglects the dynamics of the pneumatic subsystem. In other words, the MPC2 law assumes the actual pneumatic force equals its desired value, i.e., $F_p = F_{p,d}$. This design requires a two-loop controller structure as the MPC2 block is responsible for controlling the position subsystem solely. An inner-loop pressure controller handles the pneumatic subsystem and defines the command signals for each valve. The schematic of this control system structure is illustrated in Figure 4.3.

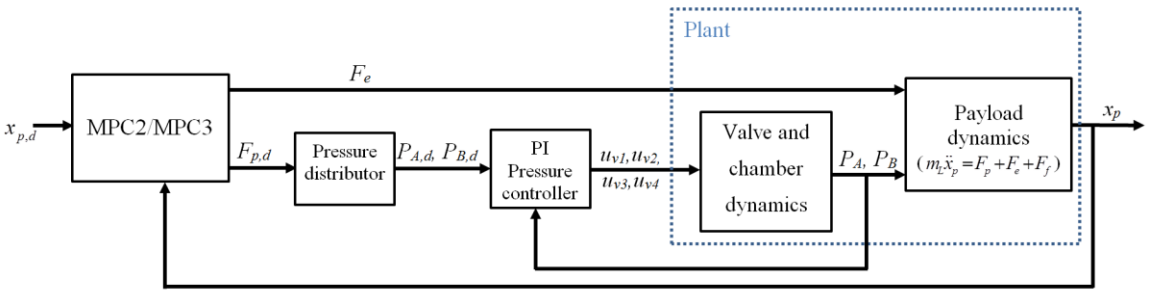

Figure 4.3 Controller structure used with MPC2 and MPC3.

MPC2 uses (4.1) to derive linear state space model as in (4.11) with the following states, inputs, and output. The corresponding state space model matrices are presented in Appendix A.

$$\mathbf{x}(k) = \begin{bmatrix} x_{p(k)} & \dot{x}_{p(k)} \end{bmatrix}^T \tag{4.18a}$$

$$\mathbf{u}(k) = \begin{bmatrix} F_{p,d(k)} & F_{e(k)} \end{bmatrix}^T \tag{4.18b}$$

$$\mathbf{y}(k) = x_{p(k)} \tag{4.18c}$$

The optimization problem declaration is almost the same as MPC1, with the only difference being adding one more constraint (shown in (4.19)) to limit the changes in $\mathbf{u}(k)$ between two consecutive samples. This change is necessary as MPC2 ignores the inner dynamics of the pressure subsystems and its limitations.

$$\Delta\mathbf{u}_{\min} \le \mathbf{u}(k+j) - \mathbf{u}(k+j-1) \le \Delta\mathbf{u}_{\max} \quad , j = 1, \ldots, N_p \tag{4.19}$$

Before feeding $F_{p,d}$ from the outer-loop position controller to the inner-loop pressure controller, the pressure distributor should define the desired chamber pressures. This is done by satisfying the two conditions $(P_{A,d}(k) - P_{atm})A_A - (P_{B,d}(k) - P_{atm})A_B = F_{p,d}(k)$ and $\left(P_{A,d}(k) + P_{B,d}(k)\right)/2 = P_{mid}$. The solution to these conditions is shown in (4.20).

$$P_{A,d(k)} = \frac{2P_{mid} + \left(\frac{A_A}{A_B} - 1\right)P_{atm} + \frac{F_{p,d(k)}}{A_B}}{\frac{A_A}{A_B} + 1} \tag{4.20a}$$

$$P_{B,d(k)} = \frac{2P_{mid} + \left(\frac{A_B}{A_A} - 1\right)P_{atm} - \frac{F_{p,d(k)}}{A_A}}{\frac{A_B}{A_A} + 1} \tag{4.20b}$$

A conventional PI controller, with a bounded trapezoidal integral term, is used to control chamber pressures as shown in (4.21). Here, Γ denotes the integral bound.

$$u_j(k) = K_{p,p}\left(P_{j,d}(k) - P_j(k)\right) + \min\left(\Gamma, \max\left(\varphi_j(k), -\Gamma\right)\right) \quad , \; j \in \{A, B\} \tag{4.21}$$

where $\varphi_j(k) = K_{I,p}\dfrac{T_s}{2}\sum_{\eta=2}^{k}\left(P_{j,d}(\eta) - P_j(\eta) + P_{j,d}(\eta-1) - P_j(\eta-1)\right)$.

The pressure controller in (4.21) returns a value for u_j that needs to be normalized and distributed between the charging and discharging valves. To do so, the distributor function, Ω, is used as follows.

$$\left[u_{v1}(k), u_{v2}(k)\right] = \Omega\left(u_A(k)\right) \tag{4.22a}$$

$$\left[u_{v3}(k), u_{v4}(k)\right] = \Omega\left(u_B(k)\right) \tag{4.22b}$$

where $\Omega(\varepsilon) = \begin{cases}\left[\min(\varepsilon, 1), 0\right] & \varepsilon \geq 0 \\ \left[0, \min(-\varepsilon, 1)\right] & \varepsilon < 0\end{cases}$

4.3.3. MPC3: Modified Two-Loop Controller

MPC1 and MPC2 are two extremes in terms of dynamic models for the pneumatic subsystem. MPC1 uses a linearized model of the pneumatic dynamics, whereas MPC2 neglects these dynamics. The MPC law proposed in this section, termed MPC3, is a compromise between these two extremes that is intended to balance the trade-off between performance and controller computation time. The controller structure of Figure 3 with the independent pressure controller is adopted, but the MPC position controller is expanded to include a simplified model of the pneumatic dynamics.

To obtain the simplified model for predicting the pneumatic force, F_p, we assume that the proportional term in (4.21) is dominant and that the derivative of each cylinder chamber pressure is approximately proportional to its associated valve command signal, i.e.,

$$\dot{P}_A \cong \Psi u_A \cong \Psi K_{p,p}\left(P_{A,d} - P_A\right) \tag{4.23a}$$

$$\dot{P}_B \cong \Psi u_B \cong \Psi K_{p,p}\left(P_{B,d} - P_B\right) \tag{4.23b}$$

Substituting (4.23) into (4.3) then gives the following simplified dynamic model for the pneumatic force:

$$\dot{F}_p = \kappa(F_{p,d} - F_p) \tag{4.24}$$

Finally, the discretized form of (4.24) is added to the state space model of MPC2 to produce the state space model used by MPC3. Its state vector is defined by (4.25). Its input vector and output are defined by (4.18a) and (4.18b), respectively. The corresponding state space model matrices are presented in Appendix A.

$$\mathbf{x}(k) = \begin{bmatrix} x_{p(k)} & \dot{x}_{p(k)} & F_{p(k)} \end{bmatrix}^T \tag{4.25}$$

4.3.4. Linear Two-Loop Controller

As a comparison benchmark, a conventional linear position controller was also designed and simulated. The controller structure is the same as that of Figure 3, except the MPC2 block is replaced with a linear position controller. This controller structure is similar to the two-loop structure used in [3]. Two independent controllers are used with the pneumatic and the electric actuators, with the former using feedforward + PD controller and the latter using a PD controller. Since the electric actuator has a faster response but significantly lower force capacity, the feedforward terms that compensate for the modeled inertial and friction forces are fed to the pneumatic actuator controller, while the electric actuator's force capacity is saved for reducing the residual error. The equations for these controllers are shown in (4.26) and (4.27).

$$F_{p,d}(k) = m_L \ddot{x}_{p,d}(k) + \hat{C}_v \dot{x}_p(k) + K_{P,c}\left(x_{p,d}(k) - x_p(k)\right) + K_{D,c}\left(\dot{x}_{p,d}(k) - \dot{x}_p(k)\right) \tag{4.26}$$

$$F_e(k) = K_{P,m}\left(x_{p,d}(k) - x_p(k)\right) + K_{D,m}\left(\dot{x}_{p,d}(k) - \dot{x}_p(k)\right) \tag{4.27}$$

4.4 Results and Discussion

The four controllers were simulated using MATLAB m code and Yalmip [16] running on a Windows 10 PC with an Intel Core i5 processor. To challenge the tracking and force allocation performance, a relatively large payload mass of $m_L = 10$ kg was used. The pneumatic actuator parameters for an SMC CM2XB25-300 air cylinder [19] and an Enfield LS-V05s pneumatic valve [20] were employed. The simulated linear motor is an Aerotech BLMC-92. To prevent motor overheating, the electric actuator's force has been limited to 30 N, which is lower than the 44.5 N continuous force rating of this Aerotech motor. All controller parameters were manually tuned with the goal of minimizing the root-mean-square error (RMSE). This tuning employed a coarse search followed by a fine search to reduce the possibility of stopping at a local minima. Table 4.1 lists the parameters used.

Table 4.1 Plant and controller parameters.

Parameter	Value	Parameter	Value
A_A	4.909×10^{-4} m^2	$\mathbf{Q}$ (MPC3)	10^6
A_B	4.123×10^{-4} m^2	R	287 J/kg·K
C_1	0.040418	$\mathbf{R}_1$ (MPC1)	diag([1, 1, 1, 1, 10^{-3}])
C_2	0.156174	$\mathbf{R}_1$ (MPC2)	diag([0.1, 0.5])
C_f	0.5393	$\mathbf{R}_1$ (MPC3)	diag([0.1, 0.5])
C_v	44.4 N·s/m	$\mathbf{R}_2$ (MPC1)	0
F_{kf}	13 N	$\mathbf{R}_2$ (MPC2)	diag([0.1, 0])
F_{sf}	18 N	$\mathbf{R}_2$ (MPC3)	diag([0.1, 0])
K	1.4	T	293 K
$K_{P,c}$	2000 N/m	Numerical integration timestep	0.0005 s
$K_{D,c}$	30 N·s/m	$\Delta\mathbf{u}_{\min}$ (MPC2)	$[-30, -60]^T$
$K_{P,m}$	500 N/m	$\Delta\mathbf{u}_{\max}$ (MPC2)	$[30, 60]^T$
$K_{D,m}$	50 N·s/m	Γ	5000 Pa·s
$K_{p,p}$	5×10^{-5} Pa^{-1}	κ	70
$K_{I,p}$	5×10^{-4} Pa^{-1}s^{-1}	λ_1	0.585
L_S	0.3 m	λ_2	−7.51

L_{DV}	0.03 m	λ_3	38.1
m_L	10 kg	λ_4	−46.9
N_P	15	λ_5	18.2
P_{atm}	101,000 Pa	λ_6	−21.3
P_{cr}	0.528	λ_7	3.42
P_s	404000 Pa	λ_8	5×10^{-5}
$\mathbf{Q}$ (MPC1)	diag([10^4, 10^{-3}])	λ_9	0
$\mathbf{Q}$ (MPC2)	10^6	τ_v	0.0015 s

To keep the models within the MPC-based controllers in linear time-invariant form, the static and kinetic friction components are treated as unmodeled disturbances. Only the viscous friction is incorporated in the MPC models, for which a 20% uncertainty is included in the friction coefficient $\hat{C}_v$ (i.e., $\hat{C}_v = 0.8C_v$). Figures 4.4–4.7 show the results from each controller. They follow a reference trajectory made up of step inputs, a 1 Hz sine wave, then a faster 4 Hz sine wave. This trajectory was chosen to be challenging and led to multiple saturations of the valve commands and electric actuator force (at 1 and 30 N, respectively), as shown in Figures 4.4–4.7. For easier comparison, the tracking errors are plotted on the same axes in Figure 4.8.

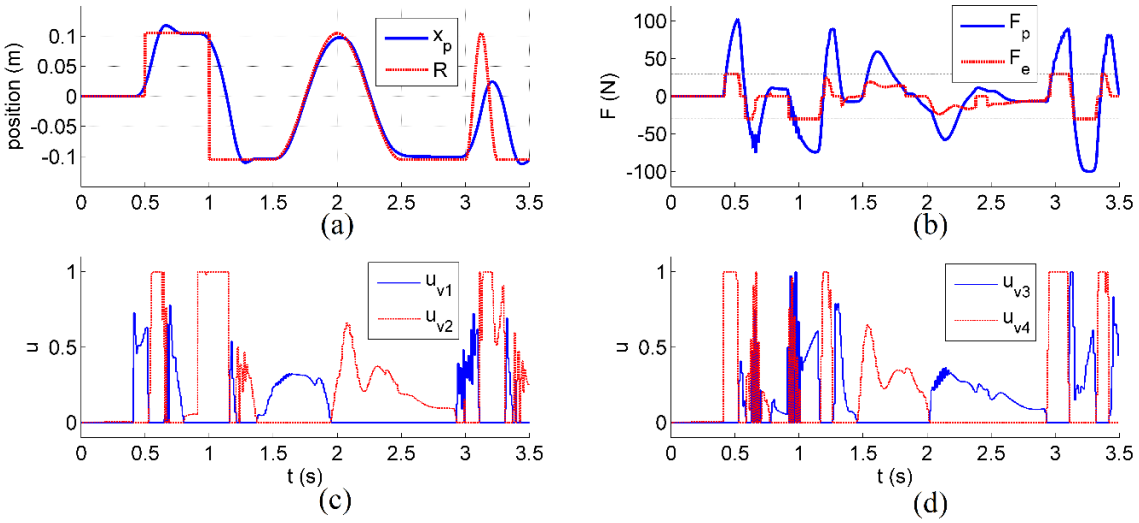

Figure 4.4 Position tracking and force allocation performance using MPC1: (**a**) position tracking, (**b**) actuator forces, (**c**) command to the valves controlling chamber A, and (**d**) command to the valves controlling chamber B.

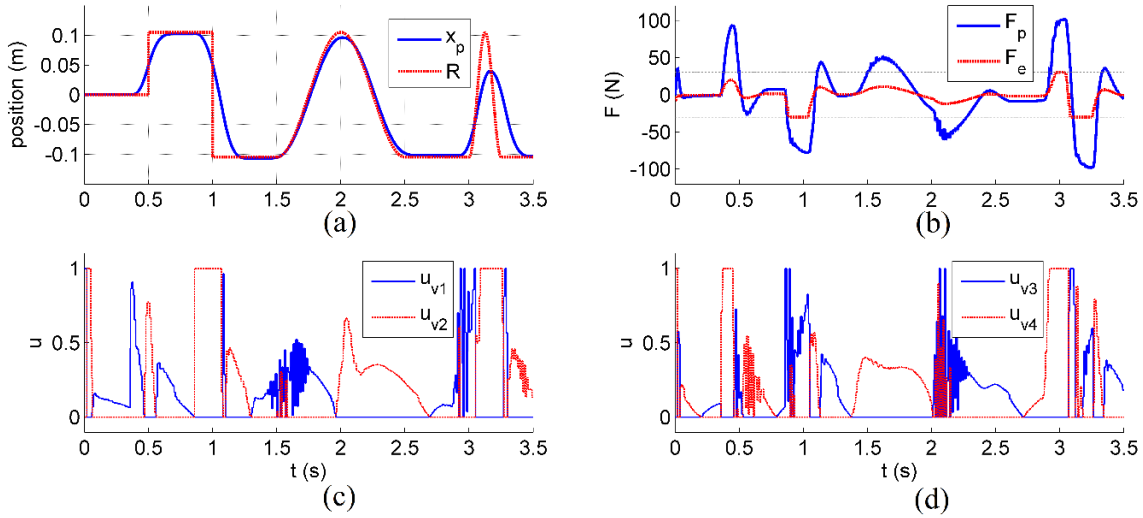

Figure 4.5 Position tracking and force allocation performance using MPC2: (**a**) position tracking, (**b**) actuator forces, (**c**) command to the valves controlling chamber A, and (**d**) command to the valves controlling chamber B.

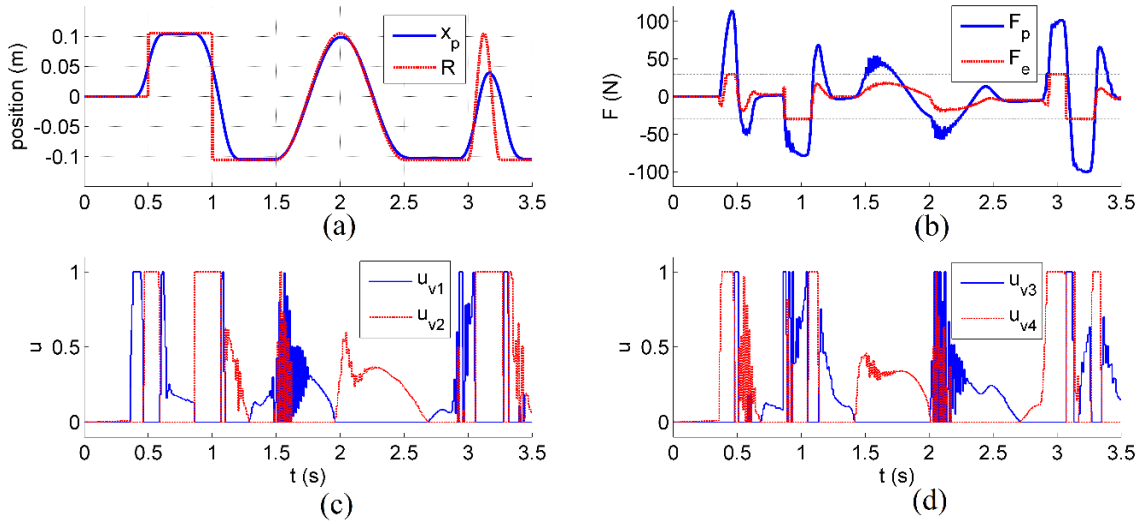

Figure 4.6 Position tracking and force allocation performance using MPC3: (**a**) position tracking, (**b**) actuator forces, (**c**) command to the valves controlling chamber A, and (**d**) command to the valves controlling chamber B.

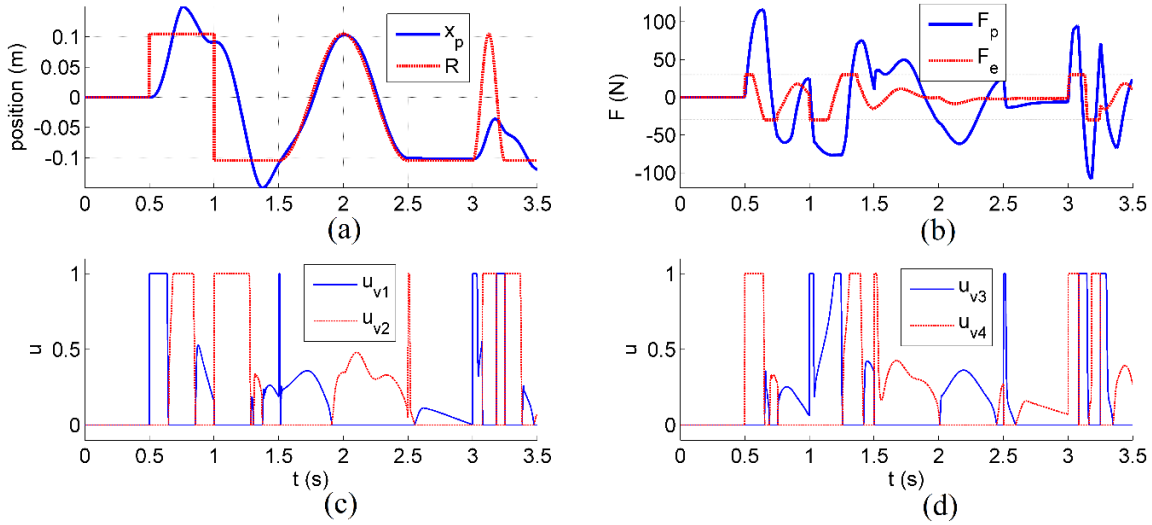

Figure 4.7 Position tracking and force allocation performance using the linear controller: (**a**) position tracking, (**b**) actuator forces, (**c**) command to the valves controlling chamber A, and (**d**) command to the valves controlling chamber B.

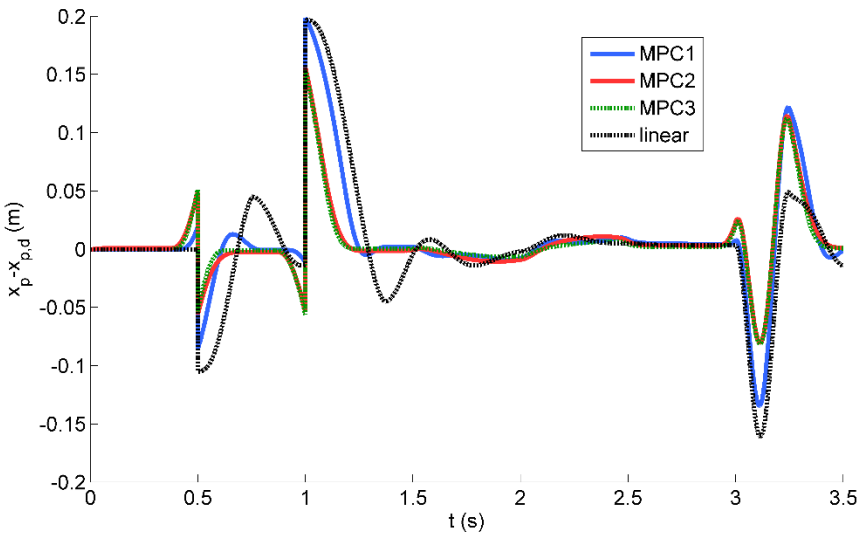

Figure 4.8 Comparison of the position tracking errors with the four control laws.

From Figures 4.4–4.8, it can be seen that the linear controller has a longer settling time, bigger overshoot, and larger error peaks when subjected to the faster trajectories, such as 4 Hz. However, all MPC-based controllers undergo chattering in the actuator force at some points, while the linear controller produces the smoothest input force and valve commands, which may lead to longer valve and actuator lives in practice. Between the MPC-based controllers, MPC3 produced the most accurate position tracking. A quantitative comparison is presented in Table 4.2. Although the linear controller has the lowest accuracy of the three, it has a much faster calculation time. MPC1 requires the highest calculation time which is undesirable for real-time operation. MPC3 yields the best tracking performance with RMSE reduction of 46%, 20%, and 55% compared to MPC1, MPC2, and the linear controller, respectively. MPC3 also reduced the mean absolute electric actuator force by 9%, and the mean absolute pneumatic actuator force by 14% relative to the benchmark linear controller. These force reductions have the benefits of reducing the energy consumption and operating cost.

Table 4.2 Numerical comparison of the controller results.

Parameter	Value			
	MPC1	**MPC2**	**MPC3**	**Linear**
Sampling period (T_s)	10 ms	10 ms	10 ms	1 ms
Position tracking RMSE	44.7 mm	29.9 mm	23.9 mm	53.0 mm
Mean Absolute F_p	29.73 N	28.11 N	28.81 N	33.58 N
Mean Absolute F_e	11.74 N	7.78 N	11.12 N	12.24 N
Average calculation time per sample	4.5 ms	3.9 ms	4.3 ms	0.003 ms
Maximum calculation time per sample	8.5 ms	6.4 ms	7.2 ms	0.02 ms

4.5 Conclusion

In this paper, three novel control algorithms for the position control of an HPEA-driven system are investigated. The first (MPC1) uses MPC with a linearized full plant model. The second (MPC2) uses an outer-loop MPC with an inner-loop PI pressure controller with a simplified linear model. The third (MPC3) uses the same structure as MPC2 with a modified model to find a balance in the trade-off between the position controller performance and computation time. A fourth controller, employed as a benchmark, uses an outer-loop PD plus feedforward controller with an inner-loop PI pressure controller. MPC2 showed the best performance in reducing the input forces (and thus, the energy consumption and operating cost). However, modifying the model in MPC3 leads to the best position tracking performance. Although MPC2 and MPC3 are computationally intensive, they can still be run in real-time using commonly available off-the-shelf hardware.

This research will be continued by investigating the extension of the MPC-based position control and task allocation approaches to rotary HPEA actuators with nonlinear payload dynamics. To avoid the subjectivity of the manual tuning approach, we will also be investigating the application of global optimization strategies (such as particle swarm optimization) to obtain the controller parameters.

Author Contributions: Conceptualization, B.R. and G.M.B.; methodology software and validation, B.R.; writing—original draft preparation, B.R.; writing—review and editing,

G.M.B.; supervision and funding acquisition, G.M.B.; All authors have read and agreed to the published version of the manuscript.

Funding: This research was supported by the Natural Sciences and Engineering Research Council of Canada (NSERC) through a Discovery Grant.

Conflicts of Interest: The authors declare no conflict of interest. The funders had no role in the design of the study; in the collection, analyses, or interpretation of data; in the writing of the manuscript, or in the decision to publish the results.

Appendix A. Matrices for the State Space Models Used in MPC1, MPC2, and MPC3

The matrices for the discrete-time state space model used in MPC1 are as follows:

$$\mathbf{A}_d = \mathbf{I} + T_s \begin{bmatrix} a_{11} & 0 & a_{13} & a_{14} \\ 0 & a_{22} & a_{23} & a_{24} \\ 0 & 0 & 0 & 1 \\ a_{41} & a_{42} & 0 & a_{44} \end{bmatrix} \tag{4.A1}$$

$$a_{11} = \frac{\dot{x}_{p_{op}}}{L_S/2 + L_{DV} + x_{p_{op}}} + \frac{RT}{A_A\left(L_S/2 + L_{DV} + x_{p_{op}}\right)} \times \cdots$$

where

$$\left(\frac{C_1 C_f \lambda_9}{\sqrt{T}} - \frac{C_2 C_f \lambda_9 \sqrt{1-\Lambda_A}}{K \Lambda_A \sqrt{T}} + \frac{C_2 C_f \lambda_9 (K\text{-}1)}{2K\sqrt{T(1-\Lambda_A)}} \right),$$

$$a_{13} = \frac{A_A P_{A_{op}} \dot{x}_{p_{op}} + \dfrac{RTC_f \lambda_9 \left(C_1 P_{A_{op}} - C_2 P_s \sqrt{1-\Lambda_A} \left(\dfrac{P_{A_{op}}}{P_s} \right)^{1/K} \right)}{\sqrt{T}}}{A_A \left(L_S/2 + L_{DV} + x_{p_{op}} \right)^2},$$

$$a_{14} = -\frac{P_{A_{op}}}{L_S/2 + L_{DV} + x_{p_{op}}},$$

$$a_{22} = \frac{\dot{x}_{p_{op}}}{L_S/2 + L_{DV} - x_{p_{op}}} + \frac{RT}{A_B\left(L_S/2 + L_{DV} - x_{p_{op}}\right)} \times \cdots$$

$$\left(\frac{C_1 C_f \lambda_9}{\sqrt{T}} - \frac{C_2 C_f \lambda_9 \sqrt{1-\Lambda_B}}{K \Lambda_B \sqrt{T}} + \frac{C_2 C_f \lambda_9 (K-1)}{2K\sqrt{T(1-\Lambda_B)}} \right),$$

$$a_{23} = \frac{A_B P_{B_{op}} \dot{x}_{p_{op}} - \dfrac{RTC_f \lambda_9 \left(C_1 P_{B_{op}} - C_2 P_s \sqrt{1-\Lambda_A} \left(\dfrac{P_{B_{op}}}{P_s} \right)^{1/K} \right)}{\sqrt{T}}}{A_B\left(L_S/2 + L_{DV} - x_{p_{op}}\right)^2},$$

$$a_{24} = \frac{P_{B_{op}}}{L_S/2 + L_{DV} - x_{p_{op}}},\ a_{41} = \frac{A_A}{\hat{m}_L},\ a_{42} = -\frac{A_B}{\hat{m}_L},\ a_{44} = -\frac{\hat{C}_v}{\hat{m}_L},\ \Lambda_A = \left(\frac{P_{A_{op}}}{P_s} \right)^{K-1/K} \text{ and}$$

$$\Lambda_B = \left(\frac{P_{B_{op}}}{P_s} \right)^{K-1/K}.$$

$$\mathbf{B_d} = T_s \begin{bmatrix} b_{11} & b_{12} & 0 & 0 & 0 \\ 0 & 0 & b_{23} & b_{24} & 0 \\ 0 & 0 & 0 & 0 & 0 \\ 0 & 0 & 0 & 0 & b_{45} \end{bmatrix} \tag{4.A2}$$

where $b_{11} = \dfrac{C_2 C_f R \lambda_8 P_s \sqrt{T} \sqrt{1-\Lambda_A} \left(\dfrac{P_{A_{op}}}{P_s} \right)^{1/K}}{A_A\left(L_S/2 + L_{DV} + x_{p_{op}}\right)}$, $b_{12} = -\dfrac{C_1 C_f R \lambda_8 P_{A_{op}} \sqrt{T}}{A_A\left(L_S/2 + L_{DV} + x_{p_{op}}\right)}$,

$b_{23} = \dfrac{C_2 C_f R \lambda_8 P_s \sqrt{T} \sqrt{1-\Lambda_B} \left(\dfrac{P_{B_{op}}}{P_s} \right)^{1/K}}{A_B\left(L_S/2 - L_{DV} + x_{p_{op}}\right)}$, $b_{24} = -\dfrac{C_1 C_f R \lambda_8 P_{B_{op}} \sqrt{T}}{A_B\left(L_S/2 + L_{DV} - x_{p_{op}}\right)}$, and $b_{45} = \dfrac{1}{\hat{m}_L}$

.

$$\mathbf{C}_d = \begin{bmatrix} 0 & 0 & 1 & 0 \\ 0.5 & 0.5 & 0 & 0 \end{bmatrix} \tag{4.A3}$$

For MPC2, the discrete-time state space matrices are as follows:

$$\mathbf{A}_d = \mathbf{I} + T_s \begin{bmatrix} 0 & 1 \\ 0 & -\hat{C}_v / \hat{m}_L \end{bmatrix} \tag{4.A4}$$

$$\mathbf{B}_d = T_s \begin{bmatrix} 0 & 0 \\ 1/\hat{m}_L & 1/\hat{m}_L \end{bmatrix} \tag{4.A5}$$

$$\mathbf{C}_d = \begin{bmatrix} 1 & 0 \end{bmatrix} \tag{4.A6}$$

Finally, the discrete-time state space matrices used in MPC3 are as follows:

$$\mathbf{A}_d = \mathbf{I} + T_s \begin{bmatrix} 0 & 1 & 0 \\ 0 & -\hat{C}_v / \hat{m}_L & 1/\hat{m}_L \\ 0 & 0 & -\kappa \end{bmatrix} \tag{4.A7}$$

$$\mathbf{B}_d = T_s \begin{bmatrix} 0 & 0 \\ 0 & 1/\hat{m}_L \\ \kappa & 0 \end{bmatrix} \tag{4.A8}$$

$$\mathbf{C}_d = \begin{bmatrix} 1 & 0 & 0 \end{bmatrix} \tag{4.A9}$$

References

1. ISO/TS 15066:2016. *Robots and Robotic Devices-Collaborative Robots*; International Organization for Standardization: Geneva, Switzerland, 2016.
2. Shin, D.; Sardellitti, I.; Khatib, O. A hybrid actuation approach for human-friendly robot design. In Proceedings of the 2008 IEEE International Conference on Robotics and Automation, Pasadena, CA, USA, 19–23 May 2008; pp. 1747–1752.

3. Rouzbeh, B.; Bone, G.; Ashby, G.; Li, E. Design, Implementation and Control of an Improved Hybrid Pneumatic-Electric Actuator for Robot Arms. *IEEE Access* **2019**, *7*, 14699–14713, doi:10.1109/access.2019.2891532.
4. Petrosky, L.J. Hybrid Electro-Pneumatic Robot Joint Actuator. U.S. Patent 478 225 828, November 1, 1988.
5. Takemura, F.; Pandian, S.R.; Nagase, Y.; Mizutani, H.; Hayakawa, Y.; Kawamura, S. Control of a hybrid pneumatic/electric motor. In Proceedings of the 2000 IEEE/RSJ International Conference on Intelligent Robots and Systems (IROS 2000) (Cat No 00CH37113) IROS-00, Takamatsu, Japan, 31 October–5 November 2002; Volume 1, pp. 209–214.
6. Teramae, T.; Noda, T.; Hyon, S.-H.; Morimoto, J.; Noda, T. Modeling and control of a Pneumatic-Electric hybrid system. In Proceedings of the 2013 IEEE/RSJ International Conference on Intelligent Robots and Systems, Tokyo, Japan, 3–7 November 2013; Volume 4, pp. 4887–4892.
7. Ishihara, K.; Morimoto, J. An optimal control strategy for hybrid actuator systems: Application to an artificial muscle with electric motor assist. *Neural Netw.* **2018**, *99*, 92–100, doi:10.1016/j.neunet.2017.12.010.
8. Sharbafi, M.A.; Shin, H.; Zhao, G.; Hosoda, K.; Seyfarth, A. Electric-Pneumatic Actuator: A New Muscle for Locomotion. *Actuators* **2017**, *6*, 30, doi:10.3390/act6040030.
9. Bone, G.; Chen, X. Position control of hybrid pneumatic-electric actuators. In Proceedings of the 2012 American Control Conference (ACC), Montreal, QC, Canada, 27–29 June 2012; pp. 1793–1799.
10. Bone, G.; Xue, M.; Flett, J. Position control of hybrid pneumatic–electric actuators using discrete-valued model-predictive control. *Mechatronics* **2015**, *25*, 1–10, doi:10.1016/j.mechatronics.2014.10.009.
11. Nakata, Y.; Noda, T.; Morimoto, J.; Ishiguro, H. Development of a pneumatic-electromagnetic hybrid linear actuator with an integrated structure. In Proceedings of

the 2015 IEEE/RSJ International Conference on Intelligent Robots and Systems (IROS), Hamburg, Germany, 28 September–2 October 2015; pp. 6238–6243.

12. Mori, S.; Tanaka, K.; Nishikawa, S.; Niiyama, R.; Kuniyoshi, Y. High-Speed Humanoid Robot Arm for Badminton Using Pneumatic-Electric Hybrid Actuators. *IEEE Robot. Autom. Lett.* **2019**, *4*, 3601–3608, doi:10.1109/lra.2019.2928778.
13. Johansen, T.A.; Fossen, T.I. Control allocation-A survey. *Automatica* **2013**, *49*, 1087–1103.
14. Härkegård, O. Dynamic Control Allocation Using Constrained Quadratic Programming. *J. Guid. Control. Dyn.* **2004**, *27*, 1028–1034.
15. Galeani, S.; Pettinari, S. On dynamic input allocation for fat plants subject to multi-sinusoidal exogenous inputs. In Proceedings of the 53rd IEEE Conference on Decision and Control, Los Angeles, CA, USA, 15–17 December 2014; pp. 2396–2403.
16. Lofberg, J. YALMIP: A toolbox for modeling and optimization in MATLAB. In Proceedings of the 2004 IEEE International Conference on Robotics and Automation (IEEE Cat No 04CH37508) CACSD-04, New Orleans, LA, USA, 2–4 Septemaber 2005; pp. 284–289.
17. Mattingley, J.; Boyd, S. CVXGEN: a code generator for embedded convex optimization. *Optim. Eng.* **2011**, *13*, 1–27, doi:10.1007/s11081-011-9176-9.
18. Hanger, M.; Johansen, T.A.; Mykland, G.K.; Skullestad, A. Dynamic model predictive control allocation using CVXGEN. In Proceedings of the 2011 9th IEEE International Conference on Control and Automation (ICCA), Santiago, Chile, 19–21 December 2011; pp. 417–422.
19. Ning, S.; Bone, G. Development of a nonlinear dynamic model for a servo pneumatic positioning system. In Proceedings of the IEEE International Conference Mechatronics and Automation, Niagara Falls, ON, Canada, 29 July–1 August 2005; pp. 43–48.
20. Taheri, B.; Case, D.; Richer, E. Force and Stiffness Backstepping-Sliding Mode Controller for Pneumatic Cylinders. *IEEE/ASME Trans. Mechatronics* **2014**, *19*, 1799–1809, doi:10.1109/tmech.2013.2294970.

21. Richer, E.; Hurmuzlu, Y. A High Performance Pneumatic Force Actuator System: Part I—Nonlinear Mathematical Model. *J. Dyn. Syst. Meas. Control.* **1999**, *122*, 416–425, doi:10.1115/1.1286336.

Chapter 5. Implementation of a Two-Degree-of-Freedom Hybrid Pneumatic-Electric Actuator Driven Arm

5.1 Introduction

In Chapter 3, we designed and controlled a HPEA-driven rotary joint [44][43]. The joint was used with a 1-DOF arm so only simple kinematic and kinetic relations were needed. In this chapter, the goal is to design and add a HPEA-driven joint to the existing 1-DOF HPEA-driven arm. The resulting prototype will be a 2-DOF planar arm with two revolute joints known as the "shoulder" and the "elbow" joints. This prototype will be designed to maintain the performance and safety advantages of the original HPEA-driven arm.

A multi-DOF manipulator can handle wider range of tasks in a larger workspace compared to a 1-DOF prototype. It can also provide a testbed for evaluating position controllers in more challenging situations. However, the kinetic and kinematic couplings between the joints require more complicated modeling and control approaches. Several new issues also need to be addressed, e.g., end-effector Cartesian path planning, inverse kinematics with multiple solutions, joint-space singularities, achievable workspace, error propagation, etc.

Although several papers have studied the design and implementation of HPEA-driven arms with different configurations, and in [46] they even optimized their HPEA design for higher bandwidth and lower mechanical impedance, they have not tested their approach on multi-DOF prototypes. Thus, a study on the motion of the coupled joints in a completely HPEA-driven system has not been performed to date.

5.2 Elbow Joint structure

The goal of this chapter is to add an elbow joint to the existing HPEA-driven shoulder joint [44]. HPEAs are favoured for their ability to provide high actuator performance (in terms of accuracy and response time) that can be compared to electrical actuators, while being more compliant and inherently safe. The added joint should be able to demonstrate these advantages in a cost-efficient configuration.

There can be several options for the actuator and the transmission structure. The actuator power can be transmitted to the elbow joint using a cable/belt and pulley as in [47]. In this case, the main HPEA components can placed on the stationary base of the arm which leads to reduction in the mass of the arm. This is beneficial if the ultimate design goal is reducing the mass. This approach can undermine the joint performance by adding transmission errors (if the belt is under-tensioned), or additional friction (if the belt is over-tensioned). However, using this type of transmission adds to the complexity of the design (since a tensioning mechanism is needed) and its maintenance requirements and reduces its reliability in providing consistent performance. Furthermore, our safety design goal is to make human-robot collisions safe. Impacts with collaborative arms are most probable near their end-effectors (where they interact with people) not near their joints, so it is more beneficial to focus on reducing the overall mechanical impedance of the joint with help of compliant HPEAs rather than merely minimizing the mass and sacrificing the performance. Finally, soft covers can be used on the joints to mitigate any impact with them, which has been proved to be highly effective in [33].

There have been several actuator types used within HPEAs in literature. They include combining a DC motor in parallel with pneumatic actuators in form of either a rotary pneumatic motor [20], or pneumatic muscle actuators (PMAs) [21][41][42][48], or pneumatic cylinders [10][11], or even a pneumatic cylinder integrated within a linear motor[22][49]. Using rotary pneumatic motors or integrated hybrid actuators adds to the mechanical complexity of the design and the actuator cost. On the other hand, PMAs suffer from an inconsistent and highly nonlinear force-displacement relationship, and hysteresis.

A combination of linear pneumatic cylinders and a DC motor can provide a simple cost-efficient actuator with enough power, as has been proven with the existing shoulder joint. The linear cylinder's motion needs to be converted to the rotary motion. Figure 5.1 shows the selected HPEA-driven joint structure. The electric motor is directly coupled to the joint shaft without any gears or other transmissions. This eliminates gear backlash and substantially lower mechanical impedance at the joint's output shaft (since a gearbox with the reduction ratio of n will amplify mechanical output impedance by n^2). The pneumatic

cylinder is directly connected to the robot links with an excavator-like, 4-bar linkage design. Unlike the stationary shoulder joint that used four symmetrically distributed cylinders, the mobile elbow joint uses one cylinder to keep the design simple with fewer mechanical parts. The geometry of this linkage and the nonlinear relation between the cylinder stroke and the joint position are some key factors in this design. The acceptable elbow joint angle range from this design was chosen to be $-100° \leq \theta_2 \leq -5°$.

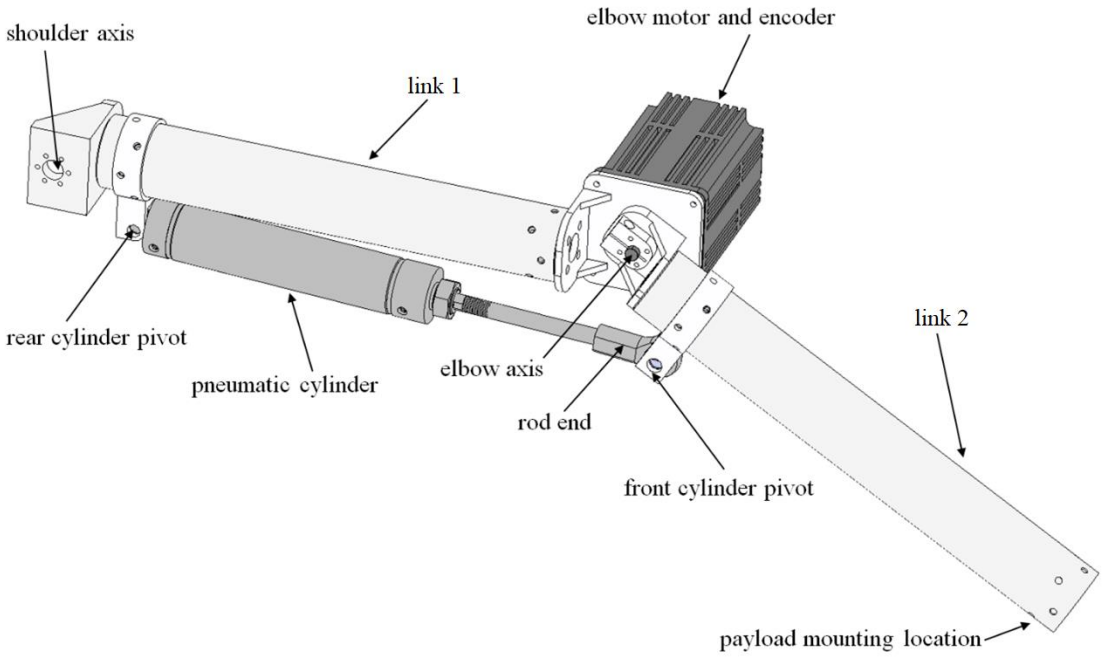

Figure 5.1 Structure of the new elbow joint included in the two-DOF HPEA-driven arm.

5.3 Manipulator Model

The manipulator needs to be mathematically modeled in order to predict its performance and use model-based position controllers. The manipulator kinematic and kinetic models, as well as the geometry of the added elbow joint, are presented in this section.

5.3.1 Kinematic Model

A kinematic model of the links and joints is needed to formulate the arm motion. According to the kinematic diagram of a standard RR planar arm in Figure 5.2, the Jacobian matrix in the fixed reference frame XYZ is [50]:

$$\boldsymbol{J} = \begin{bmatrix} -l_1 s_1 - l_2 s_{12} & -l_2 s_{12} \\ l_1 c_1 + l_2 c_{12} & l_2 c_{12} \end{bmatrix} \tag{5.1}$$

Note that in (5.1), and elsewhere in this thesis, the following abbreviated names for trigonometric functions are used: $s_1 = \sin(\theta_1)$, $c_1 = \cos(\theta_1)$, $s_2 = \sin(\theta_2)$, $c_2 = \cos(\theta_2)$, $s_{12} = \sin(\theta_1 + \theta_2)$, and $c_{12} = \cos(\theta_1 + \theta_2)$.

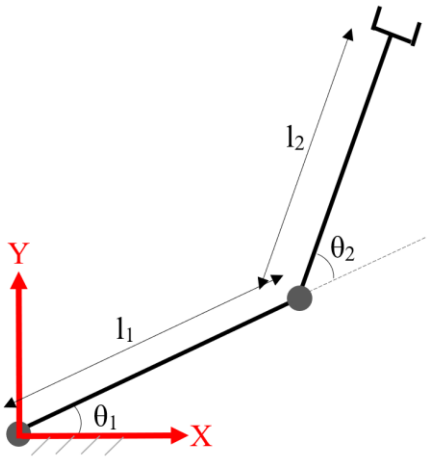

Figure 5.2 Schematic of the RR planar arm considering only the links and the joints.

The end-effector velocity and the joint velocities can be related using the Jacobian matrix as shown in (5.2) and (5.3).

$$\vec{\boldsymbol{v}}_{EE} = \boldsymbol{J}\begin{bmatrix}\dot{\theta}_1\\ \dot{\theta}_2\end{bmatrix} = \begin{bmatrix}-l_1 s_1 - l_2 s_{12} & -l_2 s_{12}\\ l_1 c_1 + l_2 c_{12} & l_2 c_{12}\end{bmatrix}\begin{bmatrix}\dot{\theta}_1\\ \dot{\theta}_2\end{bmatrix} \tag{5.2}$$

$$\begin{bmatrix}\dot{\theta}_1\\ \dot{\theta}_2\end{bmatrix} = \boldsymbol{J}^{-1}\vec{\boldsymbol{v}}_{EE} = \frac{v_{EE}}{l_1 l_2 s_2}\begin{bmatrix}l_2 c_{12} & l_2 s_{12}\\ -l_1 c_1 - l_2 c_{12} & -l_1 s_1 - l_2 s_{12}\end{bmatrix}\begin{bmatrix}cos\theta_{EE}\\ sin\theta_{EE}\end{bmatrix} \tag{5.3}$$

Here, $\vec{\boldsymbol{v}}_{EE}$ and θ_{EE} indicate the end-effector velocity vector and the angle this vector makes with the X axis, respectively. v_{EE} indicates the Euclidean norm of $\vec{\boldsymbol{v}}_{EE}$. It should be noted that when a person is inside the robot's workspace the highest allowed end-effector speed from the international safety standard for collaborative robots [51] is 0.25 m/s.

Equation (5.4) defines the end-effector position from the joint angles, which is known as the forward kinematics of the arm.

$$\begin{bmatrix}X_{EE}\\ Y_{EE}\end{bmatrix} = \begin{bmatrix}l_1 c_1 + l_2 c_{12}\\ l_1 s_1 + l_2 s_{12}\end{bmatrix} \tag{5.4}$$

The inverse relation, known as inverse kinematics of the arm, is defined using (5.5)- (5.7) [50]. In these equations $Atan2(.)$ denotes the two-argument arctangent. It must be noted that there are two solutions for the inverse kinematics of the arm, known as elbow-up and elbow-down solution. Here, the only elbow-up solution is used due to the elbow's angle range.

$$c_2 = \frac{{X_{EE}}^2 + {Y_{EE}}^2 - {l_1}^2 - {l_2}^2}{2 l_1 l_2} \tag{5.5}$$

$$\theta_2 = Atan2\left(-\sqrt{1 - {c_2}^2}\,, c_2\right) \tag{5.6}$$

$$\theta_1 = Atan2(Y_{EE}, X_{EE}) - Atan2(l_2 s_2, l_1 + l_2 c_2) \quad (5.7)$$

5.3.2 Kinetic Model

The inertia of the point masses at the end of the links are dominant compared to the inertia from the other moving parts (such as the links, mechanical connectors and bearings, the wires and the elbow cylinder). Hence, to keep the model-based controllers computationally efficient, a standard lumped-mass kinetic model of the arm has been employed. The schematic representation of such a model is shown in figure 5.3.

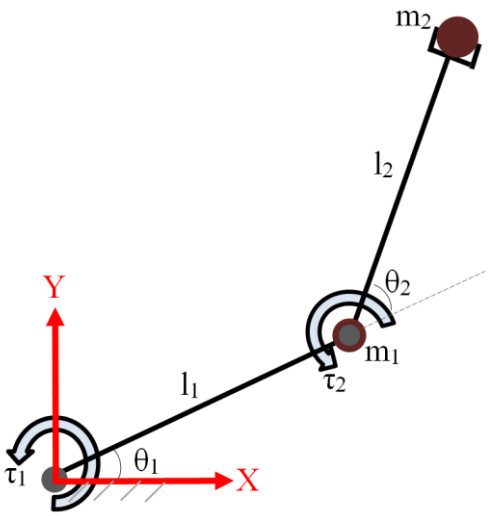

Figure 5.3 Schematic of a RR planar arm with lumped masses

The kinetic model for the lumped-mass arm model shown in Figure 5.4 is given by (5.8)-(5.11) [50].

$$\begin{bmatrix}\tau_1 \\ \tau_2\end{bmatrix} = \boldsymbol{M}\begin{bmatrix}\ddot{\theta}_1 \\ \ddot{\theta}_2\end{bmatrix} + \boldsymbol{V} + \boldsymbol{G} \quad (5.8)$$

$$\boldsymbol{M} = \begin{bmatrix} (m_1 + m_2){l_1}^2 + m_2{l_2}^2 + 2m_2 l_1 l_2 c_2 & m_2{l_2}^2 + m_2 l_1 l_2 c_2 \\ m_2{l_2}^2 + m_2 l_1 l_2 c_2 & m_2{l_2}^2 \end{bmatrix} \tag{5.9}$$

$$\boldsymbol{V} = \begin{bmatrix} -m_2 l_1 l_2 \dot{\theta}_2 (2\dot{\theta}_1 + \dot{\theta}_2) s_2 \\ m_2 l_1 l_2 {\dot{\theta}_1}^2 s_2 \end{bmatrix} \tag{5.10}$$

$$\boldsymbol{G} = \begin{bmatrix} (m_1 + m_2) g l_1 c_1 + m_2 g l_2 c_{12} \\ m_2 l_2 g c_{12} \end{bmatrix} \tag{5.11}$$

In (5.8), τ_1 and τ_2 are the torques at each joint shaft. They can be modelled as follows:

$$\tau_1 = \tau_{p1} + \tau_{m1} - \tau_{f1} - I_{out1}\ddot{\theta}_1 \tag{5.12}$$

$$\tau_2 = \tau_{p2} + \tau_{m2} - \tau_{f2} - I_{out2}\ddot{\theta}_2 \tag{5.13}$$

Here, τ_p , τ_m , τ_f, and I_{out} are the torque from the pneumatic actuator, the torque from the electric actuator, the friction torque and the equivalent actuator inertia at the output shaft for each joint.

For the elbow joint, the pneumatic cylinder force (F_{cyl}) is calculated using (5.14). In this equation, P_1, P_2, P_{atm}, A_1, and A_2 are the pressure in the rod-less side of the piston, the pressure on the rodded side of the piston, the atmospheric pressure, the surface area of the rod-less side of the piston, and the surface area of the rodded side of the piston, respectively.

$$F_{cyl} = (\mathrm{P}_1 - P_{atm})A_1 - (\mathrm{P}_2 - P_{atm})A_2 \tag{5.14}$$

5.3.3 Geometric Study of the Elbow Joint

In this section, the geometry of the elbow joint including its pneumatic cylinder is studied. Figure 5.4 shows the geometry of this joint and the parameters used to formulate the geometry. The positions of the cylinder pivots are key parameters that have a strong influence on the kinematics and dynamics of the elbow joint. The parameters a_1, r_1, a_2, and r_2 define the position of the pivots by providing the axial and radial offsets with respect to the joints.

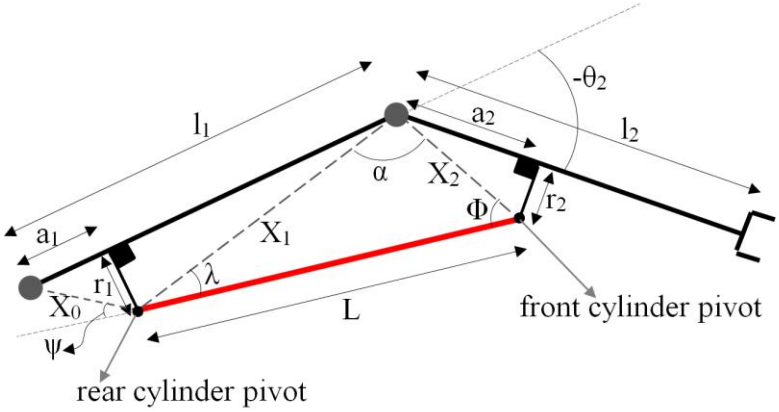

Figure 5.4 Geometry of the elbow joint and the elbow cylinder pivots.

The following equations relate the cylinder pivots' offsets with the other geometric parameters and the arm configuration.

$$\alpha = \pi + \theta_2 - \tan^{-1}\left(\frac{r_1}{l_1 - a_1}\right) - \tan^{-1}\left(\frac{r_2}{a_2}\right) \tag{5.15}$$

$$X_1 = \sqrt{(l_1 - a_1)^2 + r_1^2} \tag{5.16}$$

$$X_2 = \sqrt{{a_2}^2 + r_2^2} \tag{5.17}$$

$$L = \sqrt{{X_1}^2 + {X_2}^2 - 2X_1X_2cos\alpha} \tag{5.18}$$

$$\dot{L} = \frac{X_1X_2\dot{\theta}_2sin\alpha}{\sqrt{{X_1}^2 + {X_2}^2 - 2X_1X_2cos\alpha}} \tag{5.19}$$

Based on these geometric relationships, the pneumatic cylinder force in (5.14) can be related with the joint 2 torque it produces using (5.20).

$$\tau_{p2} = F_{cyl}X_2sin\Phi = \frac{F_{cyl}X_1X_2sin\alpha}{L} \tag{5.20}$$

Similarly, the chamber volumes at the two sides of the elbow cylinder's piston can be calculated at any arm configuration using (5.21) and (5.22). Knowing these volumes is a requirement with most model-based pressure controllers, including the one used in chapters 2 and 3, and this chapter.

$$V_{1,elbow} = \left(V_{1,elbow}\right)_0 + \mathrm{A}_1(L - L_0) \tag{5.21}$$

$$V_{2,elbow} = \left(V_{2,elbow}\right)_0 - \mathrm{A}_2(L - L_0) \tag{5.22}$$

In these equations, $V_{1,elbow}$ and $V_{2,elbow}$ are the chamber volumes for the rodless side of the piston, and the rodded side of the piston, respectively. $(V_{1,elbow})_0$, $(V_{2,elbow})_0$, and L_0 are the volumes and the pivot-to-pivot length (see 5.18) at $\theta_2 = 0°$.

5.4 Final Design and Fabrication

The 2-DOF arm's mechanical design was completed using Autodesk Inventor. The CAD model has been shown in Figure 5.1. The main dimensions are: $l_1 = l_2 = 0.4\,m$, $a_1 = 0.051\,m$, $r_1 = 0.050\,m$, $a_2 = 0.059\,m$ and $r_2 = 0.047\,m$. The manufactured and assembled arm is shown in Figure 5.5.

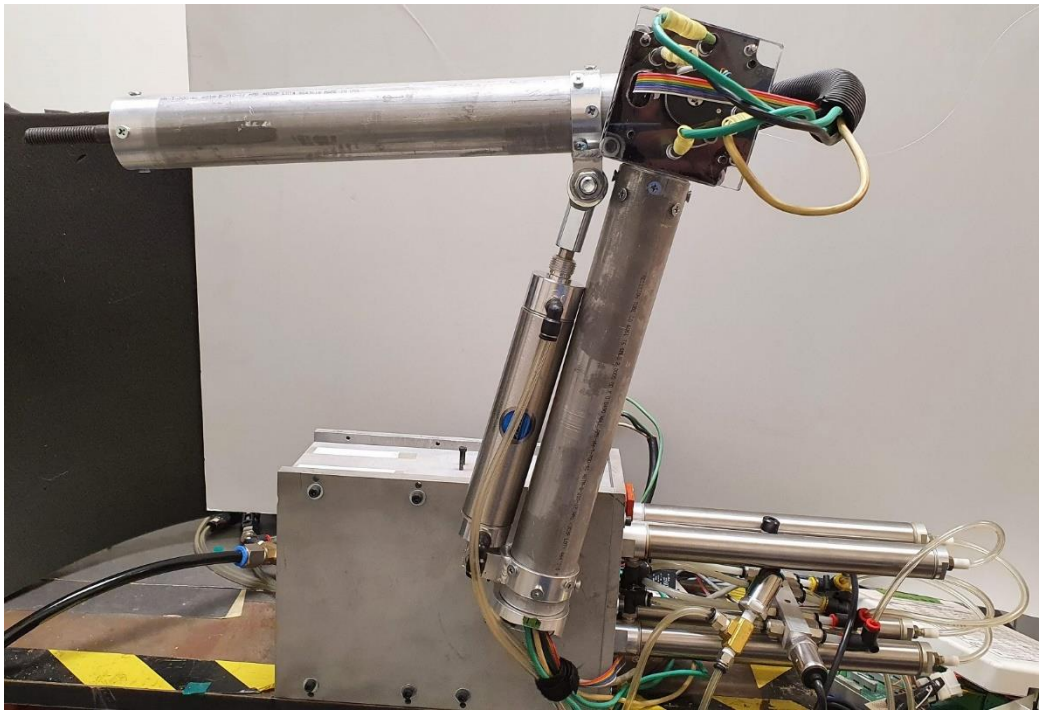

Figure 5.5 The HPEA-driven 2DOF robot arm prototype.

Figure 5.6 presents the instrumentation of the elbow joint actuator. A computer-based controller architecture with a DAQ interface is implemented to receive the sensors data, analyze them, and send commands to the pneumatic valves and the electric motor. The computer and DAQ are the same as those used in chapters 3 and 4. The chosen pneumatic cylinder has a 0.127 m stroke, 0.0381 m bore diameter and 0.0114 m rod diameter (Bimba, C-175-DXP). A pair of fast switching 2/2 solenoid valves (Festo, MHJ10-S-2,5-QS-1/4-MF-U) are used for each pneumatic chamber to control the charge/discharge flows. Two pressure sensors (SSI, P51-100) and an 80,000 count/rev incremental rotary encoder (Quantum Devices, QR12-20000) provide real-time feedback of the states. The elbow joint employs a brushless DC motor (Animatics, SM3430D, operating in current control mode).

The shoulder joint (not shown in the figure) uses a larger brushless motor (MTI Torque Systems, T0852J0001 with a built-in 20,000 count/rev encoder) to provide the torque required. It also uses two solenoid valves (Festo, MHJ10-S-2,5-QS-1/4-HF-U) and one pressure sensor (SSI, P51-100) for each of its two chambers. To attenuate the high frequency noise, the pressure sensor outputs were passed through a hardware RC low-pass filter with a 95 Hz cut off frequency.

The PWM period for the valves were chosen empirically as the smallest period at which the valves were responsive to the command duty cycle values within the 0.05 to 0.95 range (which is 90% of the total duty cycle range). Since the elbow joint uses valves with faster response time, a PWM period of 2 ms was used with its valves, while a PWM period of 4 ms was used with the slower responding valves on the shoulder joint.

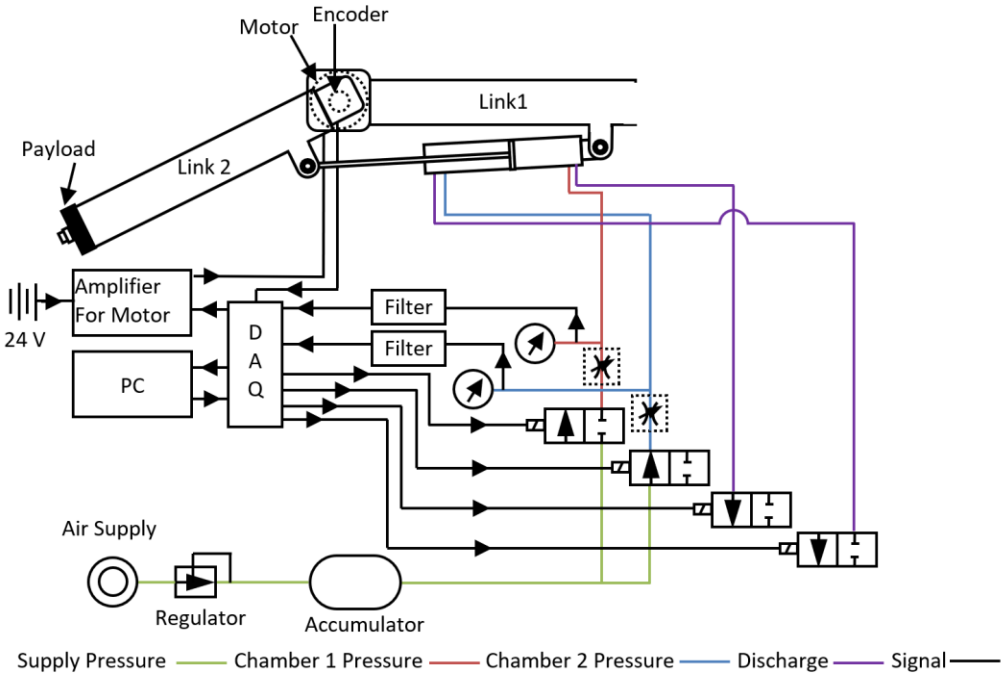

Figure 5.6 Schematic diagram of the elbow joint instrumentation indicating the hybrid actuator's mechanical, pneumatic, and electric components.

5.5 Preliminary Experimental Results

5.5.1 Elbow Joint Position Control

For the new elbow joint, a cascade control structure is implemented for the hybrid actuator with an inner-loop model-based pressure controller and an outer-loop position controller. This is the same structure that was used with the shoulder joint and presented in chapter 3. The more powerful pneumatic actuator compensates the modeled torque demands (through the controller's feedforward signal) while the weaker and higher-bandwidth electric actuator mitigates the remaining position tracking error. The HPEA-driven elbow is experimentally tested in pneumatic and hybrid modes. In the pneumatic mode the electric motor is disabled.

To test the new elbow joint independently, the shoulder joint is fixed at $\theta_1 = 0°$. Figure 5.7 shows the results from an experiment tracking a multi-cycloidal desired trajectory with a 1 Hz sine wave in the middle. Figure 5.8 presents the results from the experiment with a faster 2 Hz sine wave. The results clearly show that the errors during the transients are

much larger than at steady-state, that their amplitude increases dramatically when the frequency of the desired trajectory increases from 1 to 2 Hz. The plots also show that the addition of a relatively small motor torque in the hybrid mode causes the tracking errors to decrease dramatically.

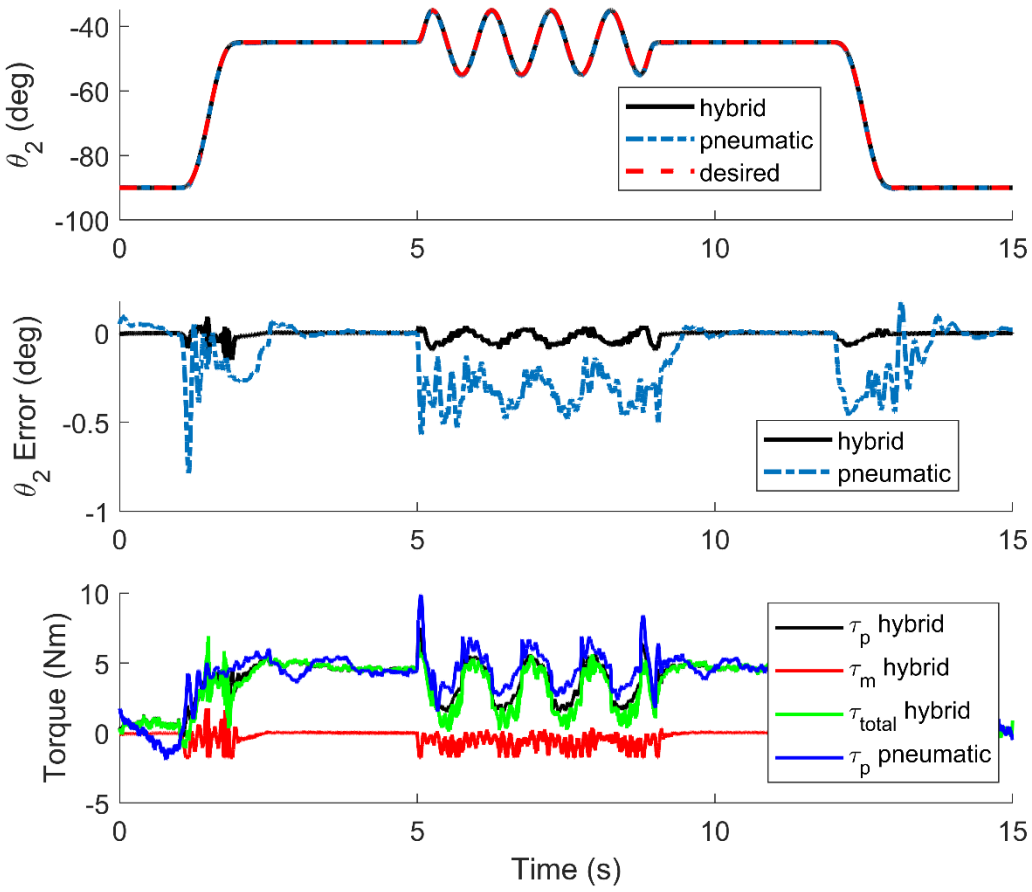

Figure 5.7 Experimental position tracking results for the elbow joint. The shoulder joint is fixed at $\theta_1 = 0$. The trajectory includes multi-cycloidal sections and a 1 Hz sine wave in the middle. A payload of 1.4 kg is attached to the end effector. The bottom plot shows the torque from the pneumatic actuator (τ_p) and the torque from the electric motor (τ_m) in pneumatic and hybrid modes.

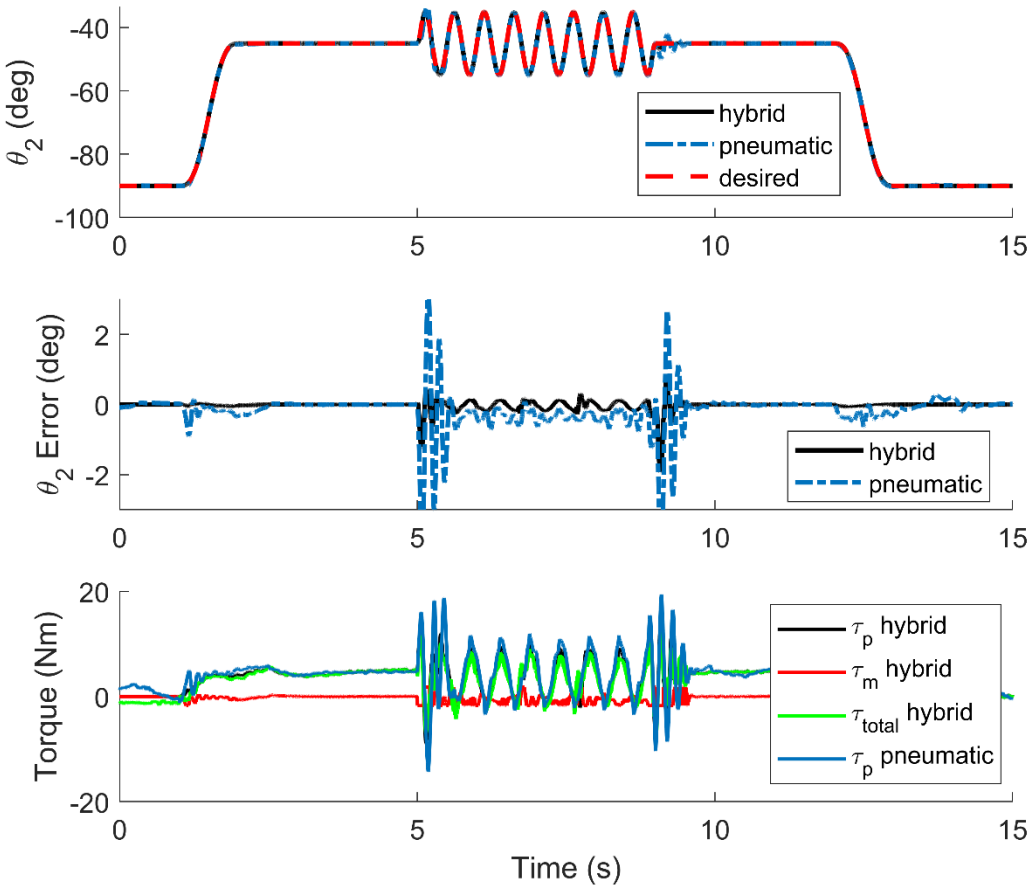

Figure 5.8 Experimental position tracking results for the elbow joint. The shoulder joint is fixed at $\theta_1 = 0$. The trajectory includes multi-cycloidal sections and a 2 Hz sine wave in the middle. A payload of 1.4 kg is attached to the end effector. The bottom plot shows the torque from the pneumatic actuator (τ_p) and the torque from the electric motor (τ_m) in pneumatic and hybrid modes.

Quantitative results from the elbow's position control tests are listed in Table 5.1. The hybrid actuator has achieved a root mean square error reduction of 75% and 72% compared to the pneumatic actuator for the 1 Hz and 2 Hz trajectories, respectively. The larger errors with the pneumatic mode are due to the model uncertainties and the pneumatic actuator's delay and torque inaccuracy. In both modes, the SSE of 0.0045˚ (which is equal to the encoder resolution) was achieved by including the adaptive friction compensator from

chapter 2. The actuator has also shown the ability to provide joint acceleration values up to 39 rad/s^2.

Table 5.1 Quantitative experimental results for the HPEA-driven elbow joint.

Parameter	1 Hz Trajectory	2 Hz Trajectory
RMSE in pneumatic mode	0.219˚	0.594˚
RMSE in hybrid mode	0.055˚	0.163˚
SSE in both modes	0.0045˚	0.0045˚
Maximum joint velocity in hybrid mode	1.65 rad/s	3.52 rad/s
Maximum joint acceleration in hybrid mode	18 rad/s^2	39 rad/s^2

5.5.2 Two-Degree-of-Freedom Arm Position Control

Position control of the 2-DOF arm is more challenging due to the kinematic and kinetic couplings between the joints and the error propagation at the end-effector. Due to the impact of COVID-19-related closures and limitations on preparing and conducting experimental tests, the two-DOF position control tests were limited to pneumatic mode only.

The kinetic coupling between the joints is included in the outer-loop position controller by replacing the 1-DOF model-based terms in (3.12) with terms based on (5.8)-(5.13). The PD feedback terms provide robustness as before. The desired torques for the two pneumatic actuators are then given by:

$$\begin{bmatrix}\tau_{p1,d}\\ \tau_{p2,d}\end{bmatrix} = \widehat{\boldsymbol{M}}\begin{bmatrix}\ddot{\theta}_{1,d}\\ \ddot{\theta}_{2,d}\end{bmatrix} + \widehat{\boldsymbol{V}} + \widehat{\boldsymbol{G}} + \begin{bmatrix}\boldsymbol{I}_{out1} & 0\\ 0 & \boldsymbol{I}_{out2}\end{bmatrix}\begin{bmatrix}\ddot{\theta}_{1,d}\\ \ddot{\theta}_{2,d}\end{bmatrix} + \begin{bmatrix}\tau_{f2}^{*}\\ \tau_{f2}^{*}\end{bmatrix} - \begin{bmatrix}K_{P1} & 0\\ 0 & K_{P2}\end{bmatrix}\begin{bmatrix}\hat{e}_{\theta 1}\\ \hat{e}_{\theta 2}\end{bmatrix} - \begin{bmatrix}K_{D1} & 0\\ 0 & K_{D2}\end{bmatrix}\begin{bmatrix}\hat{\dot{e}}_{\theta 1}\\ \hat{\dot{e}}_{\theta 2}\end{bmatrix} \tag{5.23}$$

where $\widehat{\boldsymbol{M}}$, $\widehat{\boldsymbol{V}}$ and $\widehat{\boldsymbol{G}}$ use the nominal values of the lumped masses, the sensed joint angles and the joint velocities that are obtained by backward differencing and low-pass filtering the sensed joint angles. A second-order Butterworth filter with 12.5 Hz cut off frequency was used for the experiments. The inner-loop pressure controllers use the same approach as (3.21)-(3.23).

Figure 5.9 shows the tracking performance of the two-DOF arm with the two joints following multi-cycloidal trajectories at the same time. A nominal payload of 1.4 kg is attached to the end-effector. The two joints track with RMSE of 0.52˚ and 0.39˚, respectively. Figure 5.10 illustrates position control results in more challenging conditions. The joints are tracking faster multi-cycloidal trajectories. To evaluate the robustness to payload changes, this experiment has been performed with three different payloads: the nominal payload (1.4 kg), heavier payload (1.9 kg), and lighter payload (0.65 kg). The results show that the manipulator joint can perform stable tracking with different payloads without changing any of the controller parameters.

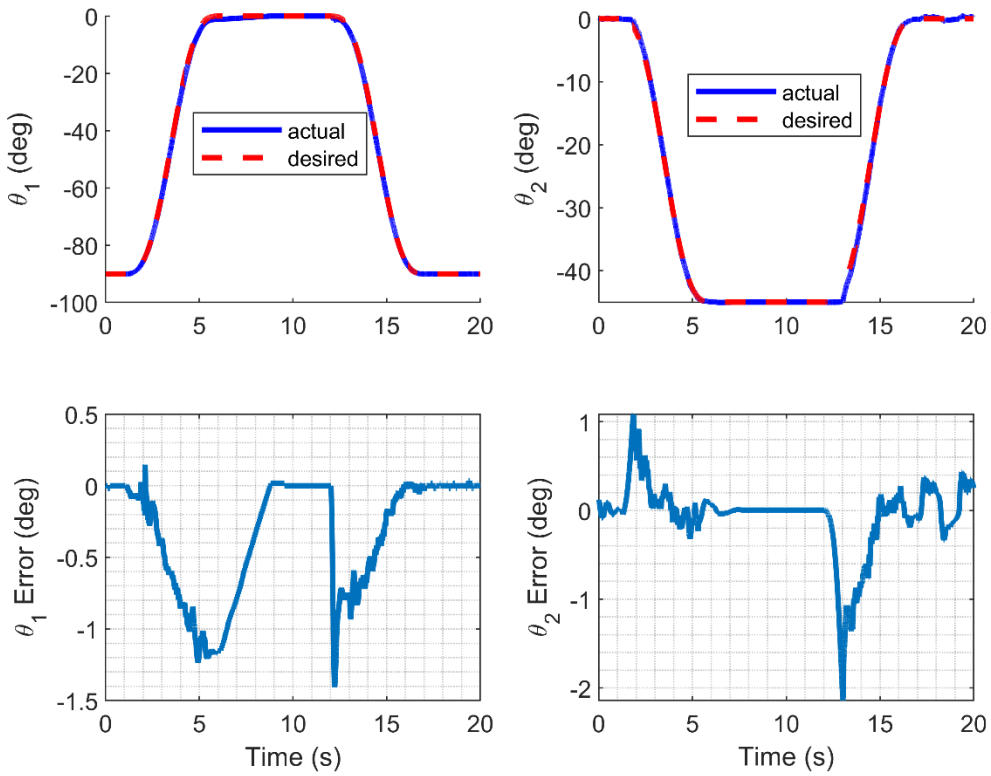

Figure 5.9 Two-DOF tracking results with multi-cycloidal trajectories and the 1.4 kg nominal payload.

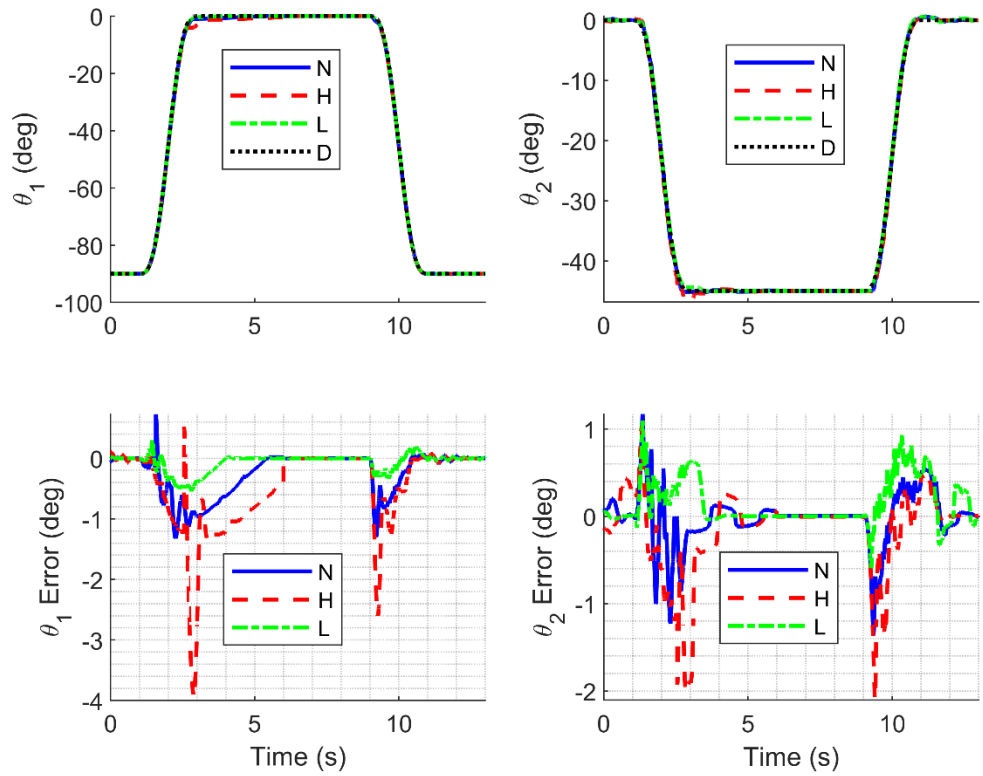

Figure 5.10 Two-DOF tracking results with faster multi-cycloidal trajectories. The figure illustrates the results for the nominal payload of 1.4 kg (N), a heavier payload of 1.9 kg (H), a lighter payload of 0.65 kg (L), and the desired trajectory (D).

In many applications, it is important for the manipulator's end-effector to be able to track a desired Cartesian trajectory, rather than the joints tracking independently. Inverse kinematics of the arm from (5.5)-(5.7) is employed to convert the Cartesian end-effector trajectory to the joint trajectories. Figure 5.10 shows the results when the end-effector is moved from the straight-down position (initial condition) to a specified position within the workspace and then follows a circular trajectory with a 0.05 m radius. The end-effector position error is the result of error at both joints, and remains mostly below 0.005 m.

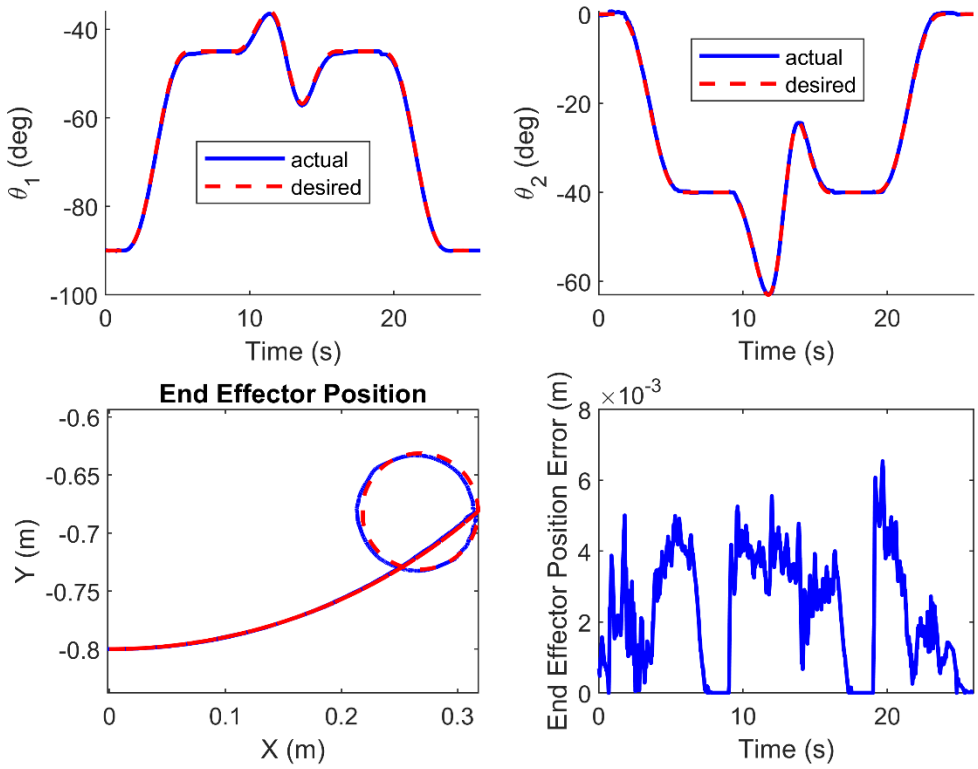

Figure 5.11 The joint and end-effector position tracking results with the end-effector following a circular path.

As a more challenging scenario, the end-effector is required to follow a circle placed higher within the workspace. This experiment requires the position to be tracked when the actuator torques are significantly higher since the links are closer to being horizontal. Figure 5.12 shows the results for this test. It can be seen that the end-effector distance error reaches 0.015 m at some points.

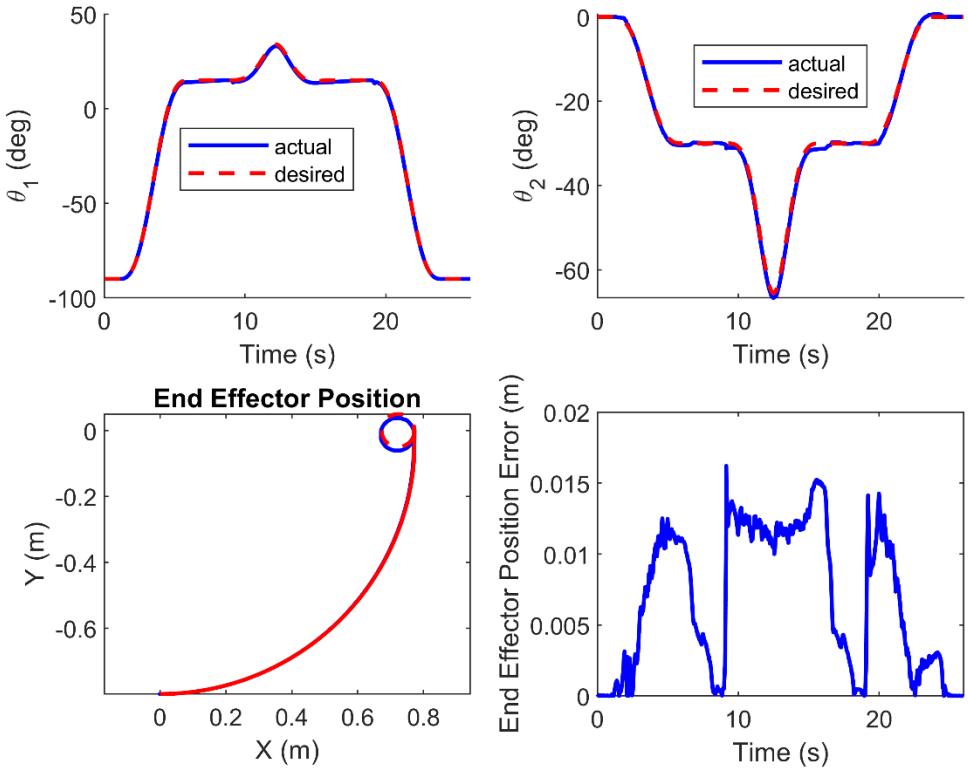

Figure 5.12 The joint and end-effector position tracking results with the end-effector following a circular path, placed higher in the workspace.

5.6 Conclusion

In this chapter, the design, implementation and control of a new elbow joint was presented. The new elbow joint was added to the existing single-DOF arm to make a two-DOF HPEA-driven manipulator. The kinematic and kinetic model of the two-DOF arm, as well as the geometry of the new elbow joint were studied. The design has been modelled in CAD, manufactured, and equipped with the sufficient instrumentation to be able to perform feedback position control. The elbow joint and its actuator were experimentally tested and proven to be able to achieve high performance position tracking (with RMSE as low as 0.05˚ and a SSE of 0.0045˚). The two-DOF manipulator's ability to perform independent

joint position tracking as well as end-effector Cartesian trajectory tracking was experimentally tested. The end-effector was able to follow a circular trajectory in pneumatic mode with position errors below 0.005 m.

References

[1] Shen X, Zhang J, Barth EJ, Goldfarb M. Nonlinear Model-Based Control of Pulse Width Modulated Pneumatic Servo Systems. J Dyn Syst Meas Control 2005;128:663–9. https://doi.org/10.1115/1.2232689.

[2] Nguyen, T.; Leavitt, J.; Jabbari, F.; Bobrow JE. Accurate Sliding-Mode Control of Pneumatic Systems Using Low Cost Solenoid Valves. IEEE Trans Mechatronics 2007;12:216–9. https://doi.org/10.1109/TMECH.2007.892821.

[3] Bobrow JE, McDonell BW. Modeling, identification, and control of a pneumatically actuated, force controllable robot. IEEE Trans Robot Autom 1998;14:732–42. https://doi.org/10.1109/70.720349.

[4] Rao Z, Bone GM. Nonlinear modeling and control of servo pneumatic actuators. IEEE Trans Control Syst Technol 2008. https://doi.org/10.1109/TCST.2007.912127.

[5] Van Varseveld RB, Bone GM. Accurate position control of a pneumatic actuator using on/off solenoid valves. IEEE/ASME Trans Mechatronics 1997;2:195–204. https://doi.org/10.1109/3516.622972.

[6] Falcão Carneiro J, Gomes De Almeida F. Modeling pneumatic servovalves using neural networks. Proc 2006 IEEE Conf Comput Aided Control Syst Des CACSD 2007:790–5. https://doi.org/10.1109/CACSD.2006.285478.

[7] Pandian S. Control performance of an air motor. Int Conf Robot Autom 1999;14:518–24. https://doi.org/10.1109/ROBOT.1999.770029.

[8] Hodgson S, Tavakoli M, Pham MT, Leleve A. Nonlinear discontinuous dynamics

averaging and pwm-based sliding control of solenoid-valve pneumatic actuators. IEEE/ASME Trans Mechatronics 2015;20:876–88. https://doi.org/10.1109/TMECH.2014.2326601.

[9] Rahman RA, He L, Sepehri N. Design and experimental study of a dynamical adaptive backstepping-sliding mode control scheme for position tracking and regulating of a low-cost pneumatic cylinder. Int J Robust Nonlinear Control 2016;26:853–75. https://doi.org/10.1002/rnc.3341.

[10] Bone GM, Chen X. Position control of hybrid pneumatic-electric actuators. Am Control Conf (ACC), 2012 2012:1793–9. https://doi.org/10.1016/j.mechatronics.2014.10.009.

[11] Bone GM, Xue M, Flett J. Position control of hybrid pneumatic-electric actuators using discrete-valued model-predictive control. Mechatronics 2015. https://doi.org/10.1016/j.mechatronics.2014.10.009.

[12] Ashby G, Bone GM. Improved hybrid pneumatic-electric actuator for robot arms, 2016. https://doi.org/10.1109/aim.2016.7576750.

[13] Tuvayanond W, Parnichkun M. Position control of a pneumatic surgical robot using PSO based 2-DOF H∞ loop shaping structured controller. Mechatronics 2017;43:40–55. https://doi.org/10.1016/j.mechatronics.2017.03.001.

[14] Chen Y, Godage IS, Tse ZTH, Webster RJ, Barth EJ. Characterization and control of a pneumatic motor for MR-conditional robotic applications. IEEE/ASME Trans Mechatronics 2017;22:2780–9. https://doi.org/10.1109/TMECH.2017.2767906.

[15] Shearer JL. Study of Pneumatic Processes in the Continuous Control of Motion With Compressed Air – I. Trans ASME n.d.:233–42.

[16] Richer E, Hurmuzlu Y. A high performance pneumatic force actuator system: Part I—nonlinear mathematical model. J Dyn Syst Meas Control Trans ASME 2000;122:416–25. https://doi.org/10.1115/1.1286336.

[17] Shu Ning, Bone GM. Development of a nonlinear dynamic model for a servo pneumatic positioning system. IEEE Int Conf Mechatronics Autom 2005 2005:43–8. https://doi.org/10.1109/ICMA.2005.1626520.

[18] Taheri B, Case D, Richer E. Force and stiffness backstepping-sliding mode controller for pneumatic cylinders. IEEE/ASME Trans Mechatronics 2014;19:1799–809. https://doi.org/10.1109/TMECH.2013.2294970.

[19] L. J. Petrosky. Hybrid Electro-Pneumatic Robot Joint Actuator. 478 225 828, n.d.

[20] Takemura F, Pandian SR, Nagase Y, Mizutani H, Hayakawa Y, Kawamura S. Control of a hybrid pneumatic/electric motor. IEEE Int. Conf. Intell. Robot. Syst., 2000. https://doi.org/10.1109/iros.2000.894606.

[21] Dongjun Shin, Sardellitti I, Khatib O. A hybrid actuation approach for human-friendly robot design 2008:1747–52. https://doi.org/10.1109/ROBOT.2008.4543453.

[22] Nakata Y, Noda T, Morimoto J, Ishiguro H. Development of a pneumatic-electromagnetic hybrid linear actuator with an integrated structure. 2015 IEEE/RSJ Int. Conf. Intell. Robot. Syst., IEEE; 2015, p. 6238–43. https://doi.org/10.1109/IROS.2015.7354267.

[23] Heinzmann J, Zelinsky A. Quantitative safety guarantees for physical human-robot interaction. Int J Rob Res 2003;22:479–504.

[24] Hirzinger G, Albu-Schäffer A, Hähnle M, Schaefer I, Sporer N. On a new generation of torque controlled light-weight robots. Proc - IEEE Int Conf Robot Autom 2001;4:3356–63. https://doi.org/10.1109/robot.2001.933136.

[25] Bicchi A, Tonietti G. Fast and "Soft-Arm" Tactics. IEEE Robot Autom Mag 2004;11:22–33. https://doi.org/10.1109/MRA.2004.1310939.

[26] Hyun D, Yang HS, Park J, Shim Y. Variable stiffness mechanism for human-friendly robots. Mech Mach Theory 2010.

https://doi.org/10.1016/j.mechmachtheory.2010.01.001.

[27] Lauzier N, Gosselin C. Performance Indices for Collaborative Serial Robots With Optimally Adjusted Series Clutch Actuators. J Mech Robot 2012. https://doi.org/10.1115/1.4005723.

[28] Moghani M, Kermani MR. Design and development of a hybrid magneto-rheological clutch for safe robotic applications. Robot. Autom. (ICRA), 2016 IEEE Int. Conf., IEEE; 2016, p. 3083–8.

[29] Suita K, Yamada Y, Tsuchida N, Imai K, Ikeda H, Sugimoto N. A failure-to-safety" Kyozon" system with simple contact detection and stop capabilities for safe human-autonomous robot coexistence. Robot. Autom. 1995. Proceedings., 1995 IEEE Int. Conf., vol. 3, IEEE; 1995, p. 3089–96.

[30] De Luca A, Albu-Schaffer A, Haddadin S, Hirzinger G. Collision detection and safe reaction with the DLR-III lightweight manipulator arm. Intell. Robot. Syst. 2006 IEEE/RSJ Int. Conf., IEEE; 2006, p. 1623–30.

[31] Jeong S, Takahashi T. Impact force reduction of manipulators using a dynamic acceleration polytope and flexible collision detection sensor. Adv Robot 2009;23:367–83.

[32] Haddadin S, Laue T, Frese U, Wolf S, Albu-Schäffer A, Hirzinger G. Kick it like a Safe Robot: Requirements for 2050. Rob Auton Syst 2009;57:761–75.

[33] Zeng L, Bone GM. Design of elastomeric foam-covered robotic manipulators to enhance human safety. Mech Mach Theory 2013. https://doi.org/10.1016/j.mechmachtheory.2012.09.010.

[34] Van Damme M, Vanderborght B, Verrelst B, Van Ham R, Daerden F, Lefeber D. Proxy-based sliding mode control of a planar pneumatic manipulator. Int J Rob Res 2009;28:266–84. https://doi.org/10.1177/0278364908095842.

[35] Johansen TA, Fossen TI. Control allocation - A survey. Automatica 2013;49:1087–

103. https://doi.org/10.1016/j.automatica.2013.01.035.

[36] Härkegård O. Dynamic Control Allocation Using Constrained Quadratic Programming. J Guid Control Dyn 2004;27:1028–34. https://doi.org/10.2514/1.11607.

[37] Galeani S, Pettinari S. On dynamic input allocation for fat plants subject to multi-sinusoidal exogenous inputs. Proc IEEE Conf Decis Control 2014;2015-Febru:2396–403. https://doi.org/10.1109/CDC.2014.7039754.

[38] Löfberg J. YALMIP: A toolbox for modeling and optimization in MATLAB. Proc IEEE Int Symp Comput Control Syst Des 2004:284–9. https://doi.org/10.1109/cacsd.2004.1393890.

[39] Mattingley J, Boyd S. CVXGEN: A code generator for embedded convex optimization. Optim Eng 2012;13:1–27. https://doi.org/10.1007/s11081-011-9176-9.

[40] Hanger M, Johansen TA, Mykland GK, Skullestad A. Dynamic model predictive control allocation using CVXGEN. IEEE Int Conf Control Autom ICCA 2011:417–22. https://doi.org/10.1109/ICCA.2011.6137940.

[41] Teramae T, Noda T, Hyon SH, Morimoto J. Modeling and control of a Pneumatic-Electric hybrid system. IEEE Int. Conf. Intell. Robot. Syst., 2013. https://doi.org/10.1109/IROS.2013.6697061.

[42] Ishihara K, Morimoto J. An optimal control strategy for hybrid actuator systems: Application to an artificial muscle with electric motor assist. Neural Networks 2018. https://doi.org/10.1016/j.neunet.2017.12.010.

[43] Rouzbeh B, Bone GM, Ashby G. High-Accuracy Position Control of a Rotary Pneumatic Actuator. IEEE/ASME Trans Mechatronics 2018;23:2774–81. https://doi.org/10.1109/TMECH.2018.2870177.

[44] Rouzbeh B, Bone GM, Ashby G, Li E. Design, Implementation and Control of an

Improved Hybrid Pneumatic-Electric Actuator for Robot Arms. IEEE Access 2019;7:14699–713. https://doi.org/10.1109/ACCESS.2019.2891532.

[45] Rouzbeh B, Bone GM. Optimal force allocation and position control of hybrid pneumatic-electric linear actuators. Actuators 2020. https://doi.org/10.3390/act9030086.

[46] Kim NH, Kim JM, Khatib O, Shin D. Design optimization of hybrid actuation combining macro-mini actuators. Int J Precis Eng Manuf 2017. https://doi.org/10.1007/s12541-017-0062-z.

[47] Findlay D, Jafarinasab M, Sirouspour S. Optimization-based design of a novel hybrid aerial/ground mobile manipulator. IEEE Int Conf Intell Robot Syst 2015;2015-Decem:2467–72. https://doi.org/10.1109/IROS.2015.7353712.

[48] Sharbafi MA, Shin H, Zhao G, Hosoda K, Seyfarth A. Electric-pneumatic actuator: A new muscle for locomotion. Actuators 2017. https://doi.org/10.3390/act6040030.

[49] Mori S, Tanaka K, Nishikawa S, Niiyama R, Kuniyoshi Y. High-Speed Humanoid Robot Arm for Badminton Using Pneumatic-Electric Hybrid Actuators. IEEE Robot Autom Lett 2019. https://doi.org/10.1109/LRA.2019.2928778.

[50] Craig JJ. Introduction to Modern Robotics: Mechanics, Planning, and Control. 2004.

[51] International Organization for Standardization. ISO/TS 15066:2016 - Robots and robotic devices - Collaborative robots. ISO/TC 299 Robot 2016.

Chapter 6. Conclusions and Recommendations

6.1 Conclusions

6.1.1 Control of a Rotary Pneumatic Actuator with Novel Pressure Controller

- The modelling, controller design and experimental verification of a high accuracy position controlled rotary pneumatic actuator were presented.
- The angular position is measured by an encoder directly coupled to the output shaft. Low-cost valves and pressure sensors were employed.
- The novel inverse valve model enabled the development of a faster and more precise model-based inner-loop pressure control law.
- The outer-loop position control law achieved small tracking errors using model-based terms plus position and velocity feedback.
- Mainly due to the adaptive friction compensator, the SSE was less than or equal to the encoder's resolution.
- Robustness to unknown payloads was achieved using an improved offline payload estimator.
- The experimental results are superior to those reported in the prior literature.

6.1.2 Study and Control of a Hybrid Pneumatic Electric Rotary Actuator

- A HPEA design with significantly higher torque output than previous designs, while maintaining the low mechanical impedance and inherent safety of the HPEA approach was used as a prototype. The HPEA is controlled by two inner-loop pressure controllers and an outer-loop position controller.
- The accuracy of the empirical inverse valve model enabled the pressure controllers to achieve high performance.
- Based on numerous experiments, the combination of adaptive friction compensation, model-based feedforward compensation, feedback compensation

and offline payload estimation allowed the HPEA to outperform the state of the art in terms of position RMSE and SSE.

- Dynamic models were developed for a constrained impact between a human head and robot arm powered by either the HPEA, a pneumatic actuator, or a conventional electric actuator. The simulation results showed that the HPEA produced the smallest impact force.
- The proposed HPEA can provide future collaborative robot arms with precise positioning, better inherent safety than conventional actuators, and lower production cost.

6.1.3 MPC-Based Input Allocation Techniques for HPEA

- Three novel control algorithms for the position control of an HPEA-driven system were investigated.
- The first (MPC1) uses MPC with a linearized full plant model. The second (MPC2) uses an outer-loop MPC with an inner-loop PI pressure controller with a simplified linear model. The third (MPC3) uses the same structure as MPC2 with a modified model to find a balance in the trade-off between the position controller performance and computation time. A fourth controller, employed as a benchmark, uses an outer-loop PD plus feedforward controller with an inner-loop PI pressure controller.
- MPC2 showed the best performance in reducing the input forces (and thus, the energy consumption and operating cost).
- The modified model used in MPC3 led to the best position tracking performance.
- Although MPC2 and MPC3 are computationally intensive, they can still be run in real-time using commonly available off-the-shelf hardware.

6.1.4 Implementation of a Two-Degree-of-Freedom Hybrid Pneumatic-Electric Driven Arm

The implementation and control of an additional elbow joint was studied, which was added to the existing single-DOF arm to make a two-DOF HPEA-driven manipulator.

The kinematic and kinetic models of the two-DOF arm, as well as the geometry of the new elbow joint were studied.

The design was modelled in CAD, manufactured, and equipped with the sufficient instrumentation to be able to perform feedback position control.

The elbow joint and its actuator were experimentally tested and proved to be able to achieve high performance position tracking (with RMSE as low as 0.05˚ and a SSE of 0.0045˚).

The two-DOF manipulator was experimentally tested to perform independent joint position tracking as well as end-effector tracking. The end-effector was able to follow a circular trajectory in pneumatic mode with position errors below 0.005 m.

6.2 Recommendations for Further Research

Despite the advances presented in this thesis, several aspects of the use of HPEAs in collaborative robots still require future study. Potential areas for further research include:

- The optimization-based task allocation techniques can be implemented and experimentally tested on rotary joints. This can be done either by local linearization of the plant model and using linear optimization tools or by using nonlinear optimization techniques, with the former being more computationally efficient. This approach can be expanded to both DOF of the HPEA-driven arm to achieve effective collaboration between the pneumatic and electric actuators, provided that the computation power can perform the optimization in real-time.
- The kinetic model (5.8)-(5.11) can be made more accurate by adopting a more general structure and identifying the parameters empirically.

- To avoid the subjectivity of the manual tuning approach, the application of global optimization strategies (such as particle swarm optimization) to obtain the controller parameters can be investigated.
- The novel model-based pressure controller used with the pneumatic subsystem can be modified to use data-driven control techniques with help of the empirical data from the experiments. This opens new opportunities to use the fast-growing machine learning and data analysis/refining tools in this area.
- An impact setup can be developed to experimentally study the impact between the HPEA-driven arm and biofidelic crash test dummy. This can be performed in different scenarios and compared to the results from a conventional electric-actuated arm to evaluate the inherent safety of the am in different situations.
- Elastomeric foam can be adopted to cover the most probable impact points of the HPEA-driven arm, and further improve its impact safety.
- The inherently safe HPEA-driven arm can be combined with active safety techniques to develop a comprehensive package for safe collaborative manipulators. These active techniques include vision-based collision avoidance, sensor-based collision mitigation and trajectory optimization to minimize the impact risk.